Multimodal Control of Adhesion in Polydopamine Nanomembranes through Texture, Microstructure, and Chemistry Control

Submitted in partial fulfillment of the requirements for

the degree of

Doctor of Philosophy

in

Materials Science and Engineering

Ik Soo Kwon

B.A., Physics, Economics, University of Pennsylvania

Carnegie Mellon University
Pittsburgh, PA

August 2018

Acknowledgement

I would like to first express my gratitude to my advisor, Professor Christopher J. Bettinger for his patience and guidance for the past four years. His guidance helped me build a structured mindset and stay focused during this journey in which one could easily get lost. The lessons I've learned from him are indispensable, and I am sure they will help me in life wherever the path leads me. I also thank my committee members, Professor Carmel Majidi, Professor Michael Bockstaller, and Professor Metin Sitti for their valuable inputs for my thesis. I acknowledge financial support from the following organizations: National Institutes of Health (R21NS095250); the Defense Advanced Research Projects Agency (D14AP00040); the National Science Foundation (DMR1542196); the Carnegie Mellon University School of Engineering; American Chemical Society (PRF51980DN17); the Pennsylvania Department of Community and Economic Development; Innovation Works (Pittsburgh, PA); the Department of Energy (DE-OE000226); the CMU Center for Technology Transfer and Enterprise Creation; the Shurl and Kay Curci Foundation; National Science Foundation (DMR1542196).

I would like to thank the former and current Bettinger group members for both their support and friendship. I would like to thank Young Jo Kim for the friendship and mentorship. Special thanks to my fellow coauthors, Brian Po-Ju Chiang and Guannan Tang for their indispensable efforts and friendship. Best of luck in your PhDs. I would like to thank Mats Forssell for immense help with EIS and fruitful discussions. Thanks to Luke Klosterman, Wei-Chen Huang, Haosheng Wu, Chenchen Mou, Aditya Balasubramanian, Faisal Ali, Maddie Cramer, Xiaomin Tang, Ashley Guertin, Riddhi Kachole and Aimon Iftikhar for being wonderful lab mates.

I also like to thank my MSE department friends, particularly, Minyoung Jeong, Jaejun Lee, Dasheng Li, Geonu Kim, and Tim Hsu. I thank Suzanne Choi for her continued support and encouragement, which enabled me to overcome many difficulties that would otherwise have been impossible to be overcome. Finally, I thank my parents (Jinil Kwon and Jan-Di Kim) and brother (Minho Kwon) for their love and faith in me. This thesis is dedicated to them. Their support kept me motivated during these challenging years, and without them, it would not have been possible.

Abstract

Finding that mussels rely on catechol and amine functional group enriched proteins to achieve robust underwater adhesion prompted scientists to create synthetic polymeric systems mimicking mussel chemistry. Polydopamine (PDA), mussel chemistry inspired polymeric coating, came to a spotlight in 2007. The primary advantage of PDA is that it can be easily deposited into a robust thin film onto various kinds of surfaces, a trait stemming from its rich content in catechol and amine motifs. The versatile functional nature of PDA enables envisioning of potential applications beyond the conformal coating; these characteristics include mixed electronic-ionic conductivity, chelation of cations, catechol-based redox activity, mechanical robustness as a nanomembrane, underwater adhesiveness, biocompatibility, and the presence of many functional groups for post-deposit modification.

The coexistence of a variety of characteristics in a single material indicates the possibility of tuning of material properties in programmable and multimodal manners. This thesis explores the fundamentals of macroscopic adhesion in PDA, with a particular focus on achieving the multimodal control of PDA adhesion. Using a custom-built Johnson-Kendall-Roberts apparatus, the adhesive property of PDA nanomembranes was examined in relation to their texture. It was revealed that PDA adhesion is a strong function of its morphology both in air and water, and could be tuned through morphological control. Persson's roughness theory was extended to model the underwater adhesion of PDA and showed a good agreement with the experiments.

PDA nanomembranes were interfaced with Polydimethylsiloxane (PDMS) substrates to create substrates with surface wrinkles. Dynamic control of surface wrinkles with mechanical

actuation translated into adhesion variance. A semi-analytical theoretical framework was developed to correlate adhesion of the composite structure to its surface wrinkle geometry.

Redox control of PDA adhesion was investigated. Presence of the catechol population with reversible chemistry was investigated through the aid of impedance spectroscopy circuit modeling. Chemical modulation of PDA adhesion through pH control was conducted, and the successful reversible variation of PDA adhesion with pH control was confirmed. Effect of pH and saline condition to PDA adhesion was analyzed in relation to catechol chemistry.

This thesis is an attempt to develop a framework to understand bulk adhesion of PDA nanomembranes to help the future translation of PDA into adhesive devices.

Table of Contents

List of Figures

List of Tables

Chapter 1
Introduction

The high content of catechol and amine molecules in mussel-foot proteins have inspired the rapid development of catechol and/or amine rich underwater adhesion systems from adhesive hydrogels to catecholamine coatings.[1-8] The most prominent example amongst mussel inspired polymeric systems is polydopamine (PDA). Synthesized by the O_2 induced oxidation of dopamine molecules in alkaline solutions, the deposition process leaves a conformal nanofilm on various kinds of surfaces (**Figure 1.1**).[2,9-12]

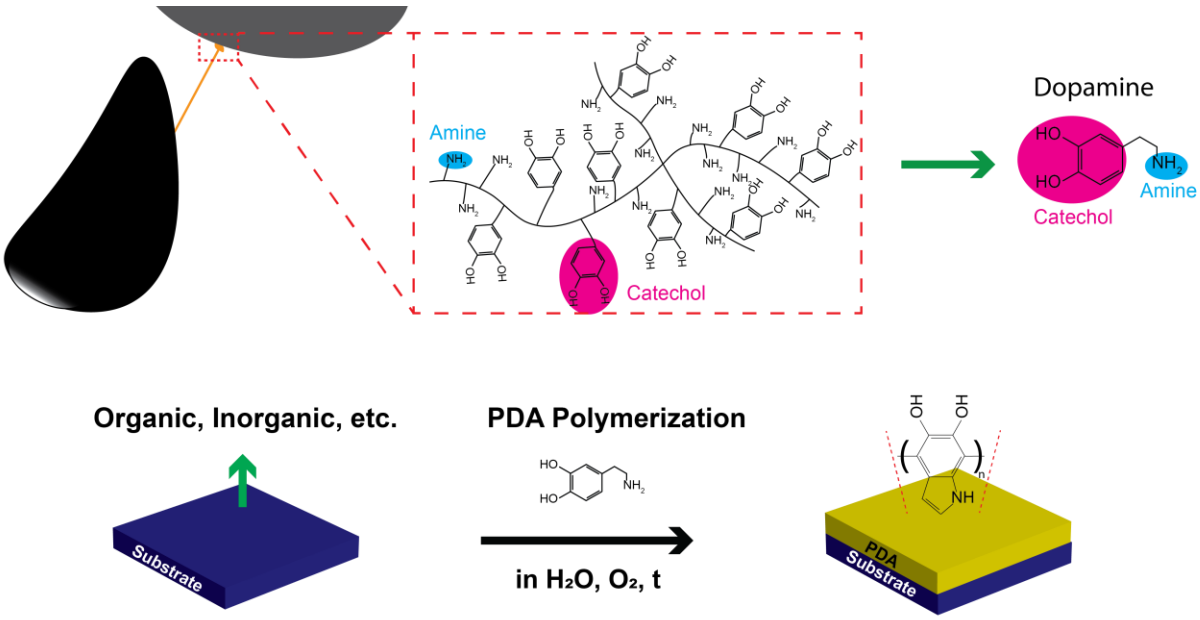

Figure 1.1 Top) Schematic illustrating the mussel-inspired chemistry of dopamine molecules. Bottom) Universal coating ability of polydopamine.

This introductory chapter will cover the general properties of PDA from its adhesive mechanism to synthesis and more, and will cover the existing applications of PDA. In the end, the motivation and objectives of this thesis will be presented.

1.1 General Properties of Polydopamine

1.1.1 Mussel-Inspired Adhesion

Mussels attach onto various surfaces under turbulent aqueous saline conditions robustly. There are multiple molecular and process engineering schemes that mussels rely on to form a reliable holdfast onto natural surfaces.[13] From the interfacial chemistry perspective, the most remarkable feature of the mussel adhesion strategy is the moisture resistance of its interfacial chemistry as the many molecular interactions weaken under the presence of water, particularly saline water.[14] Studies revealed that the adhesive proteins that mussel byssal threads secrete at the interface are rich in amine and catechol content (**Figure 1.2**).[13,15-17] Inspired by the high catechol and amine content in mussel foot proteins, Messersmith and co-workers devised a simple synthesis scheme that produces conformal adherent coatings on virtually every class of materials, and the material was termed polydopamine (PDA).[18] Produced by the O_2 induced oxidation of dopamine molecule that contains amine and catechol groups, PDA achieves universal coating ability through essentially the same molecular mechanism that mussel proteins utilize to achieve universal underwater adhesion.[18-20]

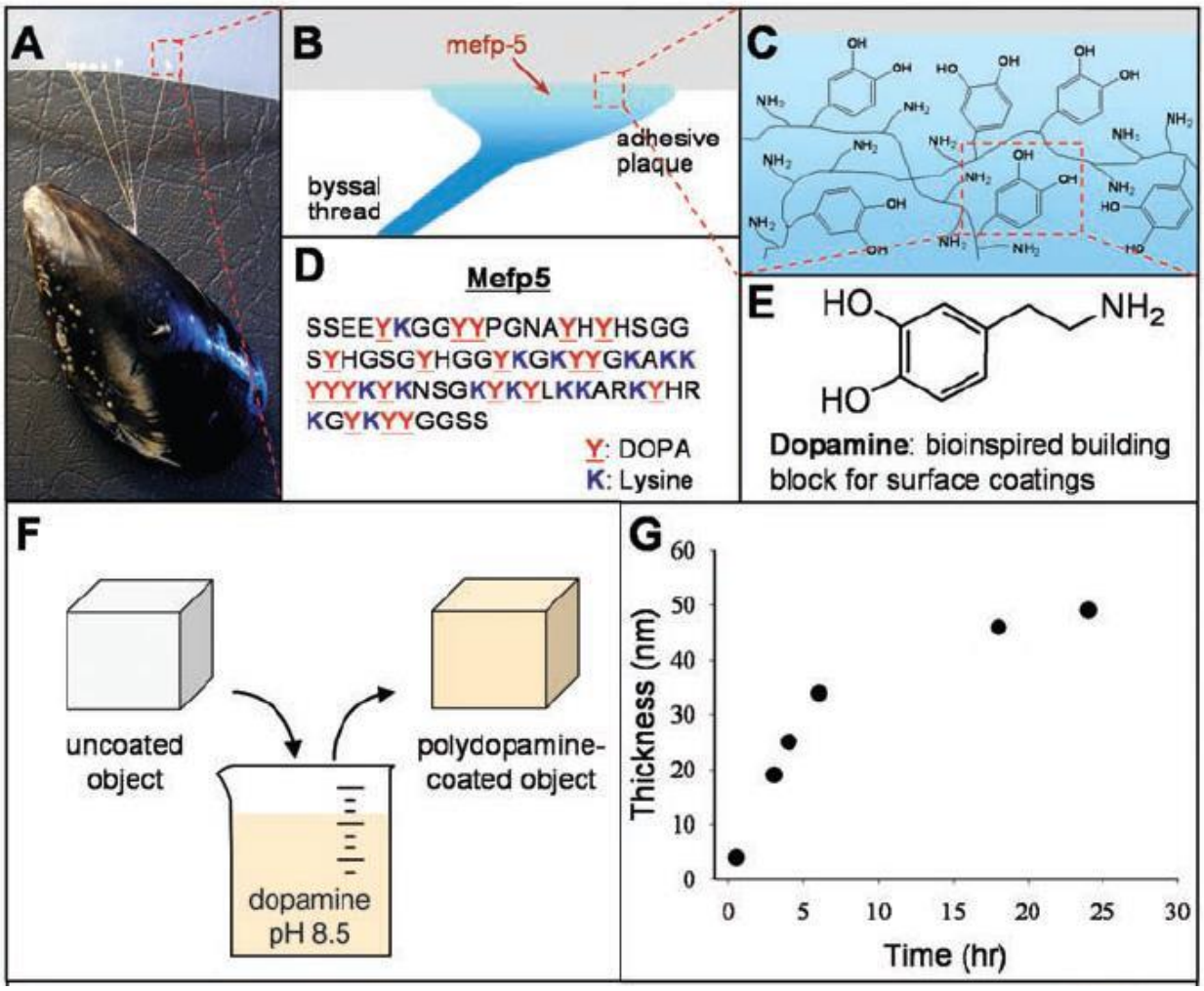

Figure 1.2: Mussel chemistry in mussels and PDA. a) Mussel attached to PTFE with byssal threads. b) Illustration of the byssal thread. c) Schematic of the molecular structure of the mussel adhesive protein, indicating the abundance of catechol and amine groups. d) Amino acid sequence of the adhesive protein also signifying the abundance of catechols (DOPA) and amines (Lysine). e) Dopamine molecule with catechol and amine groups. f) Schematic of PDA synthesis g) Thickness of the film versus time in solution. Reproduced from [18]

There are multiple interaction modes through which amine and catechol groups utilize to achieve robust underwater adhesion.[8] The role of direct adhesion is usually assigned to catechols.[21] Catechol exhibits diverse chemistries which enable it to bind various kinds of surfaces both reversibly and irreversibly (**Figure 1.3**).[22,23] The dihydroxy functionality of catechol enables it to form strong hydrogen bonds that is often energetically more favorable than water molecule adsorption,[13,24] to achieve strong adhesion with various surfaces such as mucosal tissues[25,26]

and hydroxyapatite surfaces.[8,27,28] However, it should be noted that depending on the substrate chemistry, nature of the OH group's interaction changes.[23,29,30] For the case of the metal oxide surfaces, reversible bidentate ligand-to-metal charge transform complex could be formed.[31] This interaction is especially powerful, and the single molecule AFM study between catechol and TiO_2 surface revealed that the strength of the metal-ligand interaction for catechol could reach up to 40% of that of the covalent bond interactions.[32] The benzene ring in catechol also enables cation- π interaction with charged surfaces, which is one of the strongest reversible mechanism in water.[33,34] Additional adhesion interaction modes include π-π interaction through the benzene ring of catechols[35,36] and hydrophobic interaction of catechols.[37] The oxidized form of catechol, *o*-quinone is also capable of covalent crosslinking with nucleophiles (e.g. amines or thiols) as well.[38-41]

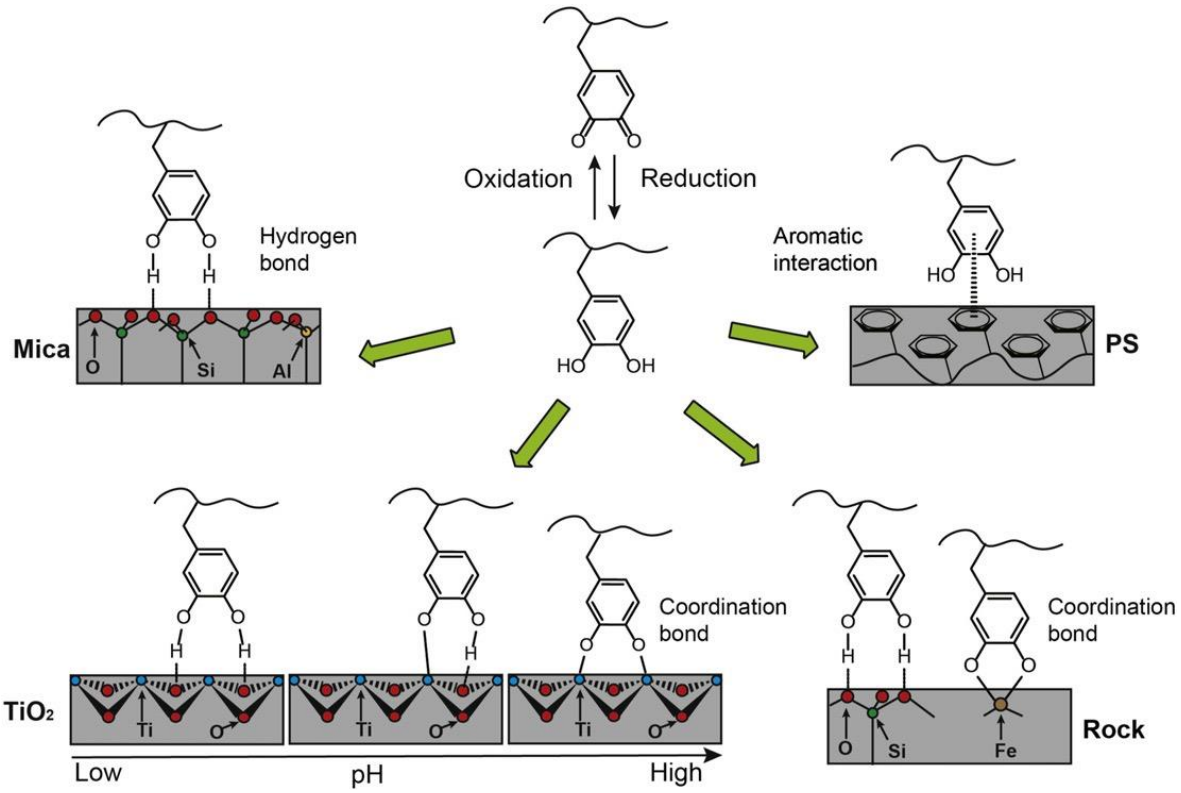

Figure 1.3: Various binding mechanisms of catechol (e.g. DOPA) to various surfaces depending on the nature of surface. Reproduced from [24]

Amines serve to remove surface cations present in saline conditions through the cooperative synergy with catechol.[16] In the marine environment, surfaces acquire a net negative charge regardless of their original polarity due to the adsorption of organics from sea water.[13] Due to the anionic nature of surfaces, cations are always present at the interface of natural surfaces, preventing catechols to achieve good adhesion. At pH of 8.5 (pH of natural sea water), amine groups bear positive charges, effectively removing the surface cations at natural surfaces, enabling catechols to interact with underlying surfaces (**Figure 1.4**).[13,42]

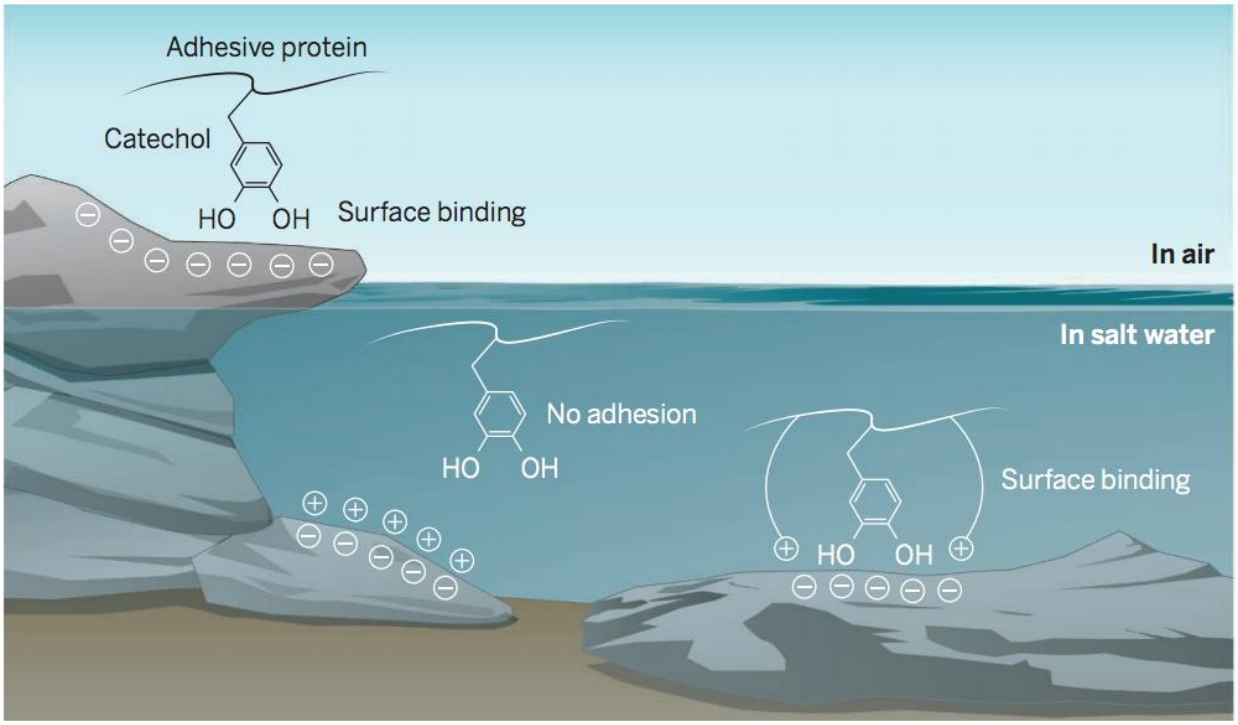

Figure 1.4: Illustration of cooperative synergy between catechol and amines (positive charge on adhesive protein). Amine serves to disrupt the cation layer on natural surfaces. Reproduced from [42]

The multifold adhesion scheme of catechol and amine functionalities enables versatile wet adhesion of mussel-foot proteins and other catecholamine systems, including PDA.

1.1.2 Synthesis and Structure of Polydopamine

The most widely used protocol for PDA synthesis is the simple solution oxidation method originally proposed by Messersmith and co-workers in 2007, even though some alternative synthesis schemes have been proposed to alter or improve the property of PDA.[9] When dopamine monomers are placed in an aerial alkaline condition (pH > 7.5), oxidative polymerization of the monomers occurs, resulting in conformal nanometer coating on surfaces in the solution.[2] The maximum thickness in a single reaction scheme is limited to 50 nm, the origin of which is still debatable but is most likely accounted for by the dopamine depletion from the coating solution.[9,43] The facile and universal deposition of PDA onto various surfaces is advantageous over other various organic coatings, which often involve lengthy preparation steps with specific apparatuses for preparation[44] or are fundamentally limited by target surface properties.[45] Contrary to the simple preparation protocol, the reaction pathway of PDA formation involves complex redox process and various intermediates, and up to date, there is no general consensus on the precise structure and reaction pathway of PDA.[43] It is generally accepted that formation of PDA involves both the covalent polymerization and non-covalent self-assembly of oligomers involving H-bonding and π - π interaction (**Figure 1.5**).[46] The primary building block of PDA is 5,6-dihydroxyindole (DHI), the oxidative product of dopamine, but the considerable amount of dopamine is remained unpolymerized within the PDA matrix, along with other intermediate species.[46] The resultant matrix is both physically and chemically stable and exhibits Young's modulus of about 2 Gpa.[11,43,47] An additional point to be noted is that PDA's heterogeneous nature is not only limited to its chemistry but also extends to its structural properties. Due to its highly adhesive nature, during synthesis, PDA film growth on the substrate is accompanied by the spherical self-aggregate growth that adheres to the PDA films grown on the substrates, result-

ing in a poor morphological homogeneity and mechanical homogeneity with many defect sites.[48,49 50]

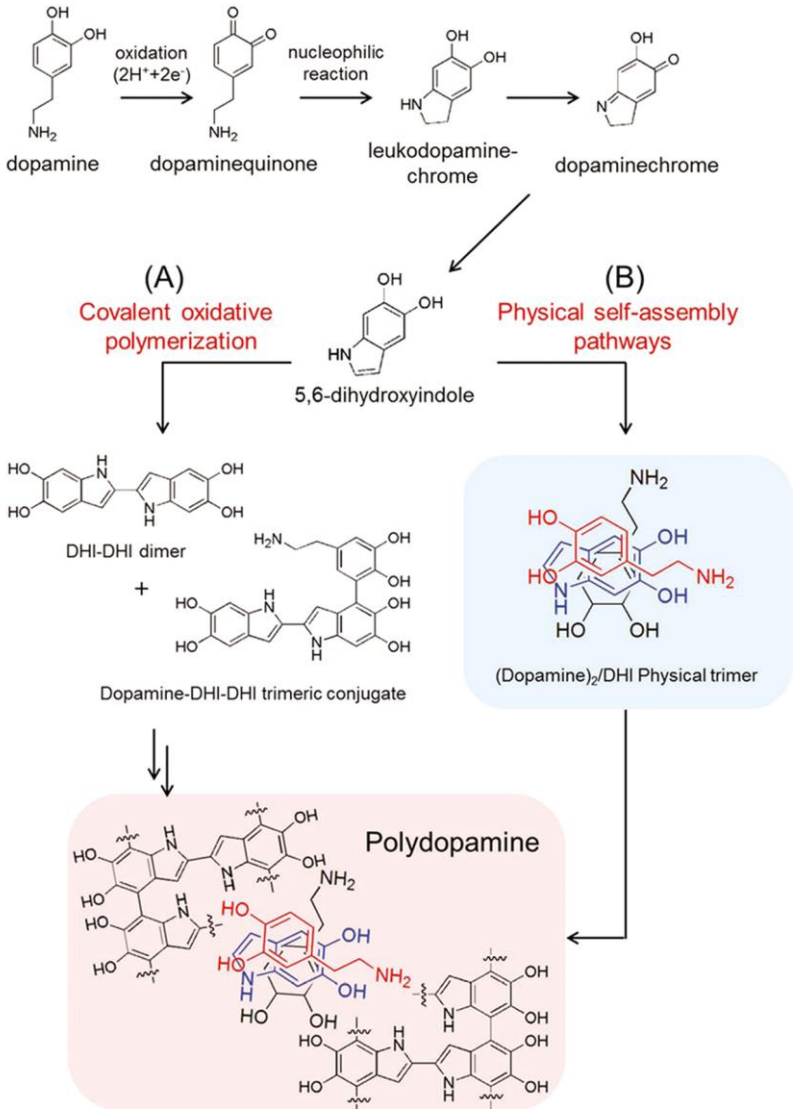

Figure 1.5: Two reaction pathways for the formation of PDA. a) Covalent polymerization. b) Non-covalent self-assembly. Reproduced from [46]

1.1.3 Other Properties

PDA bears marked structural similarity with synthetic and natural eumelanins and shares many of the characteristics of the two.[43,51] Both PDA and eumelanin possess ample catechol groups, and catechol redox chemistry is responsible for various properties in these two materials.

Catechol redox chemistry involves two-proton and two-electron reversible oxidation & reduction with semiquinone as an intermediate species and o-quinone as the oxidized form (**Figure 1.6**).[52] The hydration dependent comproportionation equilibrium exists between the catechol redox states (**Figure 1.7**),[53] and the resultant stable population of semiquinone intermediate species results in the hydration dependent mixed electronic-protonic conductivity.[54] Catechol groups also chelate with multivalent metal ions with pH-dependent complex forming behavior (**Figure 1.8**).[55,56] *O*-quinone exhibits strong reactivity with thiols and amines as mentioned, via Schiff base or Michael addition reactions, which is especially useful for conjugation of various biomolecules (**Figure 1.9**).[10] Other functional groups in PDA, carboxy, amino, imine, and phenol permit various reactions with a wide range of molecule as well.[10,43] Also thanks to its structural similarity to naturally occurring eumelanin, PDA exhibits excellent biocompatibility.[43]

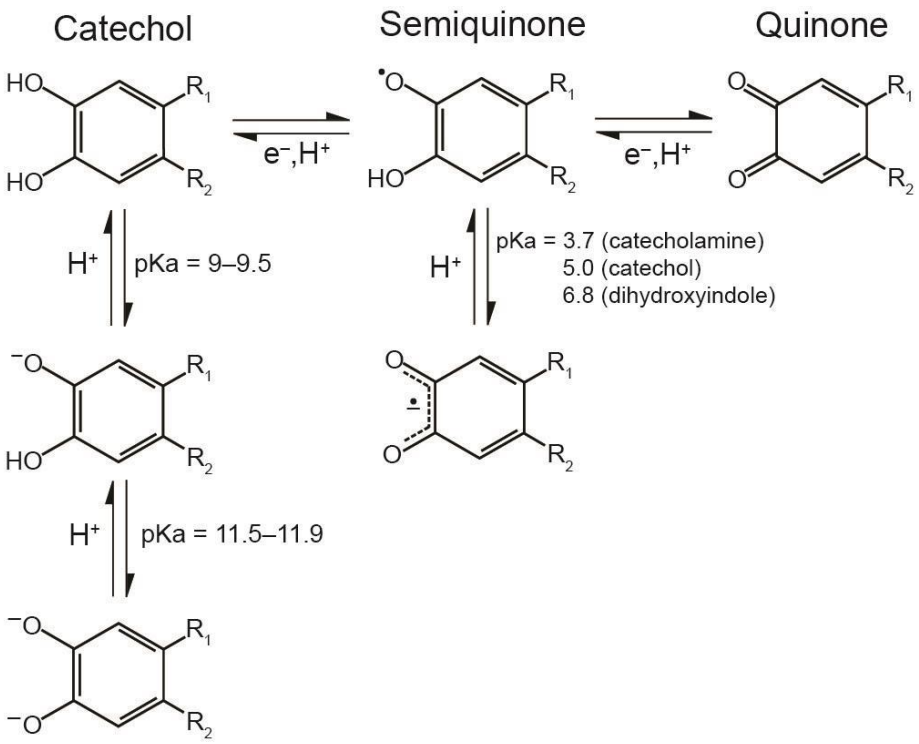

Figure 1.6: Various chemical equilibria of catechols. Reproduced from [57]

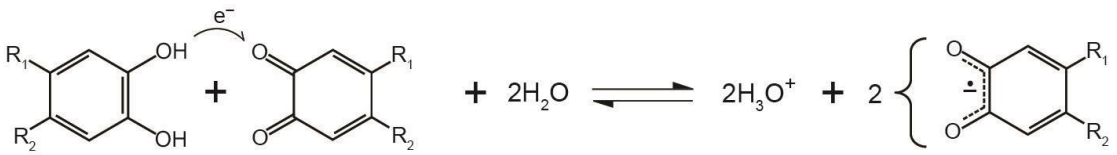

Figure 1.7: Comproportionation equilibrium of catechol. Reproduced from [57]

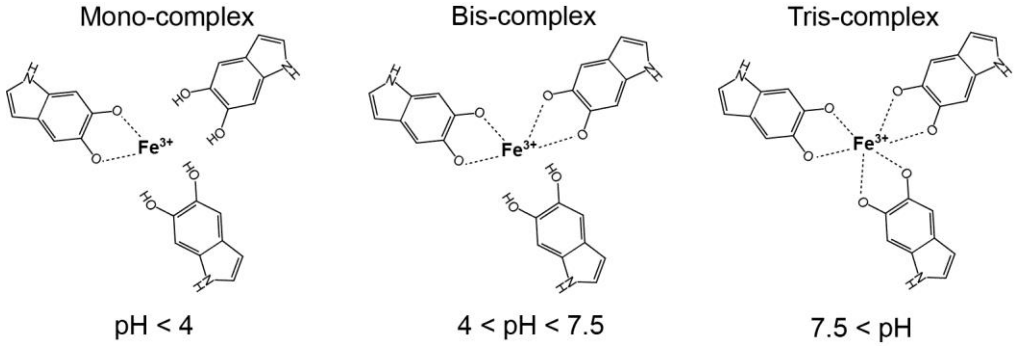

Figure 1.8: pH-dependent Fe^{3+} chelation to catechol groups. Reproduced from [55] and [58]

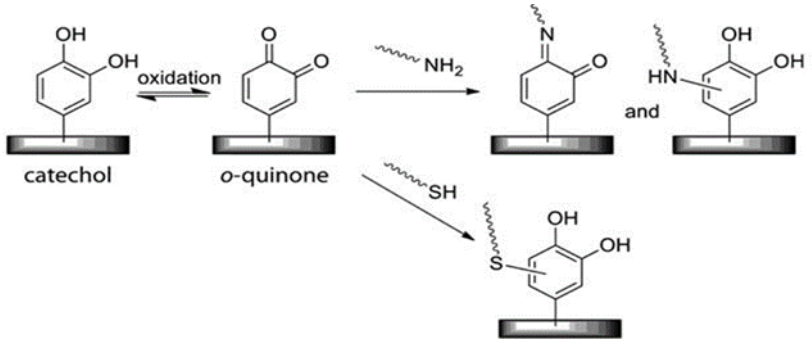

Figure 1.9: Chemical Reactivity of *o*-quinone with thiols and amines. Schiff base reaction and Michael addition with amines (top). Michael addition of thiols (bottom). Reproduced from [10]

1.2 Existing Applications

The versatile nature of PDA has led to investigations in the context of various applications. Certain applications require the hydrophobicity of surfaces to be diminished, and PDA has been extensively used in the area. For example, polyethylene separators in Li-ion batteries were coated with PDA for improved hydrophilicity (**Figure 1.10**).[59] Also the low surface energy substrates can be coated with PDA for block-copolymer lithography.[60] Cell behaviors can be regulated with PDA surfaces, achieving selective proliferation and adhesion of cells (**Figure**

1.11).[61] A wide range of functional groups present in PDA permits the binding of various molecules to PDA through secondary reactions (covalent crosslinking). Biomolecule bound PDA was covered on implant surfaces to regulate *in vivo* behavior.[62,63] Additionally, PDA has been extensively explored as a component in nanoparticle drug delivery (**Figure 1.12**). It was used either as a stand-alone vesicle in either spherical[64,65]or hollow-spherical form[66,67] or as an ad-layer on other nanoparticles for binding sites for therapeutic agents.[63,68,69] Also, the high-adhesive nature of PDA chemistry permitted exploration of PDA coating as an adhesion promoting layer for gastric retention of therapeutic nanoparticles for long-term drug delivery (**Figure 1.13**).[70] PDA-nanoparticle approach extends to catalyst binding and carbon adsorption as well.[71]

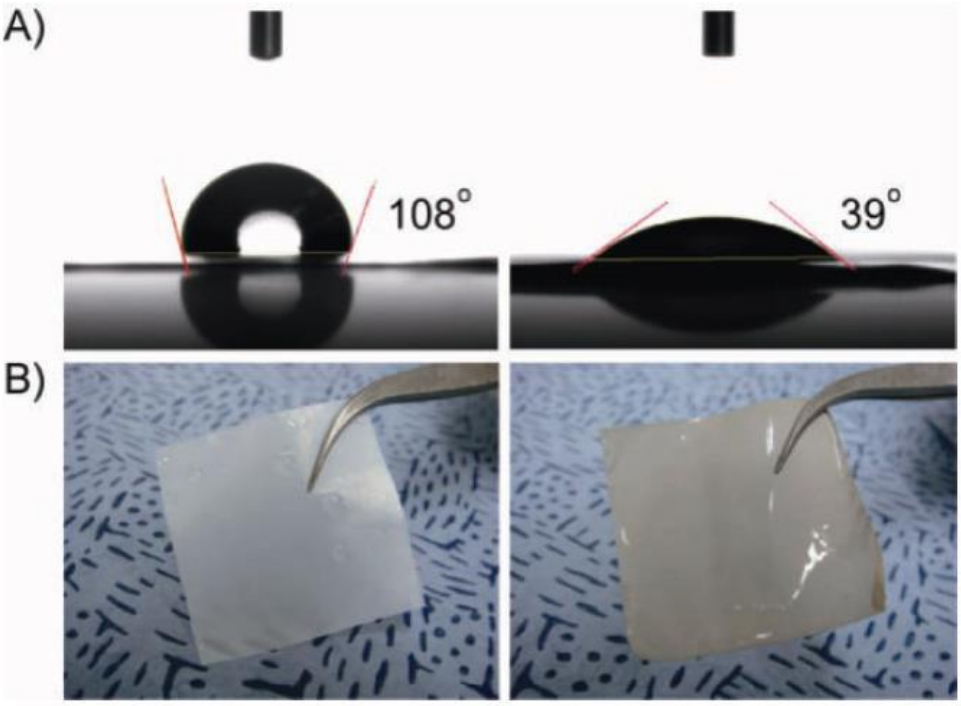

Figure 1.10: Contact angle of a Li-ion battery electrolyte on the polyethylene separator before (left) and after (right) PDA Coating. Reproduced from [59]

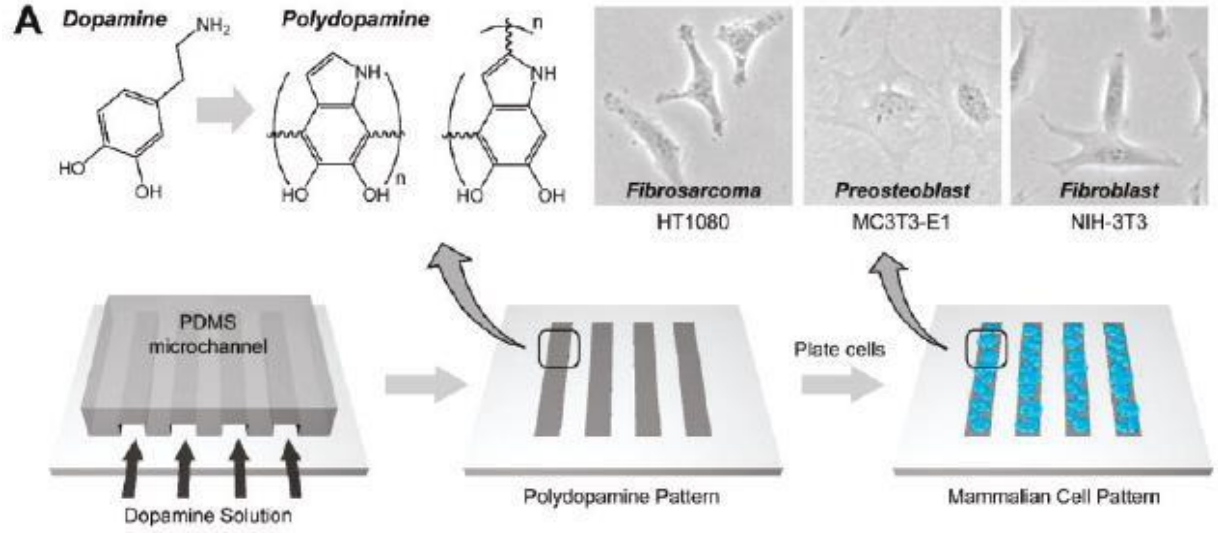

Figure 1.11: Illustration of cell patterning on the PDMS substrate using PDA. Reproduced from [61]

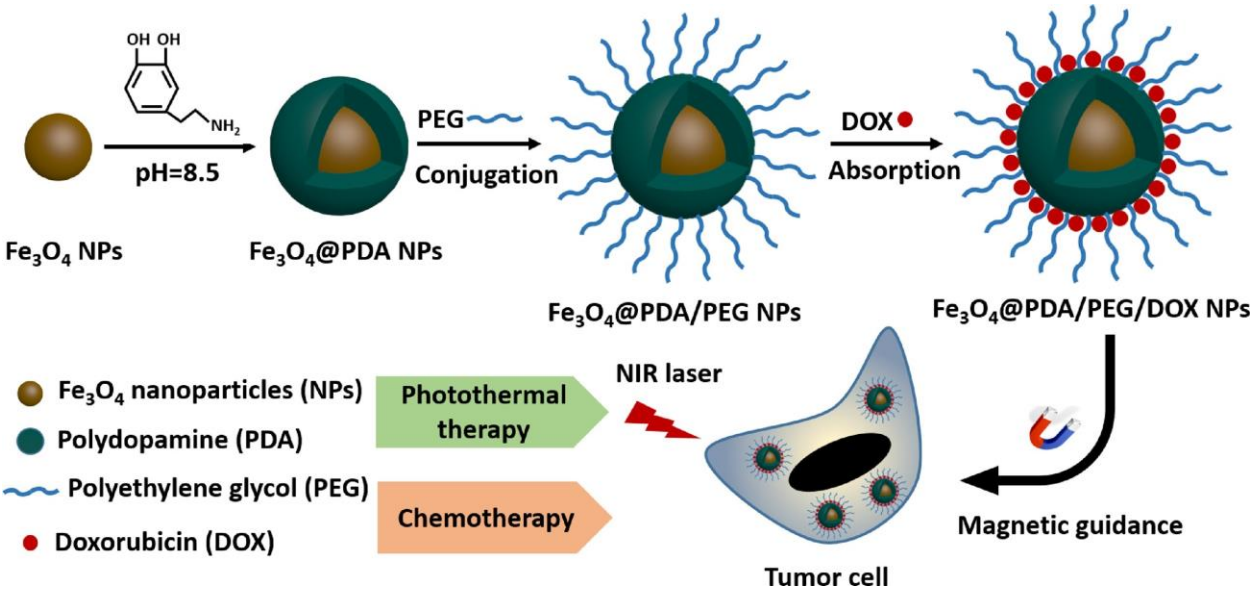

Figure 1.12: Schematic illustration of the synthesis route and application of PEGylated polydopamine coated nanoparticles for drug delivery. Reproduced from [68]

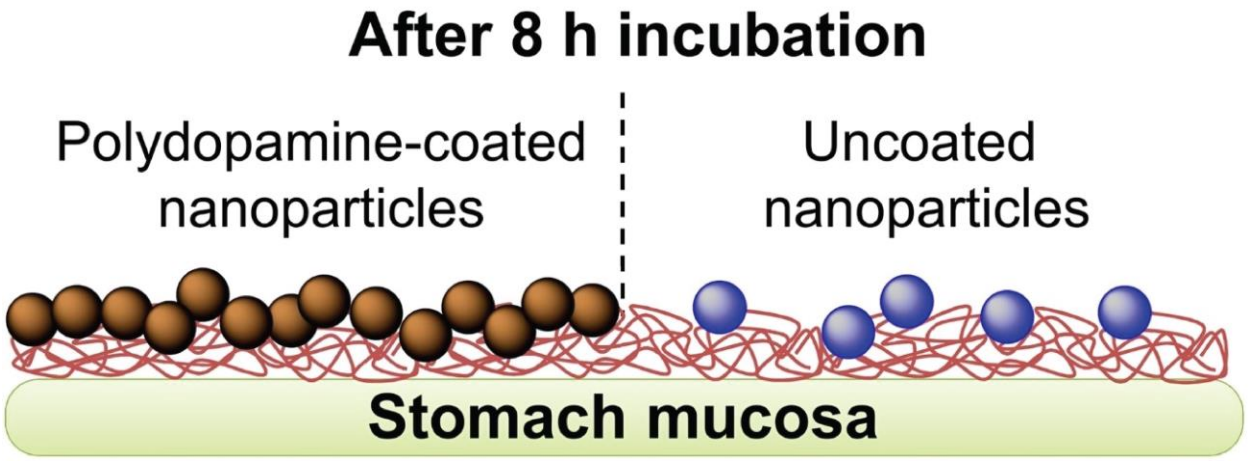

Figure 1.13: Mucoadhesive polydopamine-coated nanoparticles as a gastro-retentive drug delivery. Reproduced from [70]

Redox-active catechol chemistry also permits interesting applications in other areas as well. Motivated by the metal chelation behavior of PDA, glass micro-beads were coated with PDA for high surface area metal sorption surfactant.[72] In addition to the passive water purification, redox-active water purification was also demonstrated through reversible redox cycling of catechols in PDA; stainless steel meshes were coated with PDA, and through repetitive voltage cycling, Mg^{2+} ions were effectively separated from water (**Figure 1.14**).[73] Plethora of reactivity in catechol chemistry also permits relatively high-specificity of molecular interactions in PDA, which inspired the use of PDA in chemical sensing applications.[43] Applications in microfluidic devices are being actively investigated as well.[74]

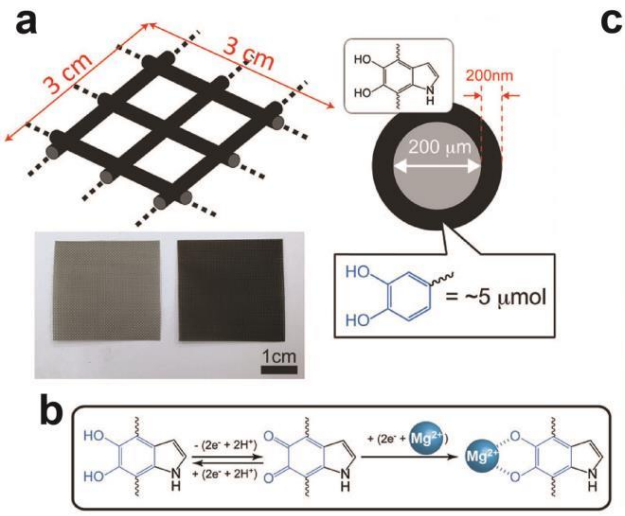

Table 4. Comparison of binding capacity of melanins to divalent ions

Material	Electrochemically mediated	Ion	Binding capacity (mmol g^{-1})	Ref.
Natural melanin[a]	No	Mg^{2+}	1.3	43
Natural melanin[a]	No	Ca^{2+}	1.4	43
Natural melanin[a]	No	Cu^{2+}	1.1	43
Natural melanin[a]	No	Zn^{2+}	1.5	43
Natural melanin[a]	Yes	Mg^{2+}	0.85	21
Synthetic melanin[b]	No	Mg^{2+}	1.91	This work
Synthetic melanin[b]	Yes	Mg^{2+}	4.61[c]	This work
Synthetic melanin[b]	Yes	Mg^{2+}	5.39[d]	This work

[a] Sourced from the ink sacs of *Sepia officinalis*.
[b] Synthesized through oxidative polymerization of dopamine in aqueous solutions.
[c] First cycle.
[d] 100th cycle.

Figure 1.14: Redox-active divalent ion removal from water using PDA. a) Stainless steel meshes were coated with PDA. b) Proposed mechanism of Mg^{2+} ion removal. c) Comparisons of binding capacity of divalent ions for various melanins. Reproduced from [73]

1.3 Summary and Motivations

Mussel-inspired chemistry of polydopamine is marked by the remarkable versatility and has provided the scientists and engineers the uniquely adaptable toolbox to tweak the surface properties of many materials under various applicational contexts. Belying its ability to form conformal coatings onto virtually any kind of surface is the lack of study into the use of PDA as an adhesive interface. From the interface chemistry viewpoint, very few materials match the capability of PDA, which exhibits strong underwater molecular adhesive power onto a wide variety of surfaces. However, preferential interfacial chemistry alone is not enough for bulk-adhesion between two materials. Surfaces in real-world settings are almost always characterized by the presence of a certain degree of roughness. Bulk adhesives (pressure sensitive adhesives) are typically characterized by a relatively low Young's modulus (< 1MPa),[75] at least at the interface, so that the material can conform onto the roughness of the surfaces without incurring too much mechanical stress, which could abolish adhesion.[76] Dahlquist criterion for tack provides a fairly material or surface independent reference point for the conformal contact to

occur in many of the practical settings, which is around 0.3 MPa (**Figure 1.15**).[77] PDA's Young's modulus is reported to be around 2 Gpa,[47] which indicates that the use of PDA as an adhesive in a conventional sense would be impractical unless the other interacting body is of soft nature such as biological tissues.

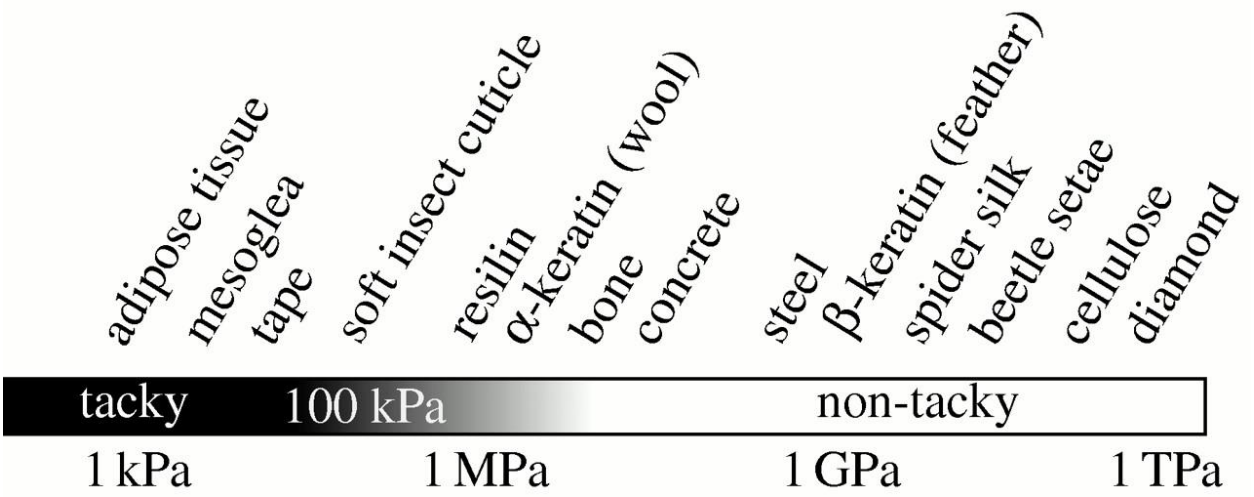

Figure 1.15: A continuum of Young's moduli of various materials with their tackiness implied by the Dahlquist criterion. Reproduced from [75]

However, nature has shown that making adhesives out of stiff materials is possible, as elaborately demonstrated with the example of gecko adhesion.[78] β – keratin which composes gecko-feet has high elastic modulus of about 1 ~ 3 Gpa,[75] yet gecko-feet exhibits remarkable bulk-adhesive capability. Studies revealed that the primary origin of this high-adhesion of gecko feet made of stiff material is due to the adaptation of the high aspect-ratio microfibrillar structures that scales down the effective modulus of the gecko-feet to 100kPa[79,80] and increases the linear dimension of the contact area through contact-splitting,[81] although other complex mechanical principles are employed to enable practical adhesion. Additional benefit of the micro-structured approach with the rigid material is the reversibility of high-adhesion as the material maintains its geometrical integrity even after multiple detachment and attachment cycles,[82] a feat that the conventional

bulk-adhesives are normally incapable of, due to susceptibility to deformation caused by their soft nature.

The example of gecko-feet implies that PDA has potential as an interface material for micro-structured adhesives; nanometer thickness of PDA implies that it could be interfaced with various substrate materials under various geometries such as mushroom-shaped adhesives.[83] Additional benefits could be realized with the use of PDA due to the unique material properties of PDA. For instance, the reversible high underwater adhesive could be realized, a concept that very few successful practical demonstrations have been made.[84] Also, the redox-state dependent controllability of catechol adhesion implies that the modulation of adhesion through chemical means might be possible as well. However, a caution should be noted in applying PDA as an interface material for micro-structured adhesives as PDA is characterized by a marked structural and chemical heterogeneity. To translate PDA successfully into micro-structured adhesive applications and achieve some PDA specific novel features, a thorough understanding of PDA material's characteristics in relation to its bulk adhesive behavior would be needed. Yet, the macroscopic adhesive behavior of PDA is an underexplored subject. The aim of this thesis is to examine the bulk-adhesive behavior of PDA to serve the dual purpose of filling in the missing gap in the literature and assessing the potential of some PDA based bulk adhesion modulation schemes, thus laying the groundwork to direct PDA research into some novel directions.

1.4 References

1 Lee, B. P., Dalsin, J. L. & Messersmith, P. B. Synthesis and gelation of DOPA-Modified poly(ethylene glycol) hydrogels. *Biomacromolecules* **3**, 1038-1047, doi:10.1021/bm025546n (2002).

2 Lee, B. P., Messersmith, P. B., Israelachvili, J. N. & Waite, J. H. Mussel-Inspired Adhesives and Coatings. *Annu Rev Mater Res* **41**, 99-132, doi:10.1146/annurev-matsci-062910-100429 (2011).

3 Meredith Heather, J., Jenkins Courtney, L. & Wilker Jonathan, J. Enhancing the Adhesion of a Biomimetic Polymer Yields Performance Rivaling Commercial Glues. *Advanced Functional Materials* **24**, 3259-3267, doi:10.1002/adfm.201303536 (2014).

4 Sever, M. J. & Wilker, J. J. Synthesis of peptides containing DOPA (3,4-dihydroxyphenylalanine). *Tetrahedron* **57**, 6139-6146, doi:https://doi.org/10.1016/S0040-4020(01)00601-9 (2001).

5 Shin, E. *et al.* Bioinspired Catecholic Primers for Rigid and Ductile Dental Resin Composites. *ACS Applied Materials & Interfaces* **10**, 1520-1527, doi:10.1021/acsami.7b14679 (2018).

6 Ahn, B. K. *et al.* High-performance mussel-inspired adhesives of reduced complexity. *Nature Communications* **6**, 8663, doi:10.1038/ncomms9663

https://www.nature.com/articles/ncomms9663#supplementary-information (2015).

7 Zhao, Q. *et al.* Underwater contact adhesion and microarchitecture in polyelectrolyte complexes actuated by solvent exchange. *Nature Materials* **15**, 407, doi:10.1038/nmat4539

https://www.nature.com/articles/nmat4539#supplementary-information (2016).

8 Kord Forooshani, P. & Lee Bruce, P. Recent approaches in designing bioadhesive materials inspired by mussel adhesive protein. *Journal of Polymer Science Part A: Polymer Chemistry* **55**, 9-33, doi:10.1002/pola.28368 (2016).

9 Ryu, J. H., Messersmith, P. B. & Lee, H. Polydopamine Surface Chemistry: A Decade of Discovery. *ACS Applied Materials & Interfaces* **10**, 7523-7540, doi:10.1021/acsami.7b19865 (2018).

10 Lynge, M. E., van der Westen, R., Postma, A. & Stadler, B. Polydopamine-a nature-inspired polymer coating for biomedical science. *Nanoscale* **3**, 4916-4928, doi:10.1039/c1nr10969c (2011).

11 Liu, X. S. *et al.* Mussel-Inspired Polydopamine: A Biocompatible and Ultrastable Coating for Nanoparticles in Vivo. *Acs Nano* **7**, 9384-9395, doi:10.1021/nn404117j (2013).

12 Dreyer, D. R., Miller, D. J., Freeman, B. D., Paul, D. R. & Bielawski, C. W. Elucidating the structure of poly (dopamine). *Langmuir* **28**, 6428-6435 (2012).

13 Waite, J. H. Natures Underwater Adhesive Specialist. *Chemtech* **17**, 692-697 (1987).

14 Lee, B. P., Messersmith, P. B., Israelachvili, J. N. & Waite, J. H. Mussel-Inspired Adhesives and Coatings. *Annual Review of Materials Research* **41**, 99-132, doi:10.1146/annurev-matsci-062910-100429 (2011).

15 Waite, J. H. Nature's underwater adhesive specialist. *International Journal of Adhesion and Adhesives* **7**, 9-14, doi:https://doi.org/10.1016/0143-7496(87)90048-0 (1987).

16 Maier, G. P., Rapp, M. V., Waite, J. H., Israelachvili, J. N. & Butler, A. Adaptive synergy between catechol and lysine promotes wet adhesion by surface salt displacement. *Science* **349**, 628 (2015).

17 Silverman, H. G. & Roberto, F. F. Understanding Marine Mussel Adhesion. *Marine Biotechnology* **9**, 661-681, doi:10.1007/s10126-007-9053-x (2007).

18 Lee, H., Dellatore, S. M., Miller, W. M. & Messersmith, P. B. Mussel-inspired surface chemistry for multifunctional coatings. *Science* **318**, 426-430, doi:10.1126/science.1147241 (2007).

19 Liu, M. *et al.* Recent developments in polydopamine: an emerging soft matter for surface modification and biomedical applications. *Nanoscale* **8**, 16819-16840, doi:10.1039/C5NR09078D (2016).

20 Ding, Y. H., Floren, M. & Tan, W. Mussel-inspired polydopamine for bio-surface functionalization. *Biosurface and Biotribology* **2**, 121-136, doi:https://doi.org/10.1016/j.bsbt.2016.11.001 (2016).

21 Waite, J. H. & Tanzer, M. L. Polyphenolic substance of Mytilus edulis: novel adhesive containing L-dopa and hydroxyproline. *Science* **212**, 1038-1040 (1981).

22 Hofman Anton, H., van Hees Ilse, A., Yang, J. & Kamperman, M. Bioinspired Underwater Adhesives by Using the Supramolecular Toolbox. *Adv Mater* **30**, 1704640, doi:10.1002/adma.201704640 (2018).

23 Ye, Q., Zhou, F. & Liu, W. Bioinspired catecholic chemistry for surface modification. *Chemical Society Reviews* **40**, 4244-4258, doi:10.1039/C1CS15026J (2011).

24 Li, L. & Zeng, H. Marine mussel adhesion and bio-inspired wet adhesives. *Biotribology* **5**, 44-51, doi:http://dx.doi.org/10.1016/j.biotri.2015.09.004 (2016).

25 Catron, N. D., Lee, H. & Messersmith, P. B. Enhancement of poly(ethylene glycol) mucoadsorption by biomimetic end group functionalization. *Biointerphases* **1**, 134-141, doi:10.1116/1.2422894 (2006).

26 Schnurrer, J. & Lehr, C.-M. Mucoadhesive properties of the mussel adhesive protein. *International Journal of Pharmaceutics* **141**, 251-256, doi:https://doi.org/10.1016/0378-5173(96)04625-X (1996).

27 Chirdon William, M., O'Brien William, J. & Robertson Richard, E. Adsorption of catechol and comparative solutes on hydroxyapatite. *Journal of Biomedical Materials Research Part B: Applied Biomaterials* **66B**, 532-538, doi:10.1002/jbm.b.10041 (2003).

28 Coombs, T. L. & Keller, P. J. Mytilus byssal threads as an environmental marker for metals. *Aquatic Toxicology* **1**, 291-300, doi:https://doi.org/10.1016/0166-445X(81)90023-0 (1981).

29 Malisova, B., Tosatti, S., Textor, M., Gademann, K. & Zürcher, S. Poly(ethylene glycol) Adlayers Immobilized to Metal Oxide Substrates Through Catechol Derivatives: Influence of Assembly Conditions on Formation and Stability. *Langmuir* **26**, 4018-4026, doi:10.1021/la903486z (2010).

30 Anderson, T. H. *et al.* The Contribution of DOPA to Substrate–Peptide Adhesion and Internal Cohesion of Mussel-Inspired Synthetic Peptide Films. *Advanced functional materials* **20**, 4196-4205, doi:10.1002/adfm.201000932 (2010).

31 Stewart, R. J., Ransom, T. C. & Hlady, V. Natural Underwater Adhesives. *J Polym Sci Pol Phys* **49**, 757-771, doi:10.1002/polb.22256 (2011).

32 Lee, H., Scherer, N. F. & Messersmith, P. B. Single-molecule mechanics of mussel adhesion. *P Natl Acad Sci USA* **103**, 12999-13003, doi:10.1073/pnas.0605552103 (2006).

33 Gallivan, J. P. & Dougherty, D. A. A Computational Study of Cation−π Interactions vs Salt Bridges in Aqueous Media: Implications for Protein Engineering. *Journal of the American Chemical Society* **122**, 870-874, doi:10.1021/ja991755c (2000).

34 Lu, Q. *et al.* Nanomechanics of Cation–π Interactions in Aqueous Solution. *Angewandte Chemie International Edition* **52**, 3944-3948, doi:10.1002/anie.201210365 (2013).

35 Waiter J, H. Reverse Engineering of Bioadhesion in Marine Mussels. *Annals of the New York Academy of Sciences* **875**, 301-309, doi:10.1111/j.1749-6632.1999.tb08513.x (2006).

36 Lim, C. *et al.* Nanomechanics of Poly(catecholamine) Coatings in Aqueous Solutions. *Angew Chem Int Edit* **55**, 3342-3346, doi:10.1002/anie.201510319 (2016).

37 Yu, J. *et al.* Adaptive hydrophobic and hydrophilic interactions of mussel foot proteins with organic thin films. *P Natl Acad Sci USA* **110**, 15680-15685, doi:10.1073/pnas.1315015110 (2013).

38 Yu, M., Hwang, J. & Deming, T. J. Role of L-3, 4-dihydroxyphenylalanine in mussel adhesive proteins. *Journal of the American Chemical Society* **121**, 5825-5826 (1999).

39 Liu, B., Burdine, L. & Kodadek, T. Chemistry of periodate-mediated cross-linking of 3, 4-dihydroxylphenylalanine-containing molecules to proteins. *Journal of the American Chemical Society* **128**, 15228-15235 (2006).

40 Matos-Pérez, C. R., White, J. D. & Wilker, J. J. Polymer composition and substrate influences on the adhesive bonding of a biomimetic, cross-linking polymer. *Journal of the American Chemical Society* **134**, 9498-9505 (2012).

41 Yang, J. *et al.* The effect of molecular composition and crosslinking on adhesion of a bio-inspired adhesive. *Polymer Chemistry* **6**, 3121-3130 (2015).

42 Wilker, J. J. Positive charges and underwater adhesion. *Science* **349**, 582-583, doi:10.1126/science.aac8174 (2015).

43 Liu, Y. L., Ai, K. L. & Lu, L. H. Polydopamine and Its Derivative Materials: Synthesis and Promising Applications in Energy, Environmental, and Biomedical Fields. *Chem Rev* **114**, 5057-5115, doi:10.1021/cr400407a (2014).

44 Shim, B. S. *et al.* Nanostructured thin films made by diewetting method of layer-by-layer assembly. *Nano Lett* **7**, 3266-3273, doi:10.1021/nl071245d (2007).

45 Wei, Q. & Haag, R. Universal polymer coatings and their representative biomedical applications. *Mater Horiz* **2**, 567-577, doi:10.1039/c5mh00089k (2015).

46 Hong, S. *et al.* Non-Covalent Self-Assembly and Covalent Polymerization Co-Contribute to Polydopamine Formation. *Advanced Functional Materials* **22**, 4711-4717, doi:10.1002/adfm.201201156 (2012).

47 Klosterman, L., Ahmad, Z., Viswanathan, V. & Bettinger Christopher, J. Synthesis and Measurement of Cohesive Mechanics in Polydopamine Nanomembranes. *Advanced Materials Interfaces* **4**, 1700041, doi:10.1002/admi.201700041 (2017).

48 Klosterman, L., Riley, J. K. & Bettinger, C. J. Control of Heterogeneous Nucleation and Growth Kinetics of Dopamine-Melanin by Altering Substrate Chemistry. *Langmuir* **31**, 3451-3458, doi:10.1021/acs.langmuir.5b00105 (2015).

49 Cho, J. H. *et al.* Ultrasmooth Polydopamine Modified Surfaces for Block Copolymer Nanopatterning on Flexible Substrates. *ACS Applied Materials & Interfaces* **8**, 7456-7463, doi:10.1021/acsami.6b00626 (2016).

50 Tran, N. T. *et al.* Polydopamine and Polydopamine–Silane Hybrid Surface Treatments in Structural Adhesive Applications. *Langmuir* **34**, 1274-1286, doi:10.1021/acs.langmuir.7b03178 (2018).

51 d'Ischia, M., Napolitano, A., Ball, V., Chen, C.-T. & Buehler, M. J. Polydopamine and Eumelanin: From Structure–Property Relationships to a Unified Tailoring Strategy. *Accounts of Chemical Research* **47**, 3541-3550, doi:10.1021/ar500273y (2014).

52 Wünsche, J. *et al.* Protonic and Electronic Transport in Hydrated Thin Films of the Pigment Eumelanin. *Chemistry of Materials* **27**, 436-442, doi:10.1021/cm502939r (2015).

53 Chio, S.-S., Hyde, J. S. & Sealy, R. C. Paramagnetism in melanins: pH dependence. *Archives of Biochemistry and Biophysics* **215**, 100-106, doi:https://doi.org/10.1016/0003-9861(82)90283-1 (1982).

54 Mostert, A. B. *et al.* Role of semiconductivity and ion transport in the electrical conduction of melanin. *Proceedings of the National Academy of Sciences* **109**, 8943 (2012).

55 Holten-Andersen, N. *et al.* pH-induced metal-ligand cross-links inspired by mussel yield self-healing polymer networks with near-covalent elastic moduli. *P Natl Acad Sci USA* **108**, 2651-2655, doi:10.1073/pnas.1015862108 (2011).

56 Holten-Andersen, N. *et al.* pH-induced metal-ligand cross-links inspired by mussel yield self-healing polymer networks with near-covalent elastic moduli. *Proceedings of the National Academy of Sciences* **108**, 2651 (2011).

57 Klosterman, L. J. *Deposition, Oxidation, and Adhesion Mechanisms of Conformal Polydopamine Films*, Carnegie Mellon University, (2016).

58 Charkoudian, L. K. & Franz, K. J. Fe(III)-coordination properties of neuromelanin components: 5,6-dihydroxyindole and 5,6-dihydroxyindole-2-carboxylic acid. *Inorg Chem* **45**, 3657-3664, doi:10.1021/ic060014r (2006).

59 Ryou, M. H., Lee, Y. M., Park, J. K. & Choi, J. W. Mussel-Inspired Polydopamine-Treated Polyethylene Separators for High-Power Li-Ion Batteries. *Adv Mater* **23**, 3066-+, doi:10.1002/adma.201100303 (2011).

60 Kim, B. H. *et al.* Mussel-Inspired Block Copolymer Lithography for Low Surface Energy Materials of Teflon, Graphene, and Gold. *Adv Mater* **23**, 5618-+, doi:10.1002/adma.201103650 (2011).

61 Ku, S. H., Lee, J. S. & Park, C. B. Spatial Control of Cell Adhesion and Patterning through Mussel-Inspired Surface Modification by Polydopamine. *Langmuir* **26**, 15104-15108, doi:10.1021/la102825p (2010).

62 Kang, K., Choi, I. S. & Nam, Y. A biofunctionalization scheme for neural interfaces using polydopamine polymer. *Biomaterials* **32**, 6374-6380, doi:10.1016/j.biomaterials.2011.05.028 (2011).

63 Liu, X. *et al.* Mussel-Inspired Polydopamine: A Biocompatible and Ultrastable Coating for Nanoparticles in Vivo. *Acs Nano* **7**, 9384-9395, doi:10.1021/nn404117j (2013).

64 Xing, Y., Zhang, J., Chen, F., Liu, J. & Cai, K. Mesoporous polydopamine nanoparticles with co-delivery function for overcoming multidrug resistance via synergistic chemo-photothermal therapy. *Nanoscale* **9**, 8781-8790, doi:10.1039/C7NR01857F (2017).

65 Zhu, Z. & Su, M. Polydopamine Nanoparticles for Combined Chemo- and Photothermal Cancer Therapy. *Nanomaterials* **7**, 160, doi:10.3390/nano7070160 (2017).

66 Wang, Y. *et al. Hollow polydopamine colloidal composite particles: Structure tuning, functionalization and applications*. Vol. 513 (2017).

67 Zhai, Y., Whitten, J. J., Zetterlund, P. B. & Granville, A. M. Synthesis of hollow polydopamine nanoparticles using miniemulsion templating. *Polymer* **105**, 276-283, doi:https://doi.org/10.1016/j.polymer.2016.10.038 (2016).

68 Xue, P. *et al.* PEGylated polydopamine-coated magnetic nanoparticles for combined targeted chemotherapy and photothermal ablation of tumour cells. *Colloids and Surfaces B: Biointerfaces* **160**, 11-21, doi:https://doi.org/10.1016/j.colsurfb.2017.09.012 (2017).

69 Chang, D. *et al.* Polydopamine-based surface modification of mesoporous silica nanoparticles as pH-sensitive drug delivery vehicles for cancer therapy. *Journal of Colloid and Interface Science* **463**, 279-287, doi:https://doi.org/10.1016/j.jcis.2015.11.001 (2016).

70 Sunoqrot, S., Hasan, L., Alsadi, A., Hamed, R. & Tarawneh, O. Interactions of mussel-inspired polymeric nanoparticles with gastric mucin: Implications for gastro-retentive drug delivery. *Colloids and Surfaces B: Biointerfaces* **156**, 1-8, doi:https://doi.org/10.1016/j.colsurfb.2017.05.005 (2017).

71 Batul, R., Tamanna, T., Khaliq, A. & Yu, A. Recent progress in the biomedical applications of polydopamine nanostructures. *Biomaterials Science* **5**, 1204-1229, doi:10.1039/C7BM00187H (2017).

72 Lee, M. *et al.* Water Detoxification by a Substrate-Bound Catecholamine Adsorbent. *Chempluschem* **77**, 987-990, doi:10.1002/cplu.201200209 (2012).

73 Park, H. A., Kim, Y. J., Kwon, I. S., Klosterman, L. & Bettinger, C. J. Lithium purification from aqueous solutions using bioinspired redox-active melanin membranes. *Polym Int* **65**, 1331-1338, doi:10.1002/pi.5184 (2016).

74 Kanitthamniyom, P. & Zhang, Y. Application of polydopamine in biomedical microfluidic devices. *Microfluidics and Nanofluidics* **22**, 24, doi:10.1007/s10404-018-2044-6 (2018).

75 Peattie, A. M., Majidi, C., Corder, A. & Full, R. J. Ancestrally high elastic modulus of gecko setal β-keratin. *Journal of the Royal Society Interface* **4**, 1071-1076, doi:10.1098/rsif.2007.0226 (2007).

76 Persson, B., Albohr, O., Tartaglino, U., Volokitin, A. & Tosatti, E. On the nature of surface roughness with application to contact mechanics, sealing, rubber friction and adhesion. *Journal of Physics: Condensed Matter* **17**, R1 (2004).

77 Abbott, S. *Adhesion Science: Principles and Practice*. (DEStech Publications, Incorporated, 2015).

78 Autumn, K. & Gravish, N. Gecko adhesion: evolutionary nanotechnology. *Philosophical Transactions of the Royal Society of London A: Mathematical, Physical and Engineering Sciences* **366**, 1575-1590 (2008).

79 Autumn, K., Dittmore, A., Santos, D., Spenko, M. & Cutkosky, M. Frictional adhesion: a new angle on gecko attachment. *Journal of Experimental Biology* **209**, 3569 (2006).

80 Persson, B. N. J. On the mechanism of adhesion in biological systems. *The Journal of Chemical Physics* **118**, 7614-7621, doi:10.1063/1.1562192 (2003).

81 Kamperman, M., Kroner, E., del Campo, A., McMeeking Robert, M. & Arzt, E. Functional Adhesive Surfaces with "Gecko" Effect: The Concept of Contact Splitting. *Advanced Engineering Materials* **12**, 335-348, doi:10.1002/adem.201000104 (2010).

82 Northen, M. T., Greiner, C., Arzt, E. & Turner, K. L. A Gecko-inspired reversible adhesive. *Adv Mater* **20**, 3905-3909 (2008).

83 Majidi, C. S. *Enhanced friction and adhesion with biologically inspired fiber arrays*. (University of California, Berkeley, 2007).

84 Baik, S. *et al.* A wet-tolerant adhesive patch inspired by protuberances in suction cups of octopi. *Nature* **546**, 396, doi:10.1038/nature22382

https://www.nature.com/articles/nature22382#supplementary-information (2017).

Chapter 2

Texture Dependent Adhesion in PDA

2.1 Introduction

2.1.1. Background

PDA film growth is a two-part process, where the three-dimensional island growth on the substrate surface is accompanied by concurrent bulk solution phase production of secondary grains with dimensions up to several hundred nanometers (**Figure 2.1**).[1,2]

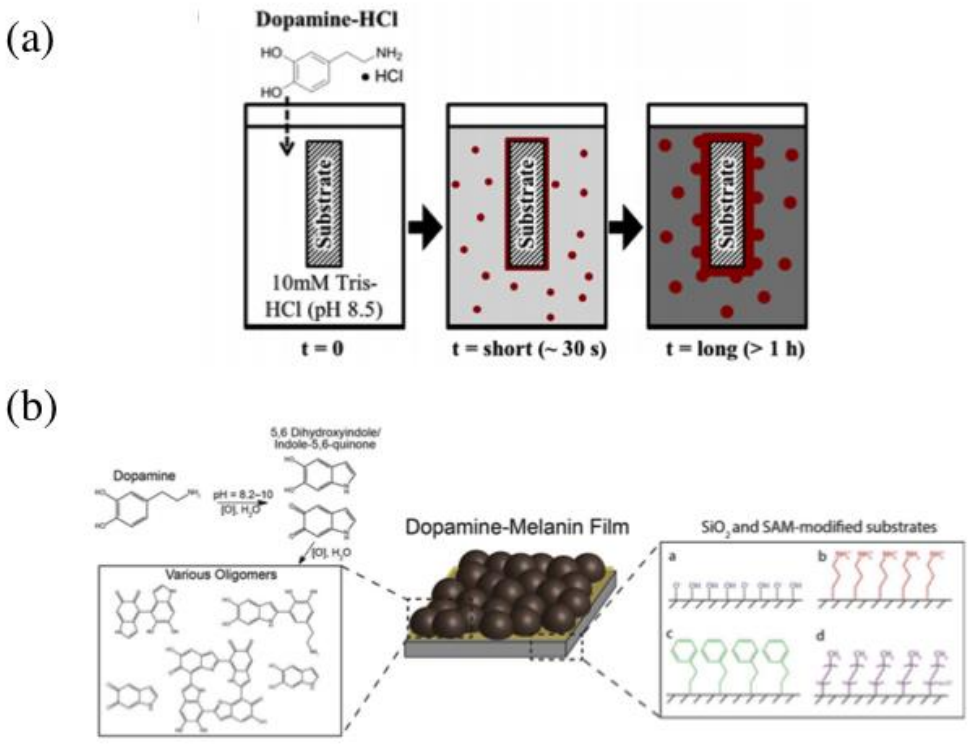

Figure 2.1: Mechanism of PDA film growth. a) PDA film growth is a two-part process where the film growth is accompanied by the bulk solution phase growth. b) Three-dimensional nature of the film growth on the substrates. Reproduced from [1,2]

Development of mound structures in the film and adsorption of bulk phases as time passes result in the rougher PDA surface with increasing synthesis time. The observed heterogeneity in PDA

film surfaces suggests that the macroscopic adhesion of PDA will be impacted with this inevitable heterogeneity on PDA surfaces[3] and calls for a need for systematic investigation of the impact of these heterogeneities to PDA adhesion for the purpose of both PDA adaptation in reversible adhesive applications and more fundamental studies. A possibility of tuning adhesion of PDA film with synthesis condition exists as well.

An indirect evidence for the assertion already exists in the literature. While reporting a method to create free-standing PDA nanomembranes from the PDA films deposited onto SiO_2 substrates, Klosterman et al. observed that there is a considerable contrast in morphology between the two sides of the PDA membrane; a side originally facing the substrate was much smoother than the other side (**Figure 2.2**).[4]

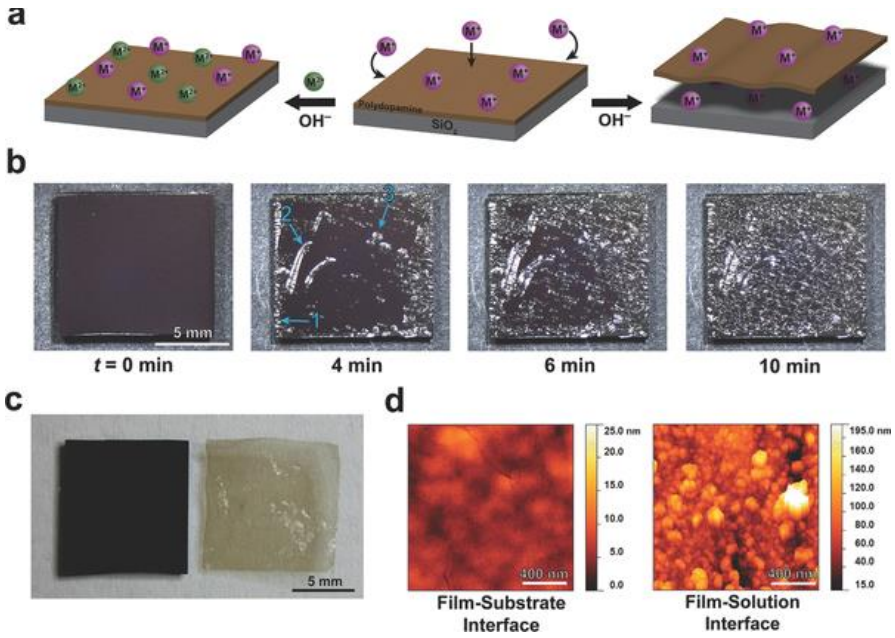

Figure 2.2: Preparation of free-standing PDA nanomembranes. a) Incubation of PDA films on SiO_2 substrates in alkaline monovalent salt solution (200mM NaCl + 50mM Tris buffer at pH = 9.5) results in delamination. b) Time lapse of PDA film delamination. c) Image of a delaminated PDA film. d) AFM images of the two surfaces of the delaminated PDA nanomembrane. Reproduced from [4]

A smoother side rapidly adhered onto the PDMS block upon application of pressure underwater, but the other side did not laminate onto the PDMS block; however, no quantification of the degree of differential in adhesion between two sides was made, and there is a significant neglect for role of surface roughness in studying PDA's adhesion in the literature. In order to systematically investigate the role of texture (surface roughness) in PDA adhesion, micro-indentation measurements using elastomeric lenses were done both in air and in water.

2.1.2 Review of JKR Contact Mechanics

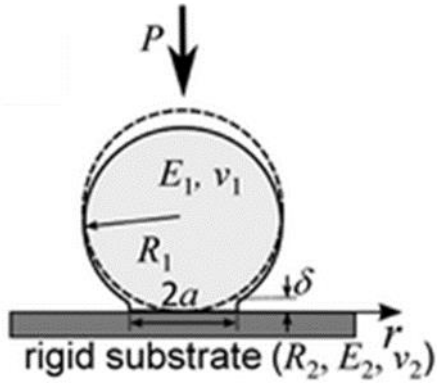

Figure 2.3: Schematic of JKR Experiment. Reproduced from [5]

Johnson-Kendall-Roberts (JKR) contact mechanics describes the deformation of two elastic solids that touch each other, with at least one of the bodies being spherical in shape. JKR equations are derived based on finding mechanical equilibrium between adhesive forces and the bulk deformation of the elastic material.[6] Derivation of JKR equations can be found in [7] and is not covered here. When a hemispherical lens with the elastic modulus of E_1 and the radius of R is brought into contact with a flat substrate with the modulus of E_2, the combined elastic modulus (E^*) ($\frac{1}{E^*} = \frac{v_1}{E_1} + \frac{v_2}{E_2}, v = poisson'sratio$), the energy release rate (surface energy required to increase or decrease contact area between two bodies) (G), the contact area radius (a), the force

(F) and the indentation depth (δ) follows the following relations according to JKR contact mechanics (**Figure 2.3**):

$$a^3 = \frac{3R}{4E^*}\left[F + 3\pi RG + \sqrt{6\pi RGF + (3\pi RG)^2}\right] \quad \text{Eqn. 2.1}$$

$$\delta = \frac{a^2}{R} - \sqrt{\frac{2\pi aG}{E^*}} \quad \text{Eqn. 2.2}$$

Combing Eqn. 2.1 and 2.2,

$$\delta = \frac{\frac{3R}{4E^*}\left[F+3\pi RG+\sqrt{6\pi RGF+(3\pi RG)^2}\right)^{\frac{2}{3}}}{R} - \sqrt{\frac{2\pi\left(\frac{3R}{4E^*}\left[F+3\pi RG+\sqrt{6\pi RGF+(3\pi RG)^2}\right)^{\frac{1}{3}}G\right)}{E^*}} \quad \text{Eqn. 2.3}$$

Fitting of a vs F data or δ vs F data to equation 2.1 or 2.3 respectively permits the recovery of G between two surfaces. For the equilibrium case, G is equal to the thermodynamic work of adhesion (W_{ad} or $\Delta\gamma$ depending on the nation) between two surfaces, and this permits the direct comparison of G acquired from JKR experiment with the surface tension data acquired from liquid probe contact angle measurements.

JKR contact mechanics embodies following assumptions:[8]

1. The system is in mechanical equilibrium.
2. The contact deformation is small compared to the size of the bodies (a << R).
3. The Tabor parameter ($\mu = \left(\frac{RW_{\mathrm{ad}}^2}{\frac{16}{9}E^{*2}z_0^3}\right)$; z_0= equilibrium separation distance of the atoms on the surfaces of the contact bodies, approximately ≈ 0.3 nm for many interactions) is greater than 5.
4. The contact is frictionless, meaning interface supports no shear stress and only normal stress is transmitted between the bodies.

The slight deviation from the last assumption often makes no or practically very little difference, but sometimes poses a problem if the contact is very rough. But if one of the material is soft and mean asperity height of the roughness is less than 100 nm, instead of invalidating JKR contact

mechanics, the effect of roughness materializes as the decrease in the apparent work of adhesion that one measures from the JKR micro-indentation tests.[9] This effect of reduction in adhesion due to surface roughness can be explained considering contact mechanics theories, which are covered in the next section.

2.1.3 Review of Contact Mechanics Theories

There are no exact and complete theories for the elastic contact between rough surfaces, but some theories are regarded as good theoretical basis to analyze elastic contact of random surfaces with Gaussian distribution of roughness.

The power spectral density (PSD) of a surface is a statistical tool that decomposes roughness in surfaces into spectral frequencies (wavevectors) and is a starting point for most mathematical treatments of surface roughness. PSD is defined as:[10]

$$C(\boldsymbol{q}) = \frac{1}{(2\pi)^2}\int d^2x < h(\boldsymbol{x})h(0) > e^{-iqx} \qquad \text{Eqn. 2.4}$$

Here $\boldsymbol{x} = (x, y)$, and $z = h(x)$ is the surface height measured from the arbitrary plane of choice such that $< h > = 0$. <…> is the ensemble averaging or spatial averaging over a reference point assuming translation invariance (the choice of a reference point doesn't affect the statistical property of the surface). $< h(\boldsymbol{x})h(0) >$, termed autocorrelation function is defined as:[10]

$$< h(\boldsymbol{x})h(0) > = \lim_{L\to\infty} \int_{-\frac{L}{2}}^{\frac{L}{2}} dx_0 \int_{-\frac{L}{2}}^{\frac{L}{2}} dy_0 h(x_0 + x, y_0 + y)h(x_0, y_0) \qquad \text{Eqn. 2.5}$$

Here L is the size of the substrate. With translational invariance, $C(\boldsymbol{q})$ only depends on the magnitude of the wavevector $\boldsymbol{q}$ ($q = |\boldsymbol{q}|$). For the case of randomly rough surfaces that follows Gaussian distribution, which often is a good estimation for many surfaces with random features, the statistical properties of the surfaces are completely described with $C(q)$. In this case, many

roughness related parameters can be easily defined using C(q). The root mean square (RMS) roughness (h_{rms}) can be defined as:[11,12]

$$h_{\text{rms}} = \sqrt{< h^2 >} = \int d^2 q C(q) = \left(2\pi \int_0^\infty dq q C(q)\right)^{\frac{1}{2}} \qquad \text{Eqn. 2.6}$$

The RMS gradient (h'_{rms}) as:

$$h'_{\text{rms}} = \sqrt{< |\nabla h|^2 >} = \left(2\pi \int_0^\infty dq q^3 C(q)\right)^{\frac{1}{2}} \qquad \text{Eqn. 2.7}$$

These PSD treatments are starting points of many of the contact mechanics theories.

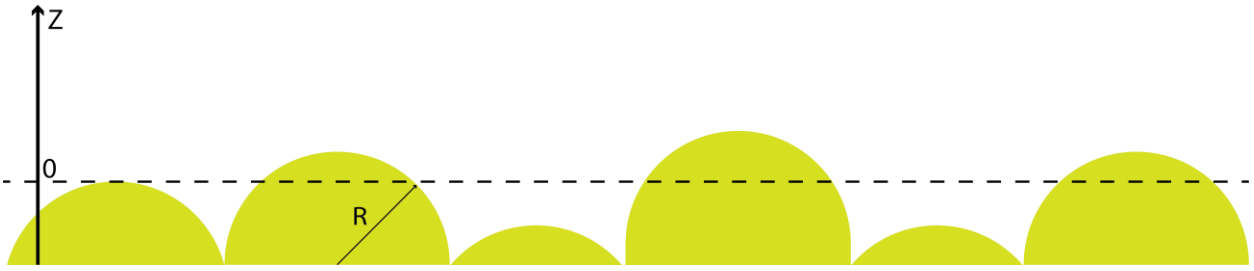

Figure 2.4: Schematic of the Greenwood-Williamson model assumptions. Surface roughness asperities are assumed as spherical asperities with the same radius with different height distributions.

Greenwood-William (GW) theory is by far the most widely used framework to analyze the effect of surface roughness due to its relative simplicity compared to other more sophisticated models. Derivation of JKR equations can be found in [13] and is not covered here. GW theory assumes the surface roughness to occur on a single length scale such that each asperity could be represented with a sphere of radius of *R*, and the height of the asperities (*h*) vary with the Gaussian distribution:[13]

$$P_h(h) = \frac{1}{\sqrt{2\pi}\sigma} e^{-\frac{h^2}{2\sigma^2}} \qquad \text{Eqn. 2.9}$$

where σ is the root mean square of the asperity height. According to GW model, when two surfaces come into contact, (one with roughness (rigid) and other perfectly smooth (soft)), if the

separation between two surfaces is denoted by *d*, an asperity with height $h > d$ will make contact with other plane.[13] Using Hertz contact theory, the normalized area of real contact at the separation *d* is:[14]

$$\frac{\Delta A}{A_0} = \pi n_0 R \int_d^\infty dh\,(h-d)P_h \qquad \text{Eqn. 2.10}$$

where A_0 is the nominal contact area between two surfaces, and n_0 is the number of asperities per unit area. The number of asperities making contact (*N*) can be denoted as:

$$N = A_0 n_0 \int_d^\infty dh P_h \qquad \text{Eqn. 2.11}$$

However, described relation is derived assuming no adhesion between two surfaces. GW theory considering adhesion was established by Fuller and Tabor using JKR theory instead of Hertz theory to analyze the asperity interaction to other surface.[15] Assuming the flat-geometries of interacting bodies, the resultant equations for force during unloading per unit area (*F*) at the surface separation *d*, assuming all the relevant contacts have occurred is:[9,16]

$$F(d) = \frac{n_0}{\sqrt{2\pi}\sigma} \int_{\delta_c}^\infty f(\delta)\, exp\left[-\frac{(d-\delta)^2}{2\sigma}\right] d\delta \qquad \text{Eqn. 2.12}$$

$$f(\delta) \xrightarrow{\text{Numerically Solve}} \begin{cases} \delta = \frac{a^2}{R} - \sqrt{\frac{2\pi a \Delta\gamma}{E^*}} \\ f(a) = \frac{4E^* a^3}{3R} - \sqrt{8\pi E^* \Delta\gamma a^3} \end{cases} \qquad \text{Eqn. 2.13}$$

where $\delta_c = -\left(\frac{3}{4}\right)\pi^{\frac{2}{3}}\left(\frac{E^{*2}}{R\Delta\gamma^2}\right)^{\frac{1}{3}}$, E^* = combined elastic modulus of interacting bodies, $\Delta\gamma$ = work of adhesion between two surfaces, *R* = radius of the asperities, n_0 = the number of asperities per unit area, and $\sigma =$ root mean square of the asperities. From the minimum point in *F(d)* curve, it is possible to identify the pull-off force per unit area, and the pull-off force per unit area could be normalized with $1.5 n_0 \pi R \Delta\gamma$ to get the relative pull-off force, which could be directly com-

pared with the JKR spherical experiment results. However, the implementational difficulty with the Fuller-Tabor model is the determination of R and n_0; for the real surfaces, roughness occurs at various length scales and the abstraction of the real-surface to get corresponding R and n_0 values to fit the GW surface could be challenging. Nayak proposed the random-field process theory that could be used to determine the inputs for the GW theory from the PSD of the surfaces.[17] Inputs for the GW model can be calculated as:[18-20]

$$R = \frac{3\sqrt{\pi}}{8m_4} \qquad \text{Eqn. 2.14}$$

$$n_0 = \frac{m_4}{m_2 6\pi\sqrt{3}} \qquad \text{Eqn. 2.15}$$

$$\sigma = \sqrt{\left(1 - \frac{0.8968}{\alpha}\right) m_0} \qquad \text{Eqn.2.16}$$

$$\alpha = \frac{m_0 m_4}{m_2} \qquad \text{Eqn.2.17}$$

where $m_0, m_2, and\ m_4$ are the spectral moments of the surface defined as $m_0 = h_{\text{rms}}, m_2 = h'_{\text{rms}}, and\ m_4 = 2h''_{\text{rms}}$ (RMS curvature).

Despite the prevalent use of GW theory and its efficiency, its assumption of confining asperity geometry to a spherical shape with the single length-scale is often unrealistic as roughness asperities occur in many length-scales. Amongst mathematical representations of randomly rough surfaces, self-affine fractal surfaces are of particular interest since most naturally rough surfaces are nearly self-affine fractal, and the mathematical simplicity self-affine fractal surfaces permit. Surfaces have roughness at various length scales, and self-affine fractal surface has a property that if part of the surface is magnified, surface 'looks the same' before magnification, that is the statistical property is preserved under the scale transformation (**Figure 2.5**):

$$\boldsymbol{x} \rightarrow \boldsymbol{x}\zeta, \qquad z \rightarrow z\zeta^{\mathrm{H}} \qquad \text{Eqn. 2.18}$$

where $\boldsymbol{x} = (x, y)$, $\zeta =$ magnification factor, H = Hurst Eponent ($0 < \mathrm{H} < 1$), and $z = h(\boldsymbol{x})$.

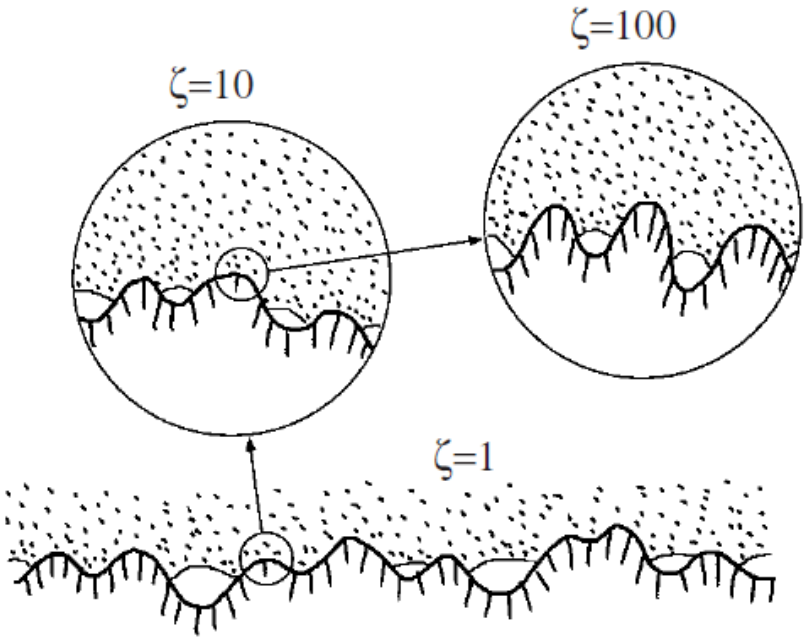

Figure 2.5: Schematic showing the translational invariance of self-affine fractal surfaces. Re-produced from [10]

For the case of self-affine surfaces, *C(q)* follows the power-law behavior:[10]

$$C(q) \sim q^{-2(H+1)} \qquad \text{Eqn. 2.19}$$

This relation holds within the finite wavevector region, $q_0 < q < q_1$, within which surface is considered self-affine fractal. q_1 describes the smallest length scale (largest wavector) associated with the roughness of the surface in question (typically assumed to be limited by the atomic spacing), and q_0 describes the largest length (smallest wavevector) scale associated with the roughness of the surface. Beyond q_0, *C(q)* is a constant until q_L, which is determined from the lateral size L from the scan size of the surface ($q_L = \frac{2\pi}{L}$) (**Figure 2.6**).

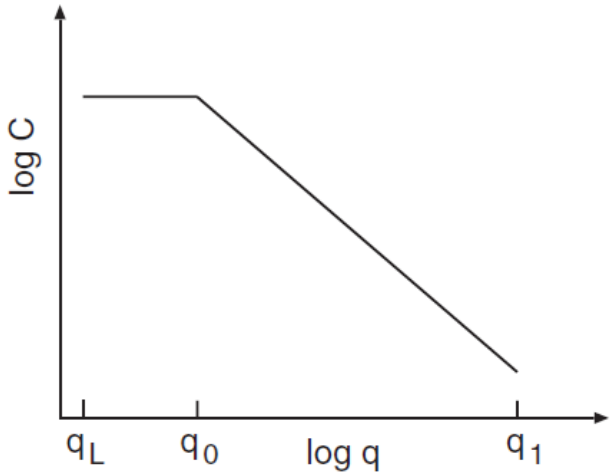

Figure 2.6: The surface roughness power spectrum of a surface that is self-affine fractal within the region $\boldsymbol{q_0 < q < q_1}$. Reproduced from [3]

All derivations and equations presented here can be found from [3] and [21]. When interacting two bodies have the length scale of $\lambda = L/\zeta$, with $q_L = \frac{2\pi}{L} and\ q = q_L\zeta$, $P(\sigma, \zeta)$ denotes the distribution of stress at the magnification ζ. Assume that one body is a rigid body with surface roughness that won't deform, and the other body is an elastic body with modulus of *E* and poisson's ratio of υ and is perfectly smooth. Persson theoretically derived that the stress distribution under this condition satisfies the diffusion like differential equation:[21]

$$\frac{\partial P}{\partial \zeta} = f(\zeta)\frac{\partial^2 P}{\partial \sigma^2} \qquad \text{Eqn. 2.20}$$

where $f(\zeta) = G'(\zeta)\sigma_0^2$, with σ_0 being average pressure in the nominal contact area ($\frac{F}{A_0}$), and $G'(\zeta)$, derivative of the function:

$$G(\zeta) = \frac{\pi}{4}\left(\frac{E^*}{\sigma_0}\right)^2 \int_{q_L}^{\zeta q_L} dq q^3 C(q) \qquad \text{Eqn. 2.21}$$

where $E^* = E/(1-\upsilon^2)$. As this is equivalent to diffusion equation with time replaced by magnification, and distance by stress, with increasing magnification, $P(\sigma, \zeta)$ will become broader

and broader (**Figure 2.7**). The broadening of pressure distribution with increasing magnification has to do with the nature of using *C(q)* in analyzing surface roughness. *C(q)* has an effect that it singles out spatial frequencies that at a specific magnification q ($q = \frac{2\pi}{\lambda}, \lambda = \frac{L}{\zeta}$), the mathematical treatment neglects all the surface features at higher magnifications than a current magnification. For example, at $\zeta = 1$, mathematically, surface is being treated as perfectly flat that the contact is made in whole nominal contact area, but with increasing magnification, the area of apparent contact decreases.

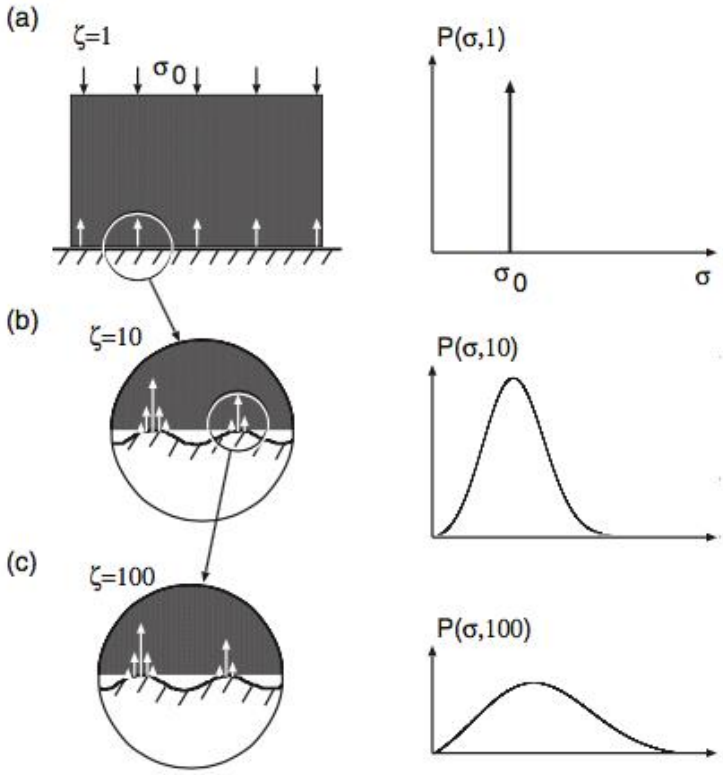

Figure 2.7: The stress distribution in the contact region between a rigid half-space and an elastic substrate at different magnifications. At the lowest magnification, the substrate looks perfectly smooth and the full (apparent) contact is made between two bodies, but with increasing magnification, the area of (apparent) contact decreases, with pressure distribution becoming broader. Reproduced from [10]

Combing back to the diffusion like Persson equation, when there is no adhesive interaction between bodies, the boundary condition is:

$$P(0,\zeta) = 0 \qquad \text{Eqn. 2.22}$$

indicating that the detachment occurs when the local stress reaches zero. At the lowest magnification ($\zeta = 1$), as there is no surface roughness (magnification here has the effect that it smoothens out features that are smaller than the current magnification):

$$P(\sigma,1) = \delta(\sigma - \sigma_0) \qquad \text{Eqn. 2.23}$$

Assuming only elastic deformation occurs, the ratio of actual contact area to nominal contact area at the magnification ζ is:[21]

$$P(\zeta) = \frac{A(\zeta)}{A_0 = A(L)} = \int_0^\infty d\sigma\, P(\sigma,\zeta) \qquad \text{Eqn. 2.24}$$

with the boundary conditions, $P(0,\zeta) = 0$ and $P(\infty,\zeta) = 0$, and the initial condition $P(\sigma,1) = \delta(\sigma - \sigma_0)$. Persson showed that:

$$P(\zeta) = \frac{2}{\pi}\int_0^\infty dx\, \frac{sinx}{x}\, e^{-\left(x^2 G(\zeta)\right)} = \text{erf}\left(\frac{1}{2\sqrt{G}}\right) \qquad \text{Eqn. 2.25}$$

The actual contact area (physical contact area) corresponds to the case where the magnification is the highest or when $q = q_1$. In this case:[22]

$$G(\zeta_{max}) = \frac{\pi}{4}\left(\frac{E^*}{\sigma_0}\right)^2 \int_{q_L}^{\zeta_{max} q_L = q_1} dq q^3 C(q) = \frac{\pi}{4}\left(\frac{E^*}{\sigma_0}\right)^2 * \left(\frac{{h'_{rms}}^2}{2\pi}\right) = \frac{1}{8}\left(\frac{E^*}{\sigma_0}\right)^2 {h'_{rms}}^2 \qquad \text{Eqn. 2.26}$$

$$P(\zeta_{max}) = \text{erf}\left(\frac{1}{2\sqrt{G(\zeta_{max})}}\right) = \text{erf}\left(\frac{\sqrt{2}\sigma_0}{E^* h'_{rms}}\right) \qquad \text{Eqn 2.27}$$

Thus the strong dependence of the actual contact area to $E^*, \sigma_0, and\ h'_{\text{rms}}$ can be shown.

When there is adhesive interaction, the tensile stress can be supported. In this situation, the boundary conditions and initial condition is:

$$P(-\sigma_a(\zeta),\zeta) = 0, P(\infty,\zeta) = 0, P(\sigma,1) = \delta(\sigma - \sigma_0) \qquad \text{Eqn. 2.28}$$

Here $\sigma_a(\zeta)$ is the stress necessary to induce detachment of width $\lambda = \frac{L}{\zeta}$ and can be defined as:[3]

$$\sigma_a(\zeta) = \left[\frac{\gamma_{eff}(\zeta)E^* q}{2}\right]^{\frac{1}{2}} \qquad \text{Eqn. 2.29}$$

$P(\zeta)$ can be written as:

$$P(\zeta) = \int_{-\sigma_a(\zeta)}^{\infty} d\sigma\, P(\sigma,\zeta) = 1 - \int_1^{\zeta} d\zeta' S(\zeta') \qquad \text{Eqn. 2.30}$$

$S(\zeta)$ is the function that satisfies the following linear integral equation derived from subjecting diffusion like differential equations to the boundary and initial conditions for the adhesive interaction:

$$\left[\int_1^{\zeta} d\zeta' S(\zeta') \left(\frac{a(\zeta)}{a(\zeta)-a(\zeta')}\right)^{\frac{1}{2}}\right] * \exp\left(-\frac{[\sigma_a(\zeta)-\sigma_a(\zeta')]^2}{4[a(\zeta)-a(\zeta')]}\right) = \exp\left(-\frac{[\sigma_a(\zeta)+\sigma_0]^2}{4(a(\zeta))}\right) \text{Eqn. 2.31}$$

where

$$a(\zeta) = \int_1^{\zeta} d\zeta' f(\zeta') \qquad \text{Eqn. 2.32}$$

The apparent surface energy at the magnification ζ, $\gamma_{\text{eff}}(\zeta)\ or\ \gamma_{\text{eff}}(q)$ $(q = \zeta q_L)$ takes the form:

$$\frac{\gamma_{\text{eff}}(q)}{\Delta\gamma} = \frac{P(q_1)}{P(q)} \int_0^{\infty} dx\, (1+\xi^2 x)^{\frac{1}{2}} e^{-x} - \frac{2\pi}{\delta} \int_q^{q_1} dq q^2 \frac{P(q)}{P(q_1)} C(q) \qquad \text{Eqn. 2.33}$$

where $\Delta\gamma$ is the actual surface energy change (when there is no surface roughness), $\delta = \frac{4\Delta\gamma}{E^*}$, $\xi = \int d^2 q q^2 C(q)$.

At $\zeta = 1$, $q = q_L$, and $\gamma_{\text{eff}}(q_L)$ is the apparent work of adhesion that is measured from the experiment. At this magnification, equation 2.33 becomes:

$$\frac{\gamma_{\text{eff}}(q_L)}{\Delta\gamma} = P(q_1) \int_0^{\infty} dx\, (1+\xi^2 x)^{\frac{1}{2}} e^{-x} - \frac{2\pi}{\delta} \int_{q_L}^{q_1} dq q^2 \frac{P(q)}{P(q_1)} C(q) \qquad \text{Eqn. 2.34}$$

$P(q_1)$ is the ratio of physical actual contact area to the nominal contact area or probability that the contact would occur at the smallest length scale, and $\int_0^\infty dx\,(1+\xi^2 x)^{\frac{1}{2}}e^{-x}$ accounts for the increase in surface area due to roughness. $\frac{2\pi}{\delta}\int_{q_L}^{q_1} dqq^2\frac{P(q)}{P(q_1)}C(q)$ is the elastic energy stored at the interface. Thus, the equation presented is the mathematical expression for the relation:

$$\gamma_{\text{eff}} = \frac{A}{A_0}\Delta\gamma - \frac{U_{\text{el}}}{A_0} \qquad \text{Eqn. 2.35}$$

where actual contact area (probability of contact occurring * ratio of increased contact area to nominal projected area) is:

$$\frac{A}{A_0} = P(q_1)\int_0^\infty dx\,(1+\xi^2 x)^{\frac{1}{2}}e^{-x} \qquad \text{Eqn. 2.36}$$

and the elastic energy stored at the interface is:

$$\frac{U_{\text{el}}}{A_0} = \frac{\left[\frac{2\pi}{\delta}\int_{q_L}^{q_1} dqq^2\frac{P(q)}{P(q_1)}C(q)\right]}{\Delta\gamma} \qquad \text{Eqn. 2.37}$$

Thus, the apparent work of adhesion is affected by three factors: partial contact due to roughness, increase in area over the projected nominal area due to roughness, elastic energy stored at the interface due to roughness.

No analytical solution exists for $P(\zeta)$ and $\gamma_{\text{eff}}(\zeta)$, but they can be solved numerically by solving equation Eqn. 2.29 ~ 2.33 iteratively. A particular interest relevant to the experiment is $P(\zeta_{\max}) = P(q_1)$ and $\gamma_{\text{eff}}(1) = \gamma_{\text{eff}}(q_L)$, since they represent the actual physical contact ratio and the surface roughness effected apparent work of energy (*G*, energy release rate from the previous section) measured from the indentation experiment, respectively.

2.2 Methods

2.2.1 Materials

Dopamine hydrochloride (98%) was purchased from Sigma-Aldrich (St. Louis, MO USA) and used as received. Tris(hydroxymethyl) aminomethane (Tris) was purchased from Fisher Scientific (Hampton, NH USA) and used as received. Water was purified (18.2 MΩ-cm) using Direct-Q 3 UV-R system (Millipore). Silicon wafers with 1 μm thermal oxide were purchased from Silicon Quest International (San Jose, CA USA; 4" diameter, phosphorus doped). Sylgard 184 (Polydimethylsiloxane) was purchased from Dow Corning (Midland, MI USA). Borosilicate glass hemispherical probes were purchased from Edmund Optics (Barrington, NJ USA; 6mm diameter). UV Glue was purchased from Norland Product (Cranbury, NJ USA; Norland Optical Adhesive 81). Tridecafluoro – 1, 1, 2, 2-Tetrahydroctyl)-Trichlorosilane was purchased from Gelest (Morrisville, PA USA). Epoxy was purchased from Loctite (Düsseldorf, GER; Aqua Marine Epoxy). Sylgard 184 and 527 (Polydimethylsiloxane) were purchased from Dow Corning (Midland, MI USA).Ecofloex 00-30 was purchased from Smooth-On (Macungie, PA USA).

2.2.2 Free-standing PDA Nanomembrane for Contact Angle Goniometry Preparation

Silicon wafers with 1 μm thermal oxide (100 mm diameter, p-doped Si, Silicon Quest International, San Jose, CA, USA) were cleaned by sonication in acetone, followed by isopropyl alcohol and ddH_2O. Substrates were then treated with UV-ozone (5 min, 30 mW-cm^{-2}, Jelight, Irvine, CA, USA). PDA nanomembranes were prepared by incubating substrates in 2 mg/ml dopamine hydrochloride in 100 ml of 10 mM Tris buffer (Fisher Scientific, Hampton, NH, USA) in ambient air and orbital rotation (65 rpm). After 24 h, the substrates were rinsed with ddH_2O

and placed in 200 mM NaCl + 50 mM Tris buffer solution for > 6 h for film delamination. Free-standing delaminated nanomembranes were then transferred to ddH_2O prior to subsequent processing.

2.2.3 Transfer Printing of PDA Nanomembranes to Silicon Wafers

Freestanding PDA nanomembranes were placed in ddH_2O along with precleaned silicon wafers in petri dishes. PDA nanomembranes were positioned atop silicon substrates with either apical or basal side facing upward. The water level was reduced until PDA nanomembranes adhered to silicon substrates. PDA nanomembranes were then dried in a stream of N_2.

2.2.4 Measurement of Contact Angle on Apical/Basal Side Membranes on Silicon Wafers

All samples were dried under mild vacuum for 24 h prior to the water-in-air contact angle measurements. The contact angle measurements were done by placing probe liquid in the increment of 5 µl. The side view of the drop was taken using Rame-Hart Contact Angle Goniometer (Model 100-00-115, Succasunna, NJ USA). The following three liquid probes were used: ddH_2O, glycerol, and ethylene glycol.

2.2.5 PDA Samples for Micro-indentation Measurements Fabrication

PDA nanomembranes were prepared by incubating precleaned silicon substrates in 2 mg/ml dopamine hydrochloride in 100 ml of 10 mM Tris buffer in ambient air and under rotation (65 rpm). After 24 h, the substrates were rinsed with ddH2O. The PDA deposition process was repeated to prepare films with the desired roughness (24, 36, 48, or 72 h). Some samples were placed in 50 mM Tris HCl solution (pH = 8.5) and sonicated for 2 h. For the basal side sample fabrication, epoxy was deposited on PDA nanomembrane on a silicon wafer (24 h deposition; no sonication) and a glass slide was placed on top of it. Epoxy-PDA-Silicon stacks were placed in

200 mM NaCl + 50 mM Tris buffer solution at 50 °C for 4 h, and Epoxy-PDA was separated while in the buffer solution, and the sample was immersed in ddH2O for >24 h prior to performing adhesion measurements.

2.2.6 Morphological Characterization of PDA Samples

PDA nanomembranes roughnesses were measured using atomic force microscopy (NTegraAFM, NT-MDT, Tempe, AZ USA) in tapping mode. Scans were 50 um x 50 um at 0.5 Hz using tips with a reported radius of < 10 nm (Budget Sensors, Sofia Bulgaria; k = 40 N/m). AFM data using Gwyddion AFM software (http://gwyddion.net/) and surface topography analyzer (http://contact.engineering/).

2.2.7 PDMS and Ecoflex Lens Fabrication

Molds for elastomeric lenses were created by using 6 mm diameter borosilicate glass hemispherical lenses and Norland Optical Adhesive 81 UV Glue. Fabricated molds were immersed in a solution made by combining 10 ml of trichloroethylene and 12 µl of (tridecafluoro-1,1,2,2-tetrahydroctyl)-trichlorosilane (Gelest, Morrisville, PA USA) for 16 h, followed by sonication in isopropyl alcohol, and then ddH2O and dried under an N2 stream. Ecoflex precursor was made by mixing part A and part B of Ecoflex 00-30 at a 1:1 ratio, degassing (< 2 Torr, 2 min; 3 cycles), casting, and curing at 60 °C for 30 min. PDMS solution was created by mixing Sylgard 527 gel and Sylgard 184 elastomer. Sylgard 527 blend was prepared by mixing equal weight of part A and part B and degassed (< 2 Torr, 5 min; 3 cycles). Sylgard 184 blend was made by mixing 5 parts base to 1 part curing agent and underwent the same mixing and degassing procedure. Sylgard 527 blend and Sylgard 184 blend were mixed in 3:7 weight ratio, degassed (< 2 Torr, 10 min; 3 cycles), cast, and cured at 80 °C for 18h.

2.2.8 Micro-indentation Measurements

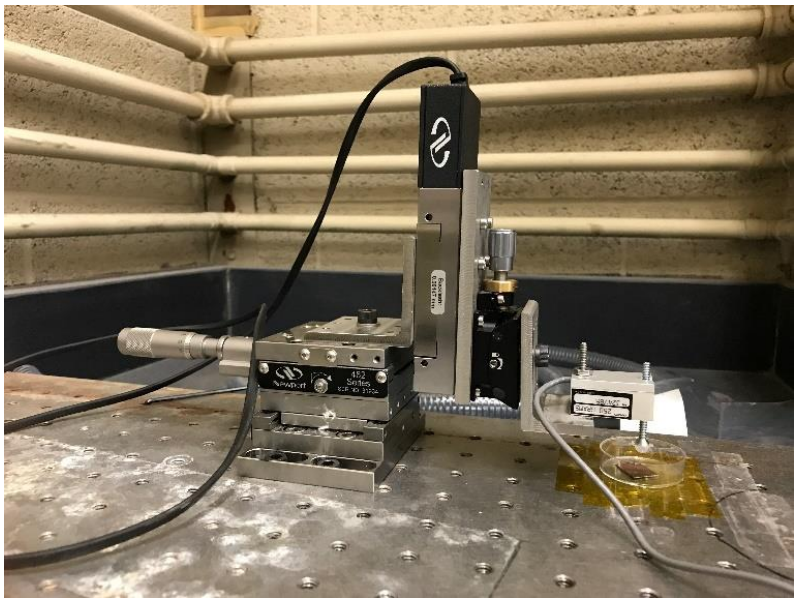

Figure 2.8: Macroscopic photo of custom-built indentation apparatus for adhesion measurements.

Custom-built micro-indentation appratus was used for the micro-indentation measurements (**Figure 2.8**). PDMS or Ecoflex lenses were mounted on a 25g load cell (GSO-25, Transducer Techniques, Temecular, CA USA), attached to a stack of a vertical motorized stage (MFA-CC, Newport Corporation, Irving, CA USA) for vertical motion and a manual tilting stage (GON40-L, Newport Corporation, Irving, CA USA) for alignment, motion of which was controlled by Newport ESP 301 motion stage (ESP 301; Newport Corporation, Irving CA). Custom written LabView software was used to control the stages. All measurements were performed at room temperature. Before the measurement, hemispherical lenses were rinsed in ethanol, dried under an N_2 stream, and air dried for >1 h. Hemispherical lenses (either PDMS or Ecoflex) were positioned over substrates at arbitrary heights and approached at a vertical speed of 0.5 µm/s until reaching a preload of 1 mN, then held in contact for 120 sec, and was retracted at 0.5 µm/s until the detachment occurred both in air and under water. During indentation, the lens force and displacement were simultaneously measured. The loading phase commences upon initial contact

between PDA samples and hemispherical lenses and concludes when the value for the preload is reached. The unloading phase starts after the holding phase and concludes when the pull-off force (maximum tensile force) is reached, beyond which point, the hemispherical lenses gradually jumped out of contact. The fit of the acquired data during loading phase was carried out in MATLAB (MathWorks®, Natick, MA, USA). The average value of the energy release rate acquired from the fit of the loading phase data is represented as mean ± s.d. unless otherwise stated.

2.2.9 Tension Measurement

PDMS and Ecoflex blocks were prepared by following the same composition and curing protocols as in 2.2.7, except using flat petri dishes as molds. After curing, PDMS and Ecoflex were fashioned into coupons with length, width, and thickness of ~20 mm, ~10 mm, and ~2 mm, respectively. Uniaxial tension experiments were conducted with a micro-tester (Instron 5943, Instron, Norwodd, MA USA) at room temperature. Samples were mounted in a uniaxial stress-strain configuration and deformed to nominal strains of ε = 10% at an elongation rate of 2 mm/min. The load and displacement were measured and stress-strain curves were recovered. Stress-strain curves were constructed and Young's moduli were extracted from the slope of the linear regions (ε < 10%).

2.3 Results and Discussion

2.3.1 Modulation of Nanoscale Texture of Polydopamine Nanomembranes

Freestanding PDA nanomembranes can be prepared by auto-oxidative polymerization of dopamine followed by modulated PDA substrate interactions through electrolyte incubation (**Figure 2.9a**).[23] Klosterman et al. qualitatively observed asymmetric adhesion in PDA nanomembranes: the surface facing the substrate during polymerization and deposition (termed the

basal side) exhibits increased underwater adhesion to PDMS compared to the opposite surface (apical side) of the same membrane.[23] Given the stark contrast in morphology reported between basal and apical sides, it was hypothesized that the contrast in texture between apical/basal sides is largely responsible for differential adhesion.[23] PDA nanomembranes were prepared on the substrates to preferentially expose either the apical or basal side of the film (**Figure 2.9b**). The morphology of apical sides was controlled by selecting the deposition time and employing sonication, where appropriate.[1] PDA nanomembranes with a broad range of textures could be prepared using these techniques (**Figure 2.9b**). The chemical homogeneity of apical and basal sides were assessed by contact angle. The apical and basal sides of freestanding PDA nanomembranes transfer-printed onto silicon wafers showed comparable values for interfacial surface tension as measured by an Owens-Wendt plot (**Figure 2.9c; See Appendix**). Furthermore, the interfacial surface energy of PDA was in agreement with previously reported values (**See Appendix**),[1,24] which suggests that the interfacial energy, and therefore the interfacial chemistry, of PDA nanomembranes is independent of both membrane orientation and electrolyte composition. Therefore, differential adhesion in PDA nanomembranes observed by Klosterman et al. is not likely attributed to chemical heterogeneity or partitioning. Further, surface roughness differential is therefore likely responsible for orientation-dependent adhesion in PDA nanomembranes. This assertion is supported by the large range in root mean square (RMS) roughness ($h_{rms,PDA}$) and RMS gradient ($h'_{rms,PDA}$) in PDA nanomembranes as a function of both PDA synthesis and PDA nanomembranes orientation (**Figure 2.9d and e**).

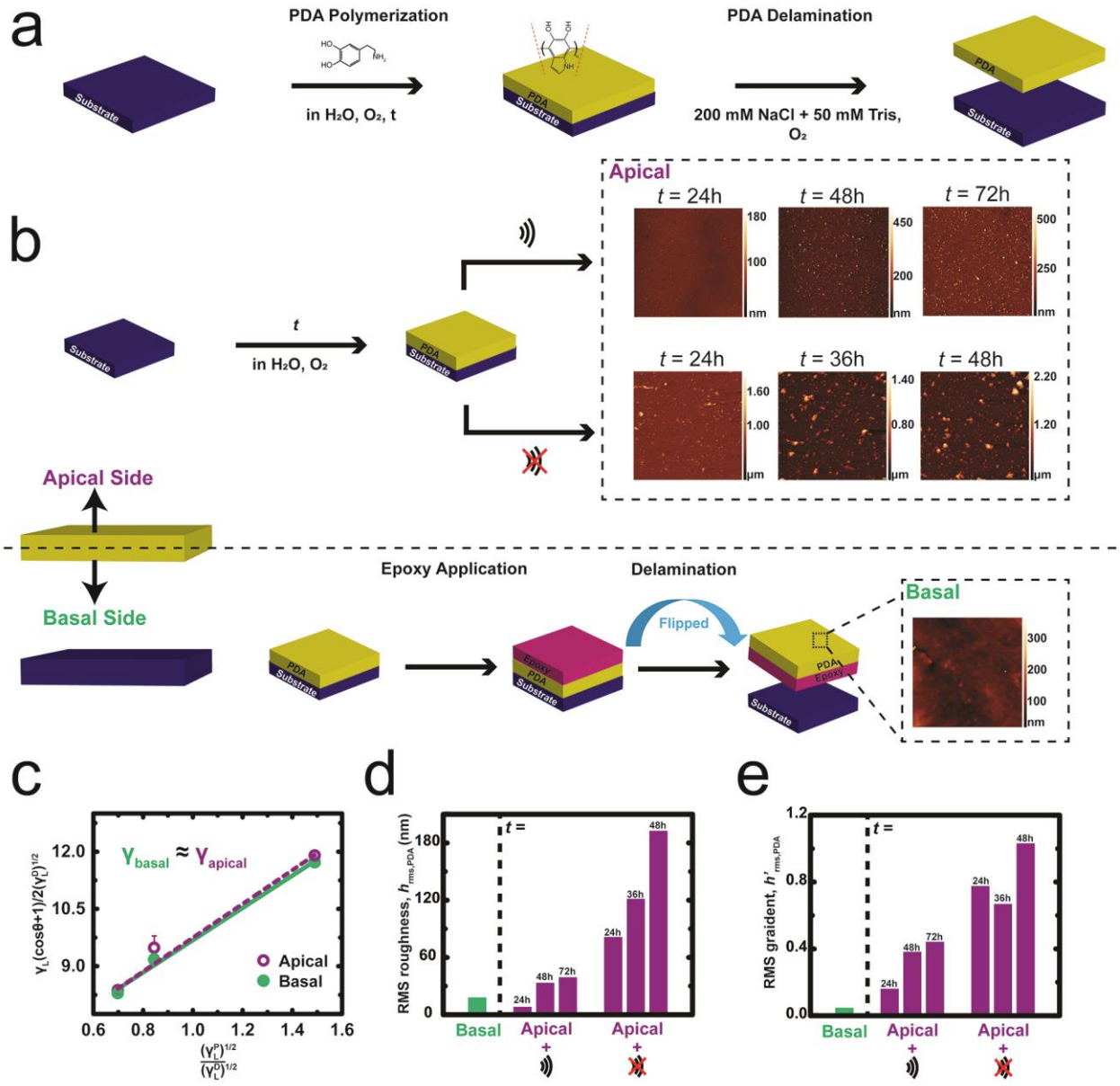

Figure 2.9: a) Schematic of freestanding PDA nanomembrane preparation procedure. Incubation of PDA prepared on SiO_2 in a weakly basic electrolyte results in the delamination of PDA nanomembranes. b) Schematic of preparation procedure and AFM images of apical/basal side PDA samples. AFM scan size is 50 x 50 μm^2. The surface originally facing the substrate before PDA delamination is termed the basal surface while the opposite is termed apical. The morphology of apical surfaces is controlled through PDA deposition times and sonication post-treatments. c) Owens-Wendt plot for basal/apical surfaces (**See Appendix**). Both surfaces exhibit comparable values for interfacial surface energy. Values for the (d) RMS roughness ($h_{rms,PDA}$) and (e) RMS gradient ($h'_{rms,PDA}$) of PDA nanomembranes as a function of synthesis condition and post-treatment.

2.3.2 Johnson-Kendall-Roberts Theory Formulation

The dependence of adhesion of PDA nanomembranes to their texture was characterized using micro-indentation tests between PDA nanomembranes on substrates and mechanically compliant hemispherical lenses composed of either PDMS or Ecoflex (**Figure 2.10a**). Given our chosen experimental conditions, indentation tests using either lenses are characterized by a Tabor parameter >> 1,[25] and these experiments generate force-displacement curves (**Figure 2.10a and b**) that can be analyzed by applying the Johnson Kendall Roberts (JKR) theory of elastic contact mechanics.[6,26-28] When a hemispherical lens with the elastic modulus of E_1 and the radius of R is brought into contact with a flat substrate of modulus E_2, the combined elastic modulus E^* can be expressed as follows:

$$\frac{1}{E^*} = \frac{1-\nu_1^2}{E_1} + \frac{1-\nu_2^2}{E_2} \qquad \text{Eqn. 2.38}$$

where, ν_1 and ν_2 are Poisson's ratios of the hemispherical lens and PDA nanomembranes. Since $E_2 >> E_1$, the combined modulus can be expressed as $E^* \approx \frac{E_1}{1-\nu_1^2}$. The force F, indentation depth δ, the work of adhesion (energy release rate between two surfaces) G are related as in Eqn. 2.3. Thus, for a given force-(indentation depth) (F vs δ) curve, the value of G and E^* between two surfaces can be determined by fitting δ and F with Eqn. 2.3. For the acquired experimental data for the current setup, the starting point of the probe before each experiment is arbitrary. Thus, an offset parameter δ_0 was introduced to Eqn. 2.3 to use experimentally acquired force-displacement curves ($\delta' = \delta + \delta_0$), which yields:

$$\delta' = \frac{\left(\frac{3R}{4E^*}\left[F+3\pi RG+\sqrt{6\pi RGF+(3\pi RG)^2}\right]\right)^{\frac{2}{3}}}{R} - \sqrt{\frac{2\pi\left(\left(\frac{3R}{4E^*}\left[F+3\pi RG+\sqrt{6\pi RGF+(3\pi RG)^2}\right]\right)^{\frac{1}{3}}G\right)}{E^*}} + \delta_0 \qquad \text{Eqn. 2.39}$$

Loading part of force-displacement data (from initial contact to hold) was fit using Eqn. 2.39 for all experimental conditions, where possible.

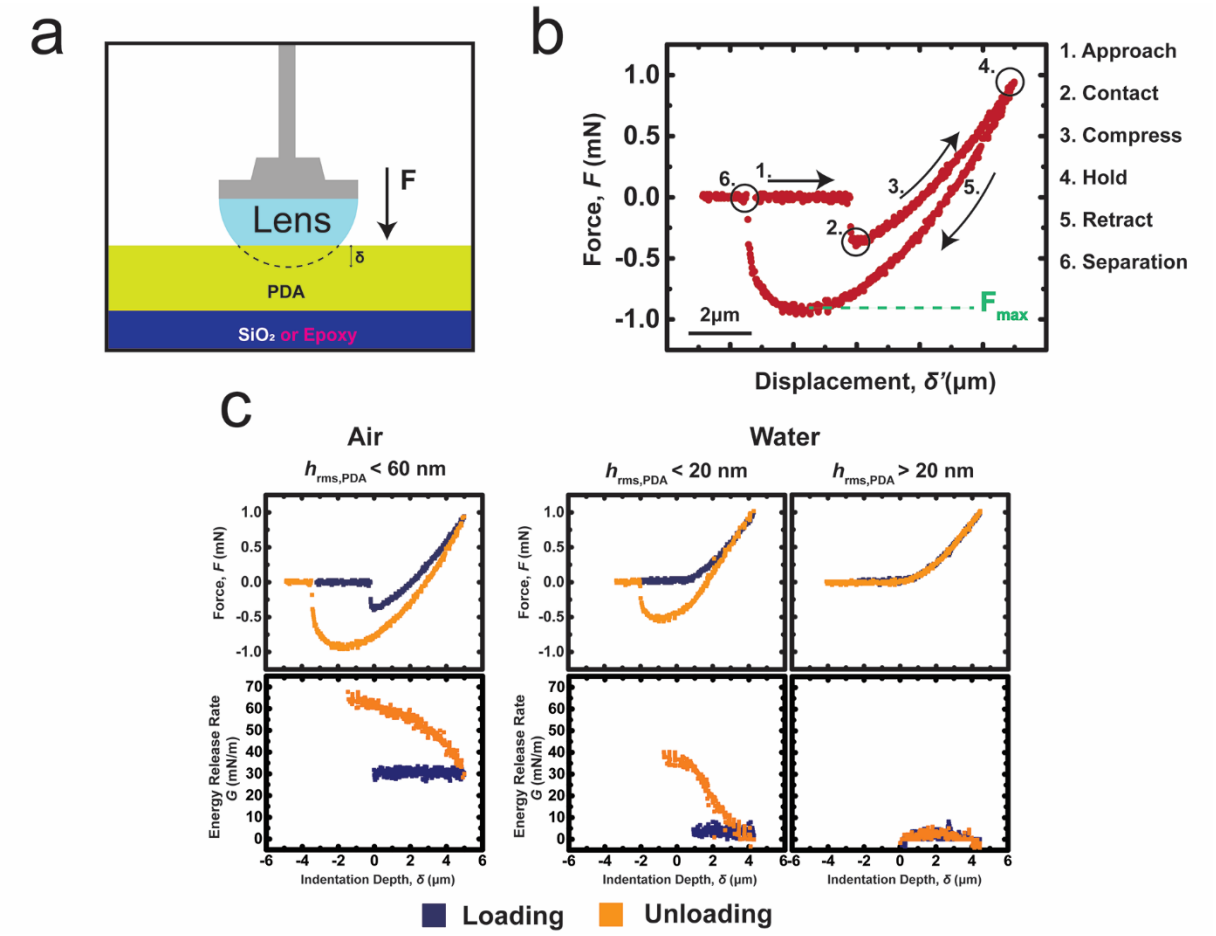

Figure 2.10: a) Schematic of micro-indentation measurements. Either PDMS or Ecoflex hemispherical lenses were indented against substrates with PDA nanomembranes. b) A representative force-displacement curve between a PDMS lens and substrates with PDA nanomembranes with various phases of contact labeled. c) Top: Representative force-(indentation depth) curves between PDMS lenses and PDA nanomembranes. Bottom: Representative energy release rate versus indentation depth plots for PDMS lenses. Left to Right: $h_{rms,PDA} < 60$ nm in air, $h_{rms,PDA} < 20$ nm underwater, and $h_{rms,PDA} > 20$ nm underwater.

2.3.3 Force-Displacement Measurements in Air

Eqn. 2.39 could be fit to the loading part of force-displacement curves acquired from indentation measurements between PDMS hemispherical lenses and PDA nanomembranes with $h_{rms,PDA} < 60$ nm in air ($R^2 > 0.995$). Values of E^*, G, and δ_0 could be calculated. For measure-

ments between PDMS hemispherical lenses and PDA nanomembranes with $h_{rms,PDA}$ < 60 nm, extracted values of G = 34 ± 4 mN/m (n = 7) were in agreement with thermodynamic calculations based on contact angle measurements (**see Appendix**). Extracted values for E^* agreed closely with the tensile measurements (**Figure 2.11**).

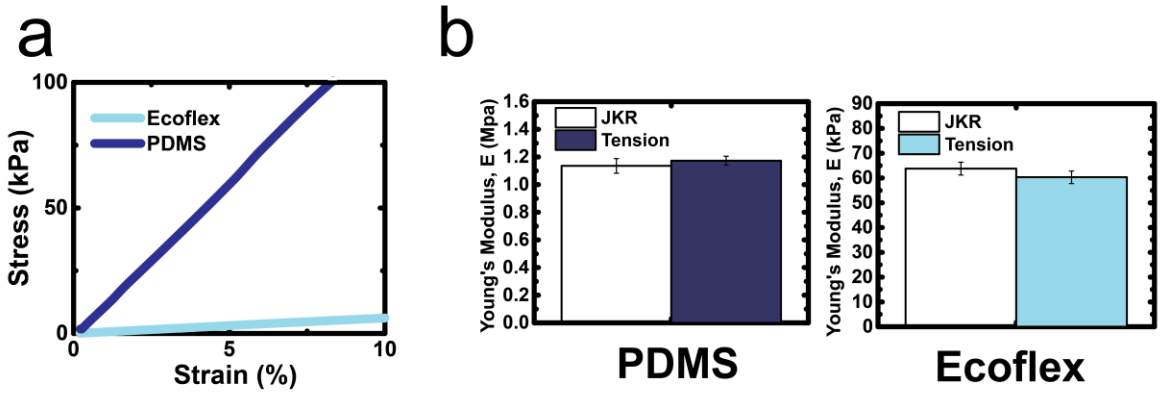

Figure 2.11: a) Representative stress-strain curves for PDMS and Ecoflex. b) Comparison between recovered Young's moduli calculated from both JKR and uniaxial tensile strain measurements (n = 3); $E_{PDMS,JKR}$ = 1.14 ± 0.05 MPa, $E_{Ecoflex,JKR}$ = 63.8 ± 2.6 kPa, $E_{PDMS,Tensile}$ = 1.17 ± 0.03 MPa, and $E_{Ecoflex,Tensile}$ = 60.3 ± 2.5 kPa.

Force-(indentation depth) curves can be constructed by subtracting δ_0 from displacement data. A representative force-(indentation depth) curve (F vs δ) is given for measurements between PDMS lenses and PDA nanomembranes with $h_{rms,PDA}$ < 60 nm in air (**Figure 2.10c**). With E^* and δ_0 values determined by fitting data from the loading phase to Eqn. 2.39, Eqn. 2.39 can then be solved numerically for both loading and unloading phases to obtain values for G. A representative plot of G vs δ for measurements between PDMS lenses and PDA nanomembranes with $h_{rms,PDA}$ < 60 nm in air is shown (**Figure 2.10c**). During the loading phase, G is nearly constant; an expected result for a thermodynamically equilibrated system.[29] During the unloading phase, plots of G vs δ show significant hysteresis. We conclude that bulk viscoelastic deformation is negligible as the fit of the force-displacement data during the loading phase to Eqn. 2.39 shows a good fit (R^2 > 0.995), which indicates that bulk deformation is largely elastic.[30] We speculate that

hysteresis between loading and unloading phases is attributed to interfacial dissipation, behavior that is qualitatively similar to those described in previous reports for PDMS lenses.[29-32] JKR theory suggests that the maximum force or pull-off force during unloading ($F_{\max}$) in a perfectly elastic response with the absence of surface roughness is related to the thermodynamic work of adhesion by $G_{\text{Thermo}} = \frac{F_{\max}}{1.5\pi R}$.[27] Even in cases where interfacial dissipation are non-negligible and surface roughness is present, the same expression $\left(\frac{F_{\max}}{1.5\pi R}\right)$ gives the effective work of adhesion(W_{UL}), a key figure of merit in measuring texture-dependent adhesion,[33] that could be used in our case for the cross-comparison between samples with different roughnesses. For measurements between PDMS lenses and PDA nanomembranes with $h_{\text{rms,PDA}} > 60$ nm in air, force-displacement curves in the loading phase do not permit the fit to Eqn. 2.39, which we attribute to the higher roughness of these samples (**See Appendix**). For measurements between Ecoflex lenses and PDA nanomembranes, regardless of $h_{\text{rms,PDA}}$ of PDA nanomembranes, the force-displacement curves during the loading phase show a good fit to Eqn. 2.39 with G value similar to that of PDMS (slightly smaller), and show a similar degree of hysteresis (**See Appendix**).

2.3.4 Interfacial Viscoelastic Effect in Air

Gent and Schulz proposed that when the bulk viscoelasticity is present, the energy release rate (G) at the crack-opening interface is the function of the crack front velocity as:[34]

$$G = G_0[1 + \varphi(a_{\text{T}}V)] \qquad \text{Eqn. 2.40}$$

where G_0 is the energy release rate at the zero crack-front velocity (i.e., the energy release rate without dissipative effect), a_{T} is the WLF shift factor,[35] and V is the crack front velocity. $\varphi(a_{\text{T}}V)$ is characteristic of the material and is independent of material geometry or loading system.[36] Knowledge of $\varphi(a_{\text{T}}V)$ allows the computation of dissipative effect accounted energy

release rate provided that the dissipative effect is confined to the crack tip. Maugis and Barquins found $\varphi(a_T V)$ to have the power-law like dependence:[37,38]

$$G = G_0[1 + k(a_T V)^n] \qquad \text{Eqn. 2.41}$$

where the typical value of n fall in the range $0.1 < n < 0.8$. The above relation has the origin in bulk viscoelasticity. For the case of interfacial viscoelastic dissipative effect, Barthel and Roux found that similar power-law like relation exists:[39]

$$G = G_0\left[1 + \left(\frac{V}{V_0}\right)^{\beta}\right] \qquad \text{Eqn. 2.42}$$

where V_0 is the characteristic velocity for the onset of dissipation. However, the above relation is a phenomelogical equation not justified with an explicit theory,[40] probably due to the various molecular origins of interfacial dissipative mechanisms.[41] Also need to be noted is that the Eqn. 2.42 is dependent on testing geometry or many other conditions unlike Eqn. 2.41.

V, crack-front velocity is the time derivative of contact radius. Time derivative can be taken to $\delta \; vs \; a$ relation in Eqn. 2.2 to relate the indentation speed to the crack front velocity:

$$\frac{d\delta}{dt} = \left[\frac{2a}{R} - \sqrt{\frac{\pi G}{2E^* a}}\right]\left(\frac{da}{dt}\right) \qquad \text{Eqn. 2.43}$$

In theory, Eqn. 2.43 could be used to get V ($\frac{da}{dt}$) throughout the unloading portion of data, and *G* vs *V* curve could be constructed to fit to Eqn. 2.42 to examine the dissipative effect for the system throughout the unloading phase. But in practice, when the adhesion hysteresis is involved, contact radius starts to decrease only after the displacement has sufficiently decreased to the point that where energy release rate becomes large enough,[42] and the use of Eqn. 2.42 is often only feasible for the measurement setups that can take measure the contact radius data. This sort

of artifact was observed in our system as well (data not shown), and the *G* vs *V* curve showed behavior in congruent with Eqn. 2.42 only for the portion of data with $\delta < 1\ \mu m$ for data in **Figure 2.10c** in air. Pressure dependent hysteresis could exist as well since different regions of contact experiences different pressure history.

Instead of arbitrary truncating data, the degree of viscoelasticity was analyzed at the time of pull-off in relation to values reported in the literature measured at the time of pull-off. Contact radius at the time of pull-off (a_c) has the characteristic form:[43]

$$a_c = \left(\frac{9\pi R^2 G}{8E^*}\right)^{\frac{1}{3}} \qquad \text{Eqn. 2.44}$$

Substituting a_c in Eqn. 2.43 to *a* in Eqn. 2.44:

$$\frac{d\delta}{dt} = \left[\frac{2a_c}{R} - \sqrt{\frac{\pi G}{2E^* a_c}}\right]\left(\frac{da}{dt}\right) \qquad \text{Eqn. 2.45}$$

Plugging in corresponding values to Eqn. 2.45 ($\frac{d\delta}{dt} = 0.5\ \mu m s^{-1}, G = 34\ mN m^{-1}, R = 3\ mm,$ $and\ E^* = 1.52\ MPa$), *V* ($\frac{da}{dt}$) at the pull-off was acquired as 12.6 $\frac{\mu m}{s}$. Using $V_0 = 6.3\ \mu m\ s^{-1}, n = 0.50$,[44] and *G* = 80 mN/m, G_0 of 33.1 mN/m is acquired, a value close to the one acquired from the loading phase data; however it should be noted that V_0 and *n* show high variation with changes in experimental conditions such as preparation conditions.

2.3.5 Force-Displacement Measurements under Water

A "jump-in" is a surface free energy induced mechanical instability transition that often occurs while conducting adhesion measurements, meaning two surfaces jump into each other, establishing a finite contact even at zero load.[45] Jump-in was observed between PDA nanomembranes and both PDMS and Ecoflex lenses in air. However, these artifacts were not observed in

aqueous environments.[46] Eqn. 2.39 could be fit to the loading phase of force-displacement curves for both PDMS and Ecoflex lenses underwater. However, the value of G was near zero throughout the loading phase for both PDMS and Ecoflex lenses (**Figure 2.10c**; **See Appendix**). Also the measurements against PDA nanomembranes with $h_{rms,PDA}$ greater than 20 nm largely abolish the adhesion (pull-off force) for measurements with both PDMS and Ecoflex lenses. For measurements in water, other studies show that the velocity dependent viscoelastic effect is very low for PDMS where the two order of magnitude of retraction velocity difference shows only about ~ 10 % difference in pull-off force;[44] a result consistent with the expectation that hydrophobic molecular chains at the interface will tend to collapse due to hydrophobic-hydrophobic interaction in water. It is likely that the observed hysteresis is due to the pressure dependent contact establishment under presence of water, which will be discussed in the later section (Section 2.3.7).

2.3.6 Effect of Roughness on Adhesion

From the pull-off forces from indentation measurements, plots of W_{UL} vs. RMS roughness ($h_{rms,PDA}$) of PDA nanomembranes and W_{UL} vs. RMS gradient ($h'_{rms,PDA}$) of PDA nanomembranes were constructed (**Figure 2.12**). **Figure 2.12a** shows the plot of W_{UL} vs. $h_{rms,PDA}$ in air. For PDA nanomembranes of $h_{rms,PDA}$ < 60 nm, W_{UL} from measurements with PDMS and Ecoflex lenses did not show the trend of W_{UL} value decreasing with increasing $h_{rms,PDA}$. For Ecoflex lenses, the same trend (W_{UL} not decreasing with increasing $h_{rms,PDA}$) held true throughout the $h_{rms,PDA}$ range explored (< 200 nm). For PDMS lenses, W_{UL} decreased with increasing $h_{rms,PDA}$ in the range of $h_{rms,PDA}$ > 60 nm. The observed behavior is in reasonable agreement with theoretical

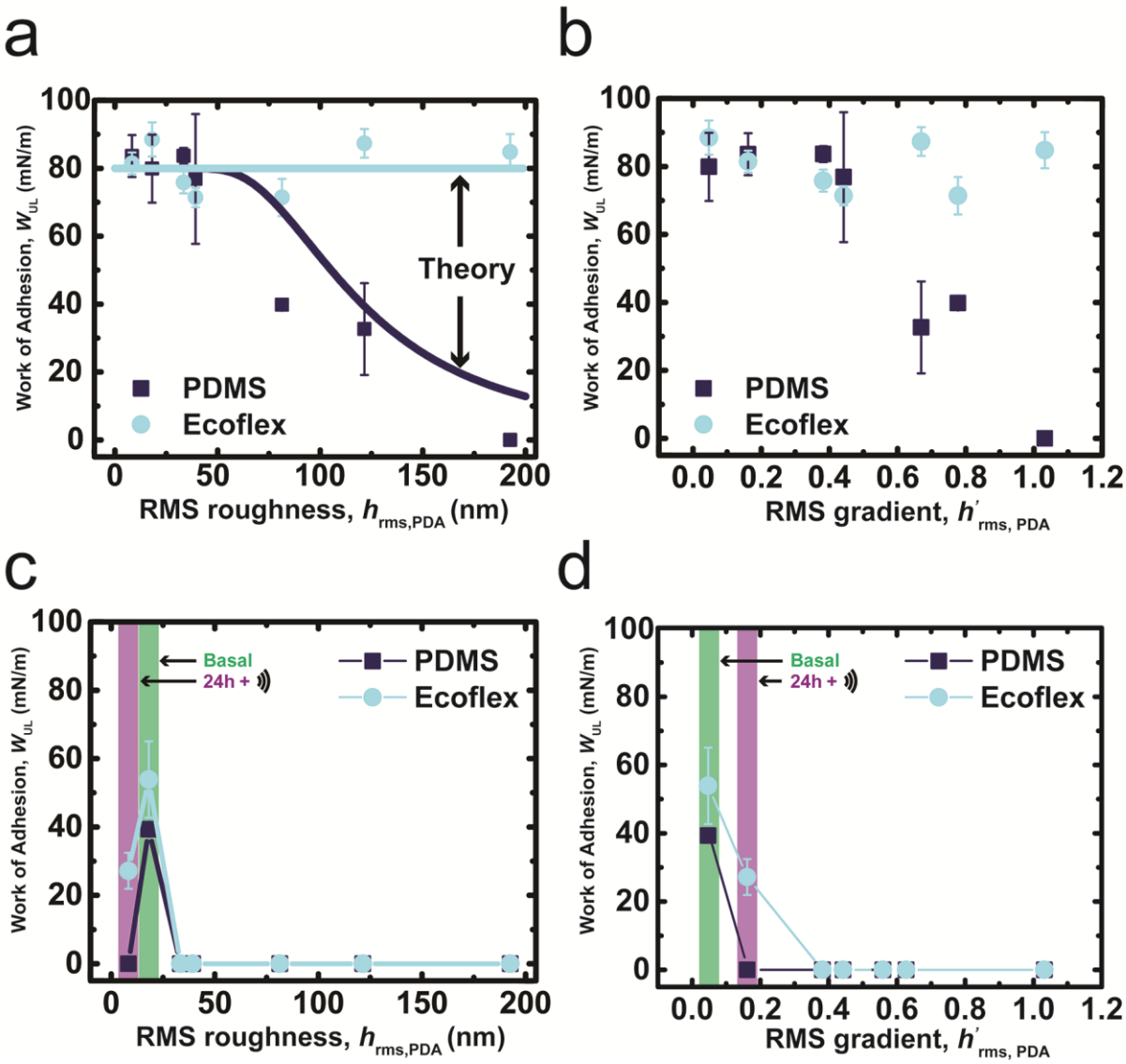

Figure 2.12: a) Plot of the effective work of adhesion vs. RMS roughness of PDA nanomembranes (W_{UL} vs $h_{rms,PDA}$) in air. b) Plot of the effective work of adhesion vs. RMS gradient of PDA nanomembranes (W_{UL} vs $h'_{rms,PDA}$) in air. c) Plot of the effective work of adhesion vs. RMS roughness of PDA nanomembranes underwater (W_{UL} vs $h_{rms,PDA}$). d) Plot of the effective work of adhesion vs. RMS gradient of PDA nanomembranes underwater (W_{UL} vs $h'_{rms,PDA}$). Highlighted regions contain points for basal PDA surfaces and apical PDA surfaces with 24 h deposition and subsequent sonication (c and d). Data plotted as mean ± s.d. for n = 3.

predictions based on Greenwood-William theory (**Figure 2.12a**) (**See Appendix**). The slight overestimation in W_{UL} is anticipated as the surface estimation through Gaussian distribution underestimates the effect of outliers (**See Appendix**).[47,48] Experimental data follows the key characteristic features expected from the theory: 1) there is an elasticity-dependent reduction in

the work of adhesion; 2) the work of adhesion is nearly constant for roughness values smaller than a certain threshold value ($h_{rms,PDA}$ = 60 nm for PDMS and $h_{rms,PDA}$ > 200 nm for Ecoflex), which is also modulus-dependent. W_{UL} can also be plotted against other roughness parameter, RMS gradient ($h'_{rms,PDA}$) (**Figure 2.12b**). W_{UL} and $h'_{rms,PDA}$ are inversely correlated with similar key characteristic behaviors observed in the plot of W_{UL} vs. $h_{rms,PDA}$. Namely, the value of W_{UL} between PDMS & PDA decreases with increasing $h'_{rms,PDA}$ for $h'_{rms,PDA}$ values beyond a threshold value. Also, the value of W_{UL} between Ecoflex & PDA is nearly constant for the range of $h'_{rms,PDA}$ range explored in this study.

Figure 2.12c and d show the plots of W_{UL} vs. $h_{rms,PDA}$ and W_{UL} vs. $h'_{rms,PDA}$ underwater. As noted previously, non-zero adhesion (pull-off force) was observed only for $h_{rms,PDA}$ < 20 nm for both PDMS and Ecoflex lenses, hinting that the effect of roughness on adhesion intensified in water (**Figure 2.12c**). Interestingly, values for W_{UL} for basal PDA surfaces ($h_{rms,PDA}$ = 18.1 nm) are larger than that of apical PDA surfaces with 24 h sonication ($h_{rms,PDA}$ = 8.3 nm) despite the former having a larger $h_{rms,PDA}$ than the latter (**Figure 2.12c**). For this situation, it could be instructive to examine another roughness related parameter; RMS gradient. Basal PDA surfaces exhibit a lower RMS gradient than the apical surface of PDA membranes that formed through 24 h deposition and sonication ($h'_{rms,PDA}$ = 0.047 vs. $h'_{rms,PDA}$ = 0.16). Assuming PDA surfaces all follow same distribution profile (i.e. Gaussian distribution), h_{rms} and h'_{rms} are proportionally correlated, which clearly is not the case between the two points here. The presence of outliers (spherical aggregates from the bulk-phase) could give rise to the present discrepancy. Per Persson's theory, the true contact between surfaces is influenced more by the smaller scale features in the surface, which is more representative by h'_{rms}.[3] As so, more focus is cast on the dependency on h'_{rms} in the following section.

2.3.7 Theoretical Analysis of Effect of Roughness in Water

No widely adapted satisfactory theory exists dedicated explicitly to analyze adhesion underwater. A thorough and exact computation of the interfacial interaction for elastic bodies in a fluid medium is a challenging problem; fluid-dynamics with consideration of possible pressure-dependent fluid viscosity effect and elastic confinement effect needs to be considered.[49-51] However, in analyzing rubber fluid squeeze-out macroscopic phenomenon, Persson showed that simplifications could be made. Assuming Newtonian fluid and the influence of the fluid-pressure on the solid-contact could be neglected, Persson analyzed the rubber fluid squeeze-out with the assumption that contact between rubber and the other solid could be approximated with Hertzian like deformation (no adhesion).[52] This is in-agreement with the current experimental results as the "jump-in", adhesive pressure driven snap of one solid to the other, was not observed during the loading phase underwater, the energy release rate was zero throughout the loading phase, and the in water recovered modulus agreed with the in air value; it could be posited that the presence of water blocks the long-range (relatively) adhesive interaction that causes spontaneous snap of elastomer to the other surface. For the following analysis, it is assumed that for the adhesion to be established underwater, surfaces first need to come into contact in the angstrom range opposed to the automatic snap of the surfaces in air or vacuum; support for the assertion could be found in the literature, where the dewetting transition between elastomers was only observed when surfaces were in ~ 400 angstrom proximity.[53]

For the present analysis, it is assumed that the contact is established during loading phase in a Hertzian manner. During unloading, only the portion of the surfaces established contact during loading phase participate in the adhesive interaction. Denoting the ratio between the actual contact area (a portion of the surface established contact) to nominal contact area as ($A/$

A_0), we will assume that the pull-off force will scale in a Greenwood-Williamson like manner such that $F_{\text{pull}} \propto (\frac{A}{A_0})^{\frac{3}{2}}$.[13] According to Persson's theory with Hertzian-like boundary condition, the ratio between the real contact area to a nominal contact area (A/A_0) is described by Eqn. 2.27:

$$\frac{A}{A_0} = \text{erf}\left(\frac{\sqrt{2}\sigma_0}{E^* h'_{rms}}\right) \qquad \text{Eqn 2.46}$$

where σ_0 is the applied pressure, E^*, combined elastic modulus between two bodies, and h'_{rms}, the RMS gradient. Pressure that the pull-off region (apex of the hemispherical probe) experiences during loading can be acquired as:[42]

$$\sigma_0 = \frac{1}{\pi}\left(\frac{6FE^{*2}}{R^2}\right)^{\frac{1}{3}} \qquad \text{Eqn 2.47}$$

where F will correspond to the 1 mN in the current situation, which is the maximal force during loading. Substituting Eqn. 2.47 to Eqn. 2.46, we acquire:

$$\frac{A}{A_0} = \text{erf}\left(\frac{\sqrt{2}\sqrt[3]{6}F^{\frac{1}{3}}}{\pi^{\frac{1}{3}}E^{*\frac{1}{3}}h'_{rms}R^{\frac{2}{3}}}\right) \qquad \text{Eqn. 2.48}$$

Eqn. 2.48 can be used to get the ratio of the portion of the nominal contact area that established contact during the loading phase. As $F_{pull} \propto (\frac{A}{A_0})^{\frac{3}{2}}$, W_{UL} (G) will also scale as $(\frac{A}{A_0})^{\frac{3}{2}}$. Since the viscoelastic dissipation is negligible in water, the thermodynamic work of adhesion calculated from the contact angle measurements data can be directly used to compare with the acquired W_{UL} experimental data such that the relation between G and h'_{rms} becomes:

$$G = G_{Thermo}\left[\text{erf}\left(\frac{\sqrt{2}\sqrt[3]{6}F^{\frac{1}{3}}}{\pi^{\frac{1}{3}}E^{*\frac{1}{3}}h'_{rms}R^{\frac{2}{3}}}\right)\right]^{\frac{3}{2}} \qquad \text{Eqn. 2.49}$$

Using $E^*_{PDMS} = 1.52\ MPa, E^*_{Ecoflex} = 85\ kPa, R = 3\ mm, and\ G_{Thermo} = 50\ mN/m$ in accordance with the current experimental condition, G vs h'_{rms} was plotted along with the experimental results (**Figure 2.13**). Despite considerable simplifications, a good agreement was found between the experiment and the theory, despite slight overestimation at the higher h'_{rms} range, which is cautiously accounted to the effect of outliers in surface topology. The present analysis could be used to explain hysteresis in underwater experiments as the amount of pressure during loading phase varies according to Hertzian like distribution along the contact radius, but this assertion warrants a further study.

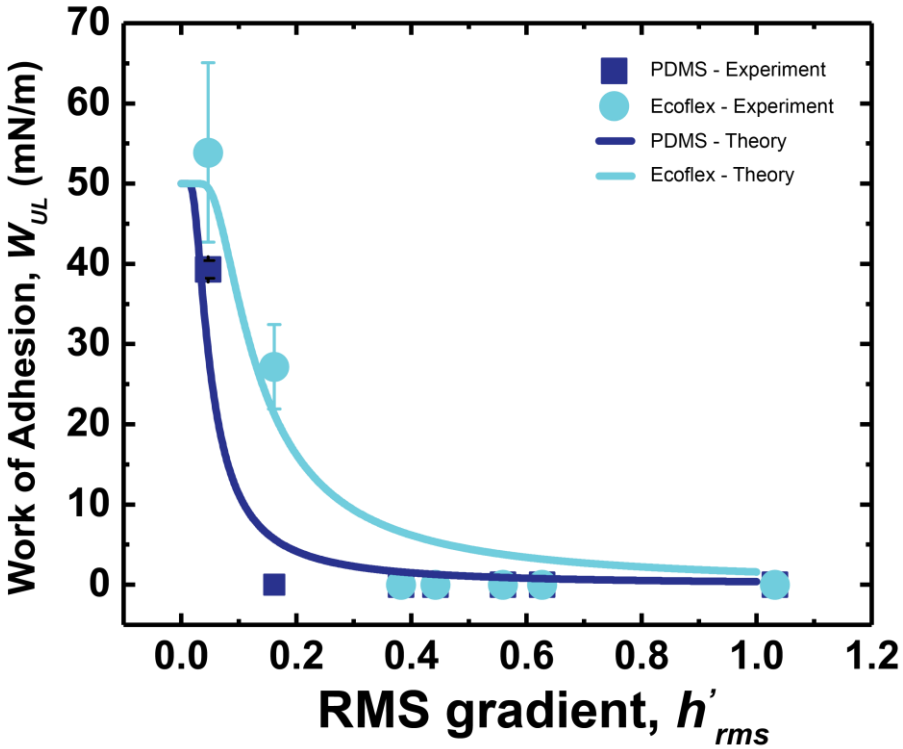

Figure 2.13: Plot of the work of adhesion during unloading vs RMS gradient of the surface underwater. Experimental data plotted as mean ± s.d. (n = 3).

The proposed physical model to explain texture-dependent adhesion in various environments is shown in **Figure 2.14**. In air, both Ecoflex (Low Elasticity) and PDMS (High Elasticity)

lenses conform well to smooth PDA surfaces (low $h_{rms,PDA}$). For rough PDA surfaces (high $h_{rms,PDA}$), Ecoflex lenses still conform well, attested by the negligible W_{UL} change with respect to change in $h_{rms,PDA}$. PDMS lenses conform poorly to PDA surfaces with high $h_{rms,PDA}$, translating to the lower work of adhesion. For the underwater case, the effect of roughness intensifies, with adhesion completely removed for PDA surfaces with $h_{rms,PDA}$ > 20 nm. The observed intensification showed a good agreement with the proposed model where the contact establishes underwater in a Hertzian like manner due to water phase blocking the long-range (relatively) adhesive interaction. The finding suggests that the suppression of adhesion underwater, often explained exclusively from a molecular level, might need to be revisited by carefully considering the morphology of the samples as the nanoscale texture completely abolished adhesion underwater. The analysis presented here could help understand the bulk adhesion of PDA in a more systematic manner.

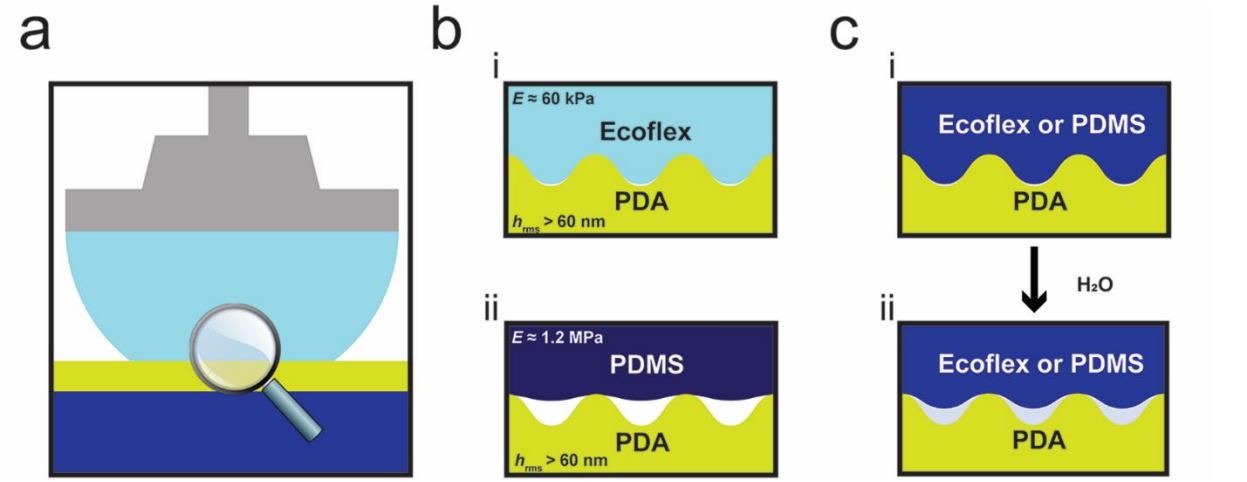

Figure 2.14: Schematic of contact between PDA nanomembranes on substrates interfacing with elastomeric spherical probes. a) The contact region between the lens and PDA substrates is magnified in subsequent panels. b-i) Ecoflex conforms well to interfaces composed of PDA nanomembranes with both $h_{rms,PDA}$ > 60 nm and $h_{rms,PDA}$ < 60 nm. b-ii). PDMS conforms poorly to PDA interfaces with $h_{rms,PDA}$ > 60 nm. c) Aqueous environments convolve the effect of surface roughness, translating to lower contact area as the deformation is Hertzian-like.

2.4 Conclusion

The role of texture in adhesive interaction of PDA nanomembranes was studied in various contexts. Micro-indentation tests elucidated the complex relationships between PDA texture, the elasticity of interacting bodies, and interfacial adhesion in both in air and underwater conditions. The nanometer-scale random roughness inevitably introduced to PDA nanomembranes during synthesis can significantly alter the adhesive behavior of PDA nanomembranes, and the fact suggests that the adhesion of PDA nanomembranes can be tuned through morphology control. Our findings suggest that the texture dependent adhesion could explain differential adhesion of PDA to many classes of materials. This study also highlights the importance of designing interfaces with low RMS gradients to ensure underwater adhesion and proposes a model capable of the analysis of the current model situation. This trend, observed in the context of PDA nanomembranes, could be extended to other types of materials as well. Generalizable trends can inform the design of PDA-based adhesives or other catechol-bearing functional materials that are designed to operate in aqueous conditions.

2.5 References

1 Cho, J. H. *et al.* Ultrasmooth Polydopamine Modified Surfaces for Block Copolymer Nanopatterning on Flexible Substrates. *Acs Appl Mater Inter* **8**, 7456-7463, doi:10.1021/acsami.6b00626 (2016).

2 Klosterman, L., Riley, J. K. & Bettinger, C. J. Control of Heterogeneous Nucleation and Growth Kinetics of Dopamine-Melanin by Altering Substrate Chemistry. *Langmuir* **31**, 3451-3458, doi:10.1021/acs.langmuir.5b00105 (2015).

3 Persson, B. N. J. Adhesion between an elastic body and a randomly rough hard surface. *Eur Phys J E* **8**, 385-401, doi:10.1140/epje/i2002-10025-1 (2002).

4 Klosterman, L., Ahmad, Z., Viswanathan, V. & Bettinger, C. J. Synthesis and Measurement of Cohesive Mechanics in Polydopamine Nanomembranes. *Adv Mater Interfaces* **4**, doi:ARTN 1700041

10.1002/admi.201700041 (2017).

5 Erath, J., Schmidt, S. & Fery, A. Characterization of adhesion phenomena and contact of surfaces by soft colloidal probe AFM. *Soft Matter* **6**, 1432-1437, doi:10.1039/b923540j (2010).

6 Shull, K. R. Contact mechanics and the adhesion of soft solids. *Mat Sci Eng R* **36**, 1-45, doi:Pii S0927-796x(01)00039-0

Doi 10.1016/S0927-796x(01)00039-0 (2002).

7 Johnson, K. L. & Johnson, K. L. *Contact mechanics*. (Cambridge university press, 1987).

8 Yang, F. *Self-polymerized Dopamine Thin Film as Bioadhesive*, UWSpace, (2012).

9 Fuller, K. N. G. & Tabor, D. The Effect of Surface Roughness on the Adhesion of Elastic Solids. *Proceedings of the Royal Society of London. A. Mathematical and Physical Sciences* **345**, 327 (1975).

10 Persson, B. N. J., Albohr, O., Tartaglino, U., Volokitin, A. I. & Tosatti, E. On the nature of surface roughness with application to contact mechanics, sealing, rubber friction and adhesion. *J Phys-Condens Mat* **17**, R1-R62, doi:10.1088/0953-8984/17/1/R01 (2005).

11 Persson, B. On the fractal dimension of rough surfaces. *Tribology letters* **54**, 99-106 (2014).

12 Carbone, G., Lorenz, B., Persson, B. N. J. & Wohlers, A. Contact mechanics and rubber friction for randomly rough surfaces with anisotropic statistical properties. *The European Physical Journal E* **29**, 275-284, doi:10.1140/epje/i2009-10484-8 (2009).

13 Greenwood, J. & Williamson, J. P. Contact of nominally flat surfaces. *Proc. R. Soc. Lond. A* **295**, 300-319 (1966).

14 Lorenz, B. *Contact mechanics and friction of elastic solids on hard and rough substrates*. Vol. 37 (Forschungszentrum Jülich, 2012).

15 Fuller, K. & Tabor, D. The effect of surface roughness on the adhesion of elastic solids. *Proc. R. Soc. Lond. A* **345**, 327-342 (1975).

16 Greenwood, J. A. Reflections on and Extensions of the Fuller and Tabor Theory of Rough Surface Adhesion. *Tribology Letters* **65**, 159, doi:10.1007/s11249-017-0938-1 (2017).

17 Nayak, P. R. Random process model of rough surfaces. *Journal of Lubrication Technology* **93**, 398-407 (1971).

18 Tomanik, E., Chacon, H. & Teixeira, G. in *Tribology Series* Vol. 41 (eds D. Dowson, M. Priest, G. Dalmaz, & A. A. Lubrecht) 205-215 (Elsevier, 2003).

19 Xu, Y., Jackson, R. L. & Marghitu, D. B. Statistical model of nearly complete elastic rough surface contact. *International Journal of Solids and Structures* **51**, 1075-1088, doi:https://doi.org/10.1016/j.ijsolstr.2013.12.005 (2014).

20 McCool, J. I. Relating Profile Instrument Measurements to the Functional Performance of Rough Surfaces. *Journal of Tribology* **109**, 264-270, doi:10.1115/1.3261349 (1987).

21 Persson, B. N. J. Theory of rubber friction and contact mechanics. *J Chem Phys* **115**, 3840-3861, doi:Doi 10.1063/1.1388626 (2001).

22 Yastrebov, V. A., Anciaux, G. & Molinari, J.-F. From infinitesimal to full contact between rough surfaces: evolution of the contact area. *International Journal of Solids and Structures* **52**, 83-102 (2015).

23 Klosterman, L., Ahmad, Z., Viswanathan, V. & Bettinger, C. J. Synthesis and Measurement of Cohesive Mechanics in Polydopamine Nanomembranes. *Advanced Materials Interfaces* **4**, 1700041-n/a, doi:ARTN 1700041

10.1002/admi.201700041 (2017).

24 Jiang, J. H., Zhu, L. P., Zhu, L. J., Zhu, B. K. & Xu, Y. Y. Surface Characteristics of a Self-Polymerized Dopamine Coating Deposited on Hydrophobic Polymer Films. *Langmuir* **27**, 14180-14187, doi:10.1021/la202877k (2011).

25 Tabor, D. Surface Forces and Surface Interactions. *J Colloid Interf Sci* **58**, 2-13, doi:Doi 10.1016/0021-9797(77)90366-6 (1977).

26 Crosby, A. J. & Shull, K. R. Adhesive failure analysis of pressure-sensitive adhesives. *J Polym Sci Pol Phys* **37**, 3455-3472, doi:Doi 10.1002/(Sici)1099-0488(19991215)37:24<3455::Aid-Polb7>3.3.Co;2-V (1999).

27 Johnson, K. L., Kendall, K. & Roberts, A. D. Surface Energy and Contact of Elastic Solids. *Proc R Soc Lon Ser-A* **324**, 301-&, doi:DOI 10.1098/rspa.1971.0141 (1971).

28 Maugis, D. & Barquins, M. Fracture Mechanics and Adherence of Viscoelastic Bodies. *J Phys D Appl Phys* **11**, 1989-&, doi:Doi 10.1088/0022-3727/11/14/011 (1978).

29 Vaenkatesan, V., Li, Z. L., Vellinga, W. P. & de Jeu, W. H. Adhesion and friction behaviours of polydimethylsiloxane - A fresh perspective on JKR measurements. *Polymer* **47**, 8317-8325, doi:10.1016/j.polymer.2006.09.037 (2006).

30 Waters, J. F. & Guduru, P. R. Mode-mixity-dependent adhesive contact of a sphere on a plane surface. *P Roy Soc a-Math Phy* **466**, 1303-1325, doi:10.1098/rspa.2009.0461 (2010).

31 Galliano, A., Bistac, S. & Schultz, J. Adhesion and friction of PDMS networks: molecular weight effects. *J Colloid Interf Sci* **265**, 372-379, doi:10.1016/S0021-9797(03)00458-2 (2003).

32 Ghatak, A., Vorvolakos, K., She, H. Q., Malotky, D. L. & Chaudhury, M. K. Interfacial rate processes in adhesion and friction. *J Phys Chem B* **104**, 4018-4030, doi:DOI 10.1021/jp9942973 (2000).

33 Fuller, K. & Tabor, D. in *Proceedings of the Royal Society of London A: Mathematical, Physical and Engineering Sciences.* 327-342 (The Royal Society).

34 Gent, A. N. & Schultz, J. Effect of Wetting Liquids on the Strength of Adhesion of Viscoelastic Material. *The Journal of Adhesion* **3**, 281-294, doi:10.1080/00218467208072199 (1972).

35 Williams, M. L., Landel, R. F. & Ferry, J. D. The Temperature Dependence of Relaxation Mechanisms in Amorphous Polymers and Other Glass-forming Liquids. *Journal of the American Chemical Society* **77**, 3701-3707, doi:10.1021/ja01619a008 (1955).

36 Waters, J. F. & Guduru, P. R. Mode-mixity-dependent adhesive contact of a sphere on a plane surface. *Proceedings of the Royal Society A: Mathematical, Physical and Engineering Science*, doi:10.1098/rspa.2009.0461 (2009).

37 Muller, V. M. On the theory of pull-off of a viscoelastic sphere from a flat surface. *Journal of Adhesion Science and Technology* **13**, 999-1016, doi:10.1163/156856199X00479 (1999).

38 Maugis, D. & Barquins, M. Fracture mechanics and the adherence of viscoelastic bodies. *Journal of Physics D: Applied Physics* **11**, 1989 (1978).

39 Barthel, E. & Haiat, G. Approximate Model for the Adhesive Contact of Viscoelastic Spheres. *Langmuir* **18**, 9362-9370, doi:10.1021/la025959+ (2002).

40 Barthel, E. & Roux, S. Velocity-dependent adherence: an analytical approach for the JKR and DMT models. *Langmuir* **16**, 8134-8138 (2000).

41 Sun, Y. & Walker, G. C. Viscoelastic response of poly (dimethylsiloxane) in the adhesive interaction with AFM tips. *Langmuir* **21**, 8694-8702 (2005).

42 Shull, K. R. Contact mechanics and the adhesion of soft solids. *Materials Science and Engineering: R: Reports* **36**, 1-45 (2002).

43 Lorenz, B. *et al.* Adhesion: role of bulk viscoelasticity and surface roughness. *Journal of Physics: Condensed Matter* **25**, 225004 (2013).

44 Tiwari, A. *et al.* The effect of surface roughness and viscoelasticity on rubber adhesion. *Soft matter* **13**, 3602-3621 (2017).

45 Silberzan, P., Perutz, S., Kramer, E. J. & Chaudhury, M. K. Study of the Self-Adhesion Hysteresis of a Siloxane Elastomer Using the Jkr Method. *Langmuir* **10**, 2466-2470, doi:DOI 10.1021/la00019a073 (1994).

46 Zhang, W. *et al.* Surface and Tribological Behaviors of the Bioinspired Polydopamine Thin Films under Dry and Wet Conditions. *Biomacromolecules* **14**, 394-405, doi:10.1021/bm3015768 (2013).

47 Persson, B. N. J. & Tosatti, E. The effect of surface roughness on the adhesion of elastic solids. *J Chem Phys* **115**, 5597-5610, doi:Doi 10.1063/1.1398300 (2001).

48 Rabinovich, Y. I., Adler, J. J., Ata, A., Singh, R. K. & Moudgil, B. M. Adhesion between nanoscale rough surfaces - I. Role of asperity geometry. *J Colloid Interf Sci* **232**, 10-16, doi:DOI 10.1006/jcis.2000.7167 (2000).

49 Villey, R. *et al.* Effect of Surface Elasticity on the Rheology of Nanometric Liquids. *Physical Review Letters* **111**, 215701, doi:10.1103/PhysRevLett.111.215701 (2013).

50 Hu, Y.-Z. & Zhu, D. A Full Numerical Solution to the Mixed Lubrication in Point Contacts. *Journal of Tribology* **122**, 1-9, doi:10.1115/1.555322 (1999).

51 Lorenz, B. & Persson, B. N. J. Leak rate of seals: Comparison of theory with experiment. *EPL (Europhysics Letters)* **86**, 44006 (2009).

52 Persson, B. N. J. Fluid dynamics at the interface between contacting elastic solids with randomly rough surfaces. *Journal of Physics: Condensed Matter* **22**, 265004 (2010).

53 Roberts, A. & Tabor, D. The extrusion of liquids between highly elastic solids. *Proc. R. Soc. Lond. A* **325**, 323-345 (1971).

Chapter 3

Surface Wrinkle Dependent Adhesion in PDA

(Disclaimer: The following chapter is part of a collaboration for the resultant publication of which, myself is a co-first author. My co-author collected data. All the figures, analysis, and writing presented in this chapter are my own, unless otherwise noted.)

3.1 Introduction

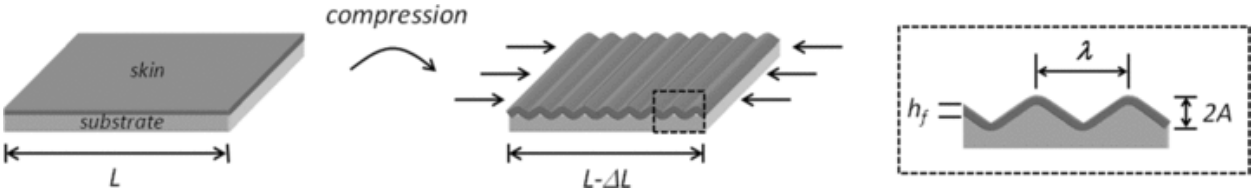

Figure 3.1: Formation of the surface wrinkles through thin-film buckling. Reproduced from [17]

In nature, as elaborately demonstrated with the example of gecko setae microstructures, surface patterns are used to dynamically control the adhesion of interfaces, such that reversible adhesion is maintained through multiple attachment and detachment cycles.[1-5] Inspired by the remarkable degree of effectiveness of natural systems, there have been significant efforts to reproduce such functionality by introducing surface patterns to synthetic systems.[6-13] While the most dominant surface pattern approach in synthetic reversible adhesives is the introduction of fibrillar structures, use of surface wrinkles has been proposed as an alternative surface pattern strategy with its primary advantage being a simpler fabrication step without the need of complicated lithographic steps, and the robust and facile real-time tunability of adhesion.[14,15] Surface wrinkles can be conveniently introduced to elastomeric substrates via compressive stress induced thin-film buckling (**Figure 3.1**).[16-18] Adhering a thin rigid skin to an uniaxially pre-strained elastomeric substrate with the subsequent release of pre-strain results in a buckling mechanical instability that introduces periodically ordered surface wrinkles on the substrate.[17,19] As PDA is a rigid nanomembrane with modulus in the gigapascal range,[19-21] PDA is ideally suited

as a component of the smart wrinkle system, and the incorporation of PDA into smart wrinkle systems could be an additional strategy to control the adhesion of PDA interface. Chapter 3 discusses the PDA incorporated wrinkle system, the adhesion of which was dynamically switched on and off with applied mechanical strain. A new kind of theoretical framework to analyze the effect of wrinkle geometry to adhesion based on the elliptical JKR contact model is presented, which could be conveniently used to predict the macro-adhesive property of surface wrinkle systems, not limited to the PDA system.

3.2 Methods

3.2.1 Materials

Dopamine hydrochloride (98%) was purchased from Sigma-Aldrich (St. Louis, MO USA) and used as received. Tris(hydroxymethyl) aminomethane (Tris) was purchased from Fisher Scientific (Hampton, NH USA) and used as received. Water was purified (18.2 MΩ-cm) using Direct-Q 3 UV-R system (Millipore). Silicon wafers with 1 μm thermal oxide were purchased from Silicon Quest International (San Jose, CA USA; 4" diameter, phosphorus doped). Sylgard 184 (Polydimethylsiloxane) was purchased from Dow Corning (Midland, MI USA). Borosilicate glass hemispherical probes were purchased from Edmund Optics (Barrington, NJ USA; 6mm diameter). Epoxy was purchased from Loctite (Düsseldorf, GER; Aqua Marine Epoxy). Gold targets (>99.99%) and chrome targets (chrome-plated tungsten rods; 99.9%) were purchased from Kurt J. Lesker (Jefferson Hills, PA USA).

3.2.2 Freestanding PDA Nanomembrane Preparation

Silicon wafers with 1 μm thick thermal oxide were cleaned by sonication in acetone and isopropyl alcohol followed by rinsing in ddH_2O. Substrates were further cleaned by UV-ozone treatment (5 min at 30 mW-cm^{-2}; Jelight, Irvine, CA USA). PDA films were prepared by

incubating pre-cleaned silicon substrates in 2 mg/ml dopamine hydrochloride in 100 ml of 10 mM Tris buffer in ambient air and under rotation (65 rpm) for 24 h. Afterwards, samples were placed in 50 mM Tris HCl solution (pH = 8.5) and was subjected to sonication for 2 h. Samples were then placed in 200 mM NaCl + 50 mM Tris buffer solution for > 6 h for delamination of the film. Delaminated nanomembranes were transferred to ddH_20 prior to the PDA/PDMS substrate fabrication.

3.2.3 Fabrication of the PDA/PDMS Substrates

Polydimethylsiloxane (PDMS) blend was prepared by mixing 10 parts base to 1 part curing agent, went through degassing in mild vacuum for ~ 5 min three times, and cured at 80 °C for 18 h. Rectangular PDMS coupons (Dimensions ~ cm) went through sol-phase extraction procedure. PDMS coupons were incubated in hexane and acetone for 3 h three times, were washed with ethanol and ddH_2O, and dried under an N_2 stream. PDMS coupons were mounted onto a custom-built strain device under designated uniaxial strains and subjected to oxygen plasma treatments (260 mTorr, 18W RF power, ambient O_2, 30 sec; Harrick Plasma, Ithaca, NY USA). Afterwards, while mounted on the strain device, PDMS coupons were submerged in ddH_2O bath. Free-standing PDA nanomembranes were positioned at the water-air interface above the PDMS coupons and the water level was lowered until the PDA nanomembranes laminated onto the PDMS coupons. PDA/PDMS structures were dried under an N_2 steam, and the strain was released. All samples were used within 20 h of fabrication.

3.2.4 Fabrication of the Hemispherical Indentation Probe

Borosilicate glass hemispheres, mounted onto screws with epoxy, were rinsed with isopropyl alcohol and ddH_2O, and dried under an N_2 stream. 5 nm Cr and 50 nm Au were thermally evaporated onto the probes (0.2 Å s^{-1}, NexDep, Angstrom Engineering, Kitchener, ON Canada).

3.2.5 Morphological Characterization of the PDA/PDMS Substrates

Film roughness were measured using atomic force microscopy (NTegra AFM, NT-MDT, Tempe, AZ USA) in tapping mode. Scans were 30 μm x 30 μm at 0.5 Hz using tips with a reported radius of < 10 nm (Budget Sensors, Sofia, Bulgaria; k = 40 N/m). Topographic data was analyzed using Gwyddion AFM software (http://gwyddion.net/) to measure the geometry of the wrinkles (wavelength & amplitude). 2D profiles of surfaces were extracted. Wavelength was measured by measuring the crest to trough horizontal distance and multiplying the value by two. Amplitude was measured by measuring the vertical distance from crest to trough and dividing the value by two. The measured values of the geometry of the wrinkles are reported as mean ± s.d. unless otherwise stated (n = 10).

3.2.6 Micro-indentation Measurements

The indentation probe was mounted on a 25g load cell (GSO-25, Transducer Techniques, Temecula, CA USA), attached to a stack of a vertical motorized stage (MFA-CC, Newport Corporation, Irving, CA USA) for vertical motion and a manual tilting stages (Newport GON40-L) for alignment, motion of which was controlled by Newport ESP 301 motion stage. Custom written LabView software was used for control. All measurements were performed at room temperature and in air. Before each measurement, indentation probes were rinsed in ethanol, dried under an N_2 stream. The indentation probe was positioned over a PDA/PDMS substrates at arbitrary heights and approached at a vertical speed of 0.5 μm/s until reaching a preload of 1 mN, allowed to dwell for 120 sec, and then retracted at 0.5 μm/s until the detachment occurred. Force-distance curves were generated during the indentation. For the indentation measurements in which the PDA/PDMS went through cyclic mechanical strains, PDA/PDMS substrates were mounted onto the custom-built strain device, and the mechanical strain of either 40 % or 0 % was applied.

A metallic cube was placed below the PDA/PDMS substrates to prevent the possible bending of the PDA/PDMS structure during the indentation measurements. Afterwards, the same procedure as described above was repeated, while either 40 % or 0% strain was applied, to generate force-displacement curves. The measured values from the indentation measurements are reported as mean ± s.d. unless otherwise stated ($n \geq 4$).

3.3 Results and Discussion

3.3.1 Control of the Surface Wrinkle Geometry of PDA/PDMS Substrates through Variation of the Applied Pre-strain

Free-standing PDA nanomembranes, prepared by incubating PDA films grown on SiO_2 substrates in a mildly basic solution[19] were laminated onto the O_2 plasma treated PDMS that were pre-strained at pre-strains ranging from $\varepsilon_0 = 0$ % to $\varepsilon_0 = 50$ % via aqueous phase transfer-printing. Upon release of the pre-strain, PDA/PDMS structures buckled to create sinusoidal wrinkles (**Figure 3.2a**). In addition to the sinusoidal wrinkles, occasional ridges or cracks were observed on the PDA surface, the cause of which could be attributed to the imperfect flattening of the PDA membranes during transfer-printing process or the residual stress at the interface caused by the volume-change associated with the O_2 plasma introduced silica layer on PDMS (**Figure 3.2b**).[22] Depending on the pre-strain applied, PDA/PDMS structures with varying wrinkle geometries (amplitude A and wavelength λ) were obtained (**Figure 3.2c and d; See Appendix**).

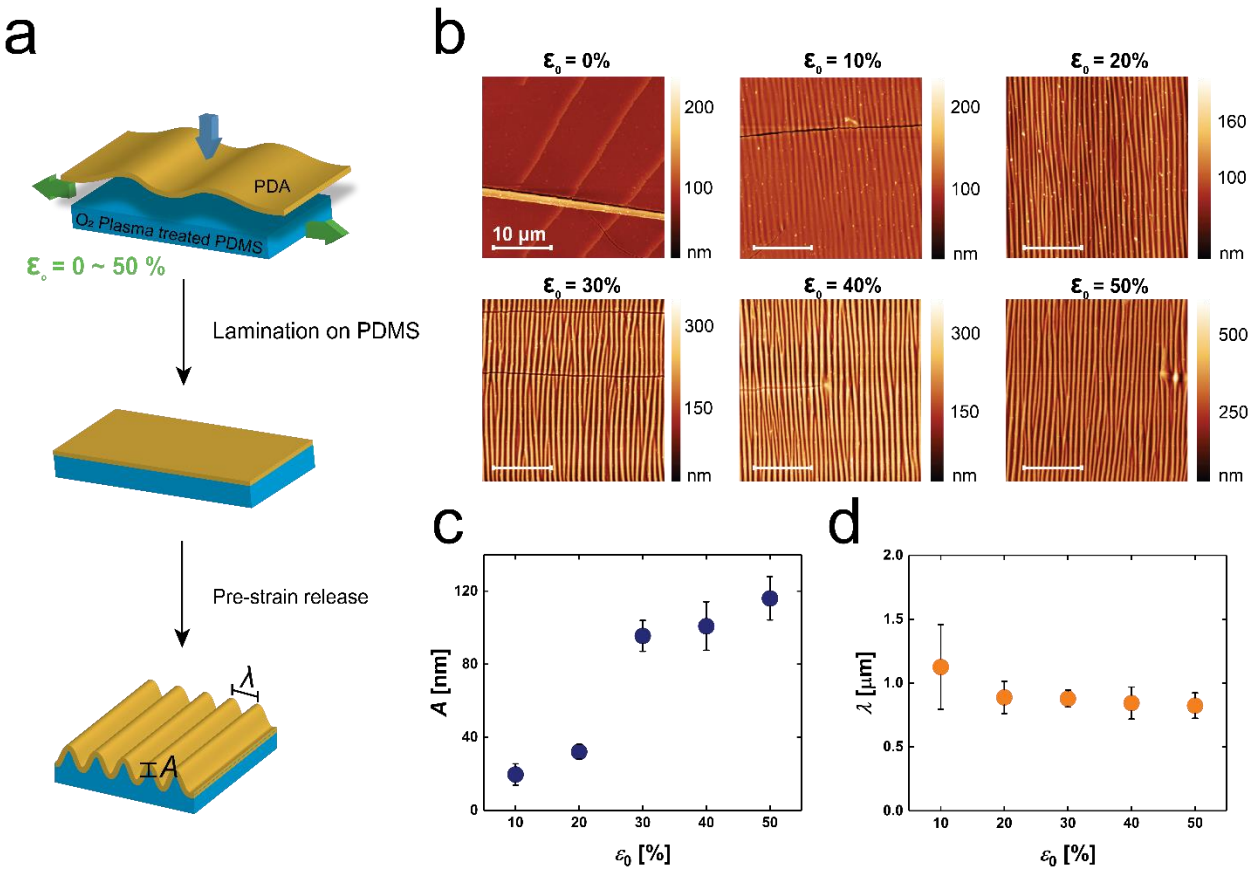

Figure 3.2 a) Schematic of the wrinkled PDA/PDMS substrate fabrication. b) AFM scans of a PDA/PDMS structure created with varying pre-strains (ε_0). All AFM images are 30 x 30 μm^2. c) Plot of the amplitude (A) vs pre-strain (ε_0). d) Plot of the wavelength (λ) vs pre-strain (ε_0).

3.3.2 Dependence of Adhesion on Wrinkle Geometry and the Reversible Control of Adhesion through Mechanical Strain

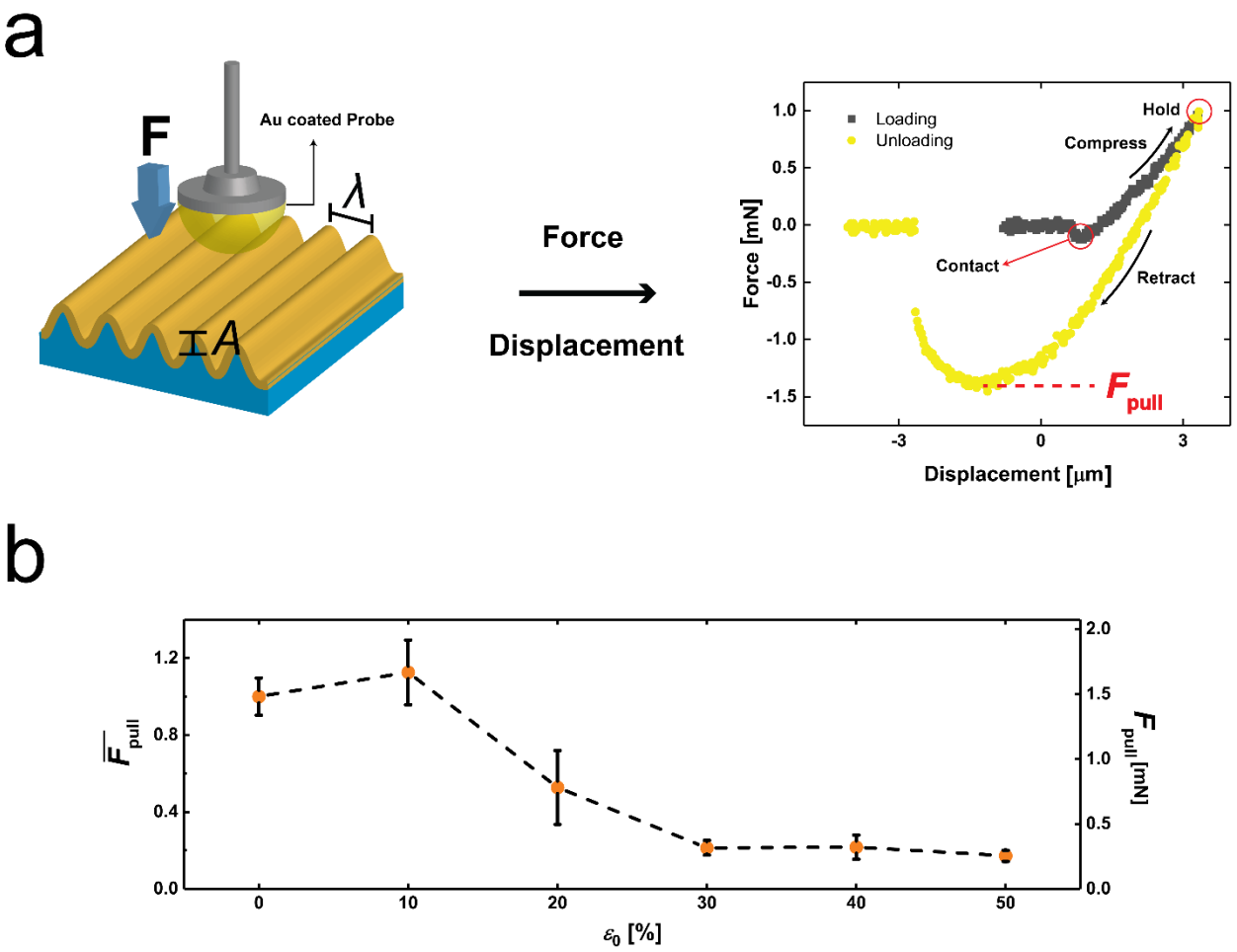

Figure 3.3: a) Force-displacement measurement schematic and the exemplary force-displacement curve produced from the measurement. Note that the origin of displacement is arbitrary as the indentation measurements start from the arbitrary probe position atop the samples. b) Plot of the normalized pull-off force ($\overline{F_{pull}}$) and pull-off force (F_{pull}) vs pre-strain (ε_0).

Interfacial adhesion of PDA/PDMS structures with different wrinkle geometries were measured through micro-indentation measurements in air. Borosilicate hemisphere, coated with gold, was indented against the wrinkled PDA/PDMS substrates created with different pre-strains, and the force-displacement curves were generated (**Figure 3.3a; See Appendix**). From the force-displacement curve, the maximum tensile force was recorded to be a pull-off force (F_{pull}) (**Figure 3.3a**). A "jump-in", a surface-force induced mechanical instability, was only observed for the

samples with $\varepsilon_0 \leq 20$ % (**See Appendix**). Absence of jump-in for the samples with $\varepsilon_0 > 20$ % is probably due to the fact that more profound wrinkle geometries for those samples make the transition to the in-contact state at zero-load energetically unfavorable. For the case of $\varepsilon_0 = 0$ % sample, the flat geometry of the surface permits the fitting of the loading portion of the force-displacement data to the Johnson-Kendall-Roberts (JKR) theory. The expected thickness of the combined thickness of PDA and silica layer is less than 100 nm.[23,24] As the thickness of the rigid layer in the PDA/PDMS substrates is < 100 nm, and the probe dimension is in the millimeter range (radius of the probe = 3 mm), the effective modulus of the current composite structure will be close to that of the pure PDMS with difference being the interfacial chemistry substituted with that of PDA.[25] Following the procedure detailed in section 2.3.2 ~ 2.3.3, the work of adhesion (W_{ad}; energy release rate (G)) and the combined elastic modulus (E^*) between the gold probe and the PDA/PDMS substrates were found to be 25.5 ± 8.6 mN/m and 2.6 ± 0.45 Mpa (n = 4; $R^2 > 0.994$), respectively. The recovered E^* corresponds to the PDMS modulus of about 2.0 ± 0.34 MPa ($E_{\text{PDMS}} \approx \frac{E^*}{1-\nu_1^2}; \nu_1 = 0.5$ for PDMS), which is in agreement with the Sylgard 184 (PDMS) modulus reported in the literature for the similar synthesis condition as herein.[26] Recovered G could have been affected by the surface heterogeneities as detailed in Chapter 2. The measured F_{pull} value for the case of $\varepsilon_0 = 0$ % are 1.48 ± 0.14 mN, reaching an equivalent work of adhesion (W_{ad}) of 112 mN/m ($W_{\text{ad}} = F_{\text{pull}}/1.5\pi R$;[27] R = radius of the probe (3 mm)). There is a significant adhesion hysteresis (25 mN/m vs. 112 mN/m). Tracking down the origin of the adhesion hysteresis is a tricky question. While the interfacial chemistry reconstruction, which for the case of interaction between Au and PDA might involve charge-transfer mechanism,[28] could be responsible, the dissipative mechanism at the interface, the origin of which is from the various molecular mechanics, play a role as well. For the current system, despite the rigid nature of the PDA and

silica layer, the thickness is in the nanometer range and the previous studies inform that plastic deformation is the unlikely source of adhesion hysteresis in that case.[29,30] The proposed likely mechanism for the adhesion hysteresis between the elastomer and solid surface is the polymeric chain pull-out or stretching from the interface of the elastomer network.[31] Even though our composite is covered with the rigid layer, diffusion of the low molar siloxane phase to the interface will result in the recovery of polymeric chains participating in the dissipative mechanism at the interface; to prevent the diffusive contamination, PDMS in the current composite structure went through sol-phase extraction to remove the low-molecular oligomers within the PDMS network. Also before measurements, the water contact angle on the composite structures was checked to be < 50° (data not shown), which confirms that the interface is predominantly PDA. The process provides a remedy to the problem, but the quantification of the degree of the remedy that the sol-extraction process provides to remove the dissipative dissipation, warrants a further study than presented here. Yet, it could be posit that the degree of dissipative mechanism in the composite interface lies somewhere between zero-interfacial dissipation to that of the untreated pure PDMS. Then the range of the dissipative mechanism accounted thermodynamic work of adhesion between the Au and PDA interface solely from the surface chemistry would lie between 112 mN/m to 42.6 mN/m (derived according to the process detailed in section 2.3.4). While the true value is expected to be closer to the upper-bound (112 mN/m), a definitive conclusion can't be drawn with the current evidences. However, even taking a lower-bound as the true-value informs that PDA interface could have gone through an interfacial chemistry reconstruction.

F_{pull} of each sample was normalized with the average F_{pull} value of $\varepsilon_0 = 0$ % samples to get the normalized pull-off forces ($\overline{F_{\text{pull}}}$). **Figure 3.3b** shows the plot of $\overline{F_{\text{pull}}}$ and F_{pull} versus ε_0 used to create the samples. $\overline{F_{\text{pull}}}$ increase initially with increasing ε_0, but subsequently decreases

as ε_0 further increases; adhesion of the PDA/PDMS substrate is the strong function of its wrinkle geometry. Initial increase in $\overline{F_{\text{pull}}}$ is likely attributed to the contact-splitting, and the subsequent decrease is likely attributed to decrease in the contact area as the amplitude increases, which decreases the radius of the wrinkles at the apex. A PDA/PDMS sample created with the pre-strain (ε_0) of 40 % went through a cyclic strain between $\varepsilon = 0$ % and $\varepsilon = 40$ % (**Figure 3.4a**), and the adhesion (F_{pull}) was measured at each strain condition. The reversible controllability of adhesion was maintained up-to five cycles, which is likely to expand to more cycles even though was not tested. **Figure 3.4c** shows the exemplary force-displacement curves at each strain. For the measurements at $\varepsilon = 40$ %, despite the flat geometry of the specimen, the loading portion of the force-displacement curve deviates from the $\varepsilon_0 = 0$ % curve, an artifact could be coming from the stretched state of the sample. Nonetheless, adhesion of the PDA/PDMS substrate was reversibly turned on and off through the mechanical strain applied, demonstrating the PDA/PDMS system's effectiveness in a fast actuation of adhesion tuning (**Figure 3.4**).

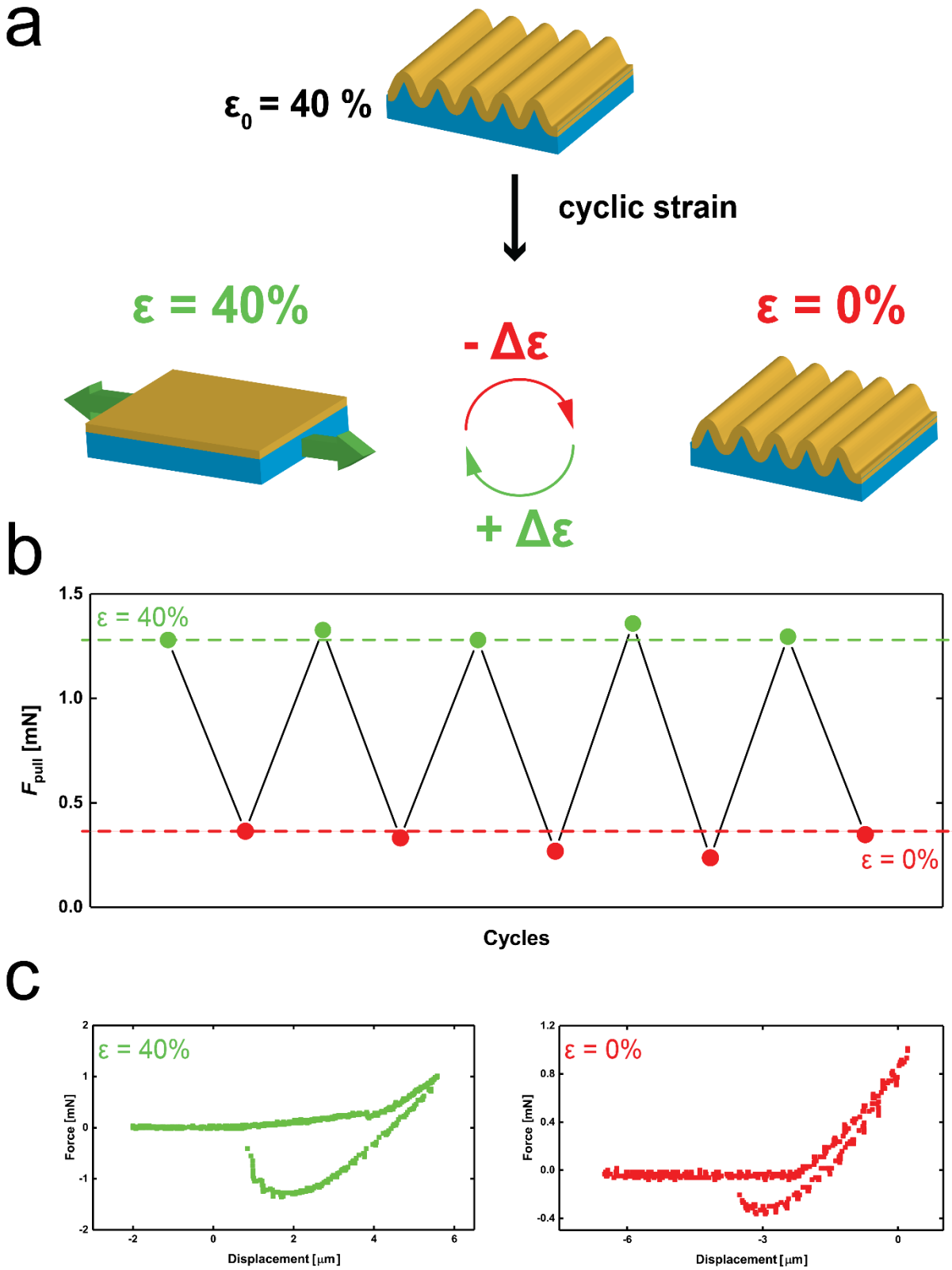

Figure 3.4: a) Schematic of the cyclic strain application. b) Pull-off forces were reversibly varied through several cycles. c) Exemplary force-displacement curves at each strain. Left) ε = 40 %. Right) ε = 0 %.

3.3.3 Theoretical Analysis of the Effect of the Wrinkle Geometry on Adhesion

A framework that could predict the adhesion (pull-off force) of the PDA/PDMS substrate as a function of the wrinkle geometry would be a convenient tool, and the analysis could be extended to other materials with the wrinkle geometry as well. The exact computation of the whole deformation of the wavy (wrinkled) surface in contact with the spherical probe is a non-trivial task which involves a heavy numerical computation.[32-34] If one's primary interest is in predicting pull-off force, the most important figure of merit in measuring material's adhesion, of the wrinkled surface, an approximate approach based on treating each wrinkle to act independently with the probe at the time of pull-off has shown to be in a reasonable agreement with the experimental results with a much facile computation scheme and tractable parametric form.[14,35,36] However, in the literature, an attempt in providing a facile scheme to predict the wrinkle geometry adhesion didn't go beyond providing a scaling relationship between the pull-off force and the wrinkle geometry. This section presents an approach that expands on that line of effort to predict the pull-off force as a function of the wrinkle geometry with a definite value.

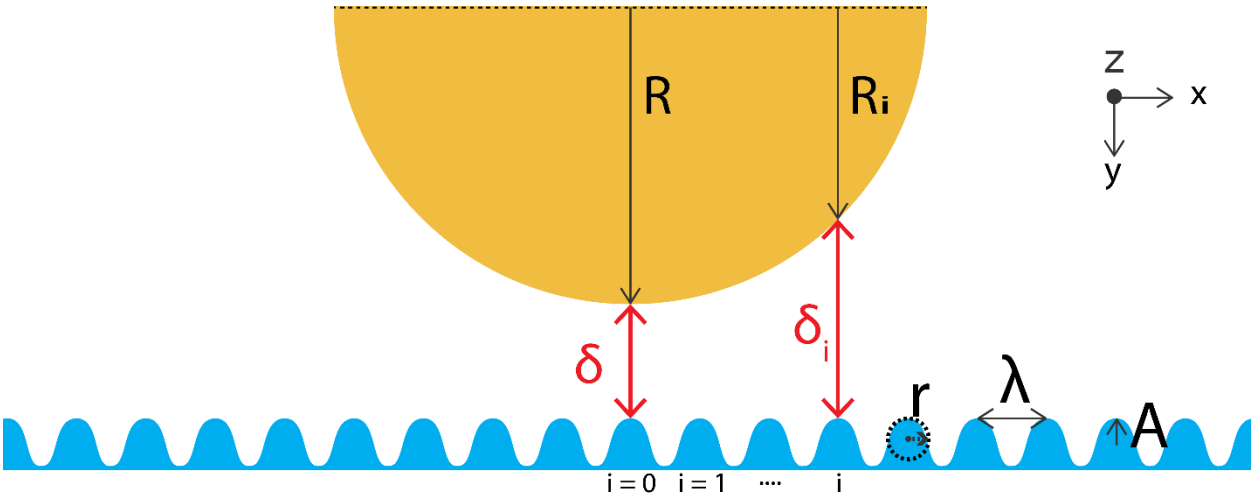

Figure 3.5: Schematic of the interaction between the hemispherical probe and the surface wrinkles.

Figure 3.5 shows the schematic of the model situation. A wrinkle, the location of which aligns with the centerline of the hemispherical probe, is the 0th wrinkle, and each wrinkle is termed the i^{th} wrinkle in the order of its position from the centerline. To predict the pull-off force between the hemispherical probe and the PDA/PDMS substrate, each wrinkle in the substrate is assumed to interact independently with the probe. The normal approach of the i^{th} wrinkle (located at iλ in the *x*-direction from the probe centerline) (δ_i) to the hemispherical probe is related to the hemispherical probe centerline normal approach δ by the following expression:

$$\delta_i = \delta - \left(R - \sqrt{R^2 - (i\lambda)^2}\right) \qquad \text{Eqn. 3.1}$$

where R is the radius of the hemispherical probe. R_i is the radius of the *y*-*z* plane cross-section of the hemispherical probe above the i^{th} wrinkle (**Figure 3.5**). The value of R_i can be expressed as:

$$R_i = \sqrt{R^2 - (i\lambda)^2} \qquad \text{Eqn. 3.2}$$

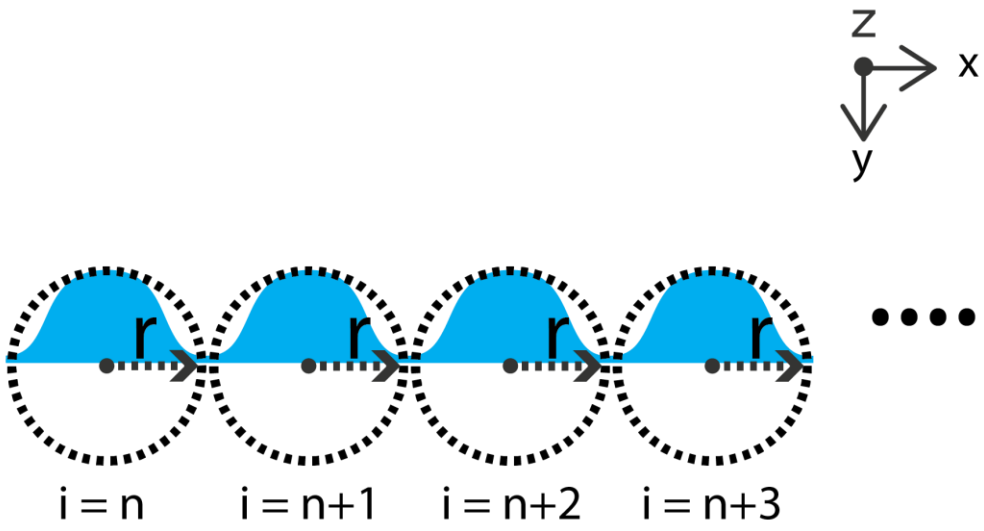

Figure 3.6: Schematic of the estimation of the wrinkle geometry as an array of cylinders.

To compute the interaction between a wrinkle and the probe, the geometry of the wrinkles is approximated as an array of cylinders each with radius r (**Figure 3.6**).[35,37] Radius of this

abstracted wrinkle-cylinder can be approximated as follows. In x-y plane, the surface profile of the wrinkle array of the PDA/PDMS surface can be described as follows (**Figure 3.7a**):

$$y = A\left(1 - \cos\left(\frac{2\pi}{\lambda}x\right)\right) \qquad \text{Eqn. 3.3}$$

As the parabolic approximation is employed for the profile of the cylinder for the JKR model,[38] the radius of the curvature of the wrinkle cylinder *r* can be estimated by choosing two points within a wrinkle (one being the peak point; (*x*,*y*) = (0,0)) and finding a parabola that intersects with those two points, with the following form:

$$y = \frac{\mathrm{x}^2}{2r} \qquad \text{Eqn. 3.4}$$

The value for *r* for a given cylinder is thus dependent on the point choice to estimate the parabola. The range of r can be computed. Rearranging Eqn. 3.4:

$$r = \frac{x^2}{2y} \qquad \text{Eqn. 3.5}$$

substituting Eqn. 3.3 for *y* yields the following expression for *r*:

$$r = \frac{\mathrm{x}^2}{2A\left(1-\cos\left(\frac{2\pi}{\lambda}x\right)\right)} \qquad \text{Eqn. 3.6}$$

A new expression is introduced: $\theta = \frac{2\pi}{\lambda}x$ such that Eqn. 3.6 becomes:

$$r = \mu\frac{\lambda^2}{2\pi^2 A} \qquad \text{Eqn. 3.7}$$

where the expression for μ is given by:

$$\mu = \frac{\theta^2}{1-cos\theta} \qquad \text{Eqn. 3.8}$$

For an individual wrinkle with a peak position of x = 0, the x range is $-\frac{\lambda}{2} < x < \frac{\lambda}{2}$, which corresponds to $-\pi < \theta < \pi$. Due to the symmetry, the range of θ for a given value of r value will be $0 < \theta < \pi$. **Figure 3.7b** shows the plot of μ vs. θ. Thus, depending on the reference point choice, the value of r ranges from $\frac{\lambda^2}{\pi^2 A}$ to $\frac{\lambda^2}{4A}$. The midpoint of $\theta = \frac{\pi}{2}$ was chosen such that $r = \frac{\lambda^2}{8A}$.

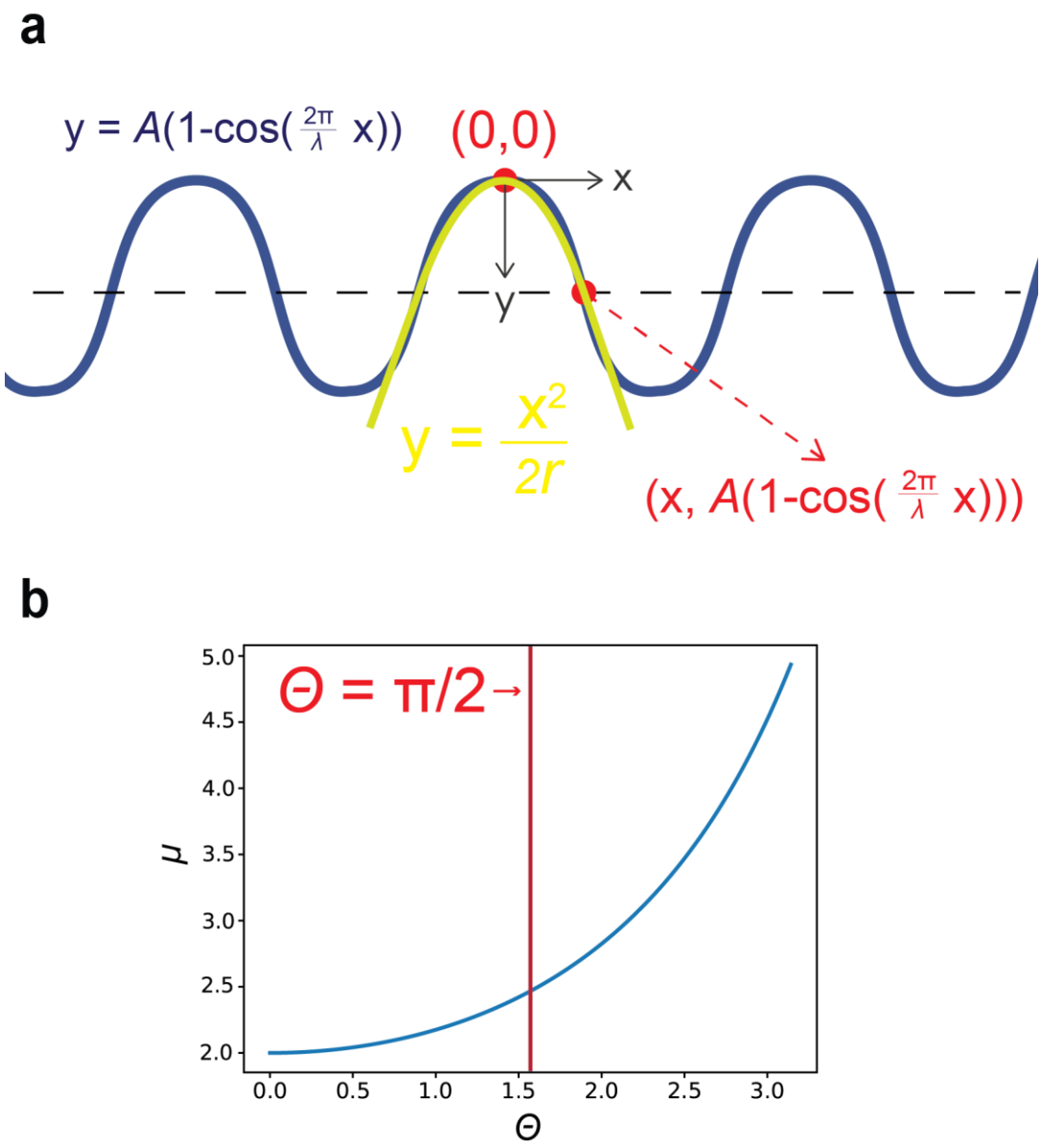

Figure 3.7: a) Schematic of the parabolic estimation process for the wrinkle cylinders. b) Plot of μ vs θ.

Now, since $R >> r$, (R ~ mm & r ~ um), it could be assumed that the i^{th} wrinkle interacts only with the small sub-section of the hemisphere that is cut along the y-z plane with the x-direction thickness corresponding to the wavelength of the wrinkle. The proposed assumption implies that the interaction between the i^{th} wrinkle and this sub-section of the probe can be modeled as the interaction between two orthogonally oriented cylinders with radii r and R_i, where R_i is the radius of the y-z plane cross-section of the hemispherical probe above the i^{th} wrinkle, as mentioned (**Figure 3.8**). The normal approach between the two cylinders δ_i will be tied to the centerline normal approach according to Eqn. 3.1.

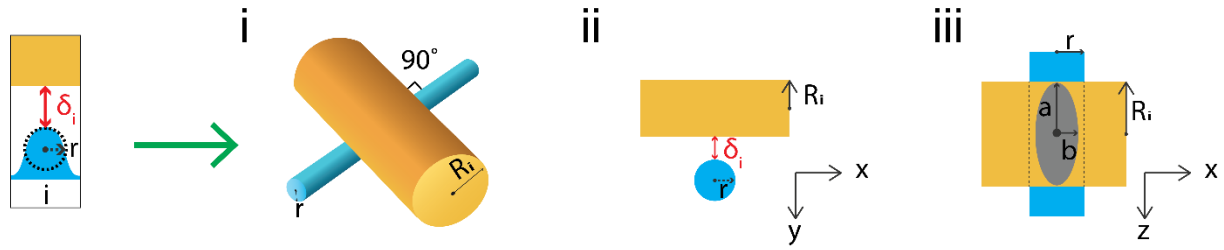

Figure 3.8: Two-cylinder approximation of the interaction between the i^{th} grating feature and the hemispherical probe. b-i) Abstraction of the interaction between the i^{th} wrinkle and the hemispherical probe. b-ii) View of the interaction along the x-y plane. b-iii) View of the interaction along the x-z plane.

This methodology of estimating the wrinkle to probe interaction with the interaction between two orthogonally oriented cylinders deviates from the efforts in the literature. Wrinkle-hemispherical probe interaction is usually estimated by interaction between an infinitely long cylinder and an infinite half-plane; in that methodology, only the line-force expression is acquired, and the line-length is obtained from the separate expression estimated from the hemispherical probe interaction with the flat plane, a practice that could give rise to self-inconsistency within the model.

For the interaction between two orthogonal cylinders with approximately equal radii, the contact region is approximately circular (and perfectly circular if $r = R_i$), and the spherical Johnson-

Kendall-Roberts (JKR) relation can approximate the force-normal approach relation.[39] For orthogonal cylinders with large radii difference, the elliptical JKR relation is more appropriate as the contact region is approximately elliptical and thus was used to model the force between the i^{th} wrinkle and the hemispherical probe (**Figure 3.8iii**). Since this is the brief overview of the elliptical JKR theory, derivation of the elliptical JKR theory is not covered here but could be found in reference [41].

The non-dimensional force between two orthogonal cylinders (i.e., the i^{th} wrinkle cylinder and the probe cylinder (with radius R_i) in the current study) with radius r and R_i ($\overline{f_\iota}$) is a function of non-dimensional normal approach between the cylinders and several geometric considerations including the ratio of axes of the contact region g, where $g = \frac{b}{a}$ and $a > b$ (**Figure 3.8iii**). The expressions for $\overline{f_\iota}$ and $\overline{\delta_\iota}$ and associated geometric factors α_i and β_i are:[40,41]

$$\overline{f_\iota} = \frac{8}{3\pi}\left[\frac{g(1-\sqrt{g})^2}{(\beta_i g^2-\alpha_i)^2}\right]\left[\frac{\alpha_i-\beta_i g^{\frac{5}{2}}}{1-\sqrt{g}} - \frac{1}{3}(\beta_i g^2 + \alpha_i)\right] \quad \text{Eqn. 3.9}$$

$$\overline{\delta_\iota} = \left(\frac{2^{\frac{7}{2}}}{9\pi^2}\right)^{\frac{2}{3}}\left[\frac{\sqrt{g}(1-\sqrt{g})}{\beta_i g^2-\alpha_i}\right]^{\frac{4}{3}}\left[2K(e)\frac{\left(\alpha_i-\beta_i g^{\frac{5}{2}}\right)}{1-\sqrt{g}} - \alpha_i B(e) - g^2\beta_i D(e)\right] \quad \text{Eqn. 3.10}$$

$$\beta_i = \frac{C(e)\lambda_i^2+C(e)+D(e)}{\lambda_i\left(B(e)C(e)+B(e)D(e)+g^2C(e)D(e)\right)} \quad \text{Eqn. 3.11}$$

$$\alpha_i = \frac{B(e)\lambda_i^2+g^2\lambda_i^2C(e)+g^2C(e)}{\lambda_i\left(B(e)C(e)+B(e)D(e)+g^2C(e)D(e)\right)} \quad \text{Eqn. 3.12}$$

where e is the eccentricity of the contact region ($e = \sqrt{1-g^2}$), λ_i is the ratio between the radii of cylinders $\lambda_i = \sqrt{\frac{r}{R_i}}$ where $R_i > r$. $K(e)$, $B(e)$, $C(e)$, and $D(e)$ are complete elliptic integrals that depend on the eccentricity of the contact region as follows:

$$K(e) = \int_0^{\frac{\pi}{2}} \frac{1}{\sqrt{1-e^2\sin^2(\psi)}}\, d\psi \qquad \text{Eqn. 3.13}$$

$$B(e) = \int_0^{\frac{\pi}{2}} \frac{\cos^2\psi}{\sqrt{1-e^2\sin^2(\psi)}}\, d\psi \qquad \text{Eqn. 3.14}$$

$$C(e) = \int_0^{\frac{\pi}{2}} \frac{\sin^2\psi\cos^2\psi}{\sqrt{1-e^2\sin^2(\psi)^3}}\, d\psi \qquad \text{Eqn. 3.15}$$

$$D(e) = \int_0^{\frac{\pi}{2}} \frac{\sin^2\psi}{\sqrt{1-e^2\sin^2(\psi)}}\, d\psi \qquad \text{Eqn. 3.16}$$

The non-dimensional values of force and normal approach distance can be converted into unitized counterparts through the following relationships:

$$\overline{f_\iota} = \frac{f_i}{3\pi R_{i,e}\mathrm{G_c}} \qquad \text{Eqn. 3.17}$$

$$\overline{\delta_\iota} = \frac{\delta_i(4E^*)^{\frac{2}{3}}}{\left(9\pi G_\mathrm{c}\sqrt{R_{i,e}}\right)^{\frac{2}{3}}} \qquad \text{Eqn. 3.18}$$

where E^* is the equivalent elastic modulus between interacting bodies, G_c is the work of adhesion between two surfaces, and $R_{i,e}$ is the geometric mean of the radius between two bodies given by $R_{i,e} = \sqrt{rR_i}$. A plot of $\overline{f_\iota}$ vs. $\overline{\delta_\iota}$can be constructed by linking $\overline{f_\iota}$ and $\overline{\delta_\iota}$ for a given value of g in Eqns. 3.9 through 3.12. **Figure 3.9** shows the exemplary plots of $\overline{f_\iota}$ vs $\overline{\delta_\iota}$ for the elliptical JKR model and the spherical JKR model (**See Appendix**). The spherical JKR model clearly overestimates the tensile force compared to the elliptical model and comparatively underestimates the compressive force.

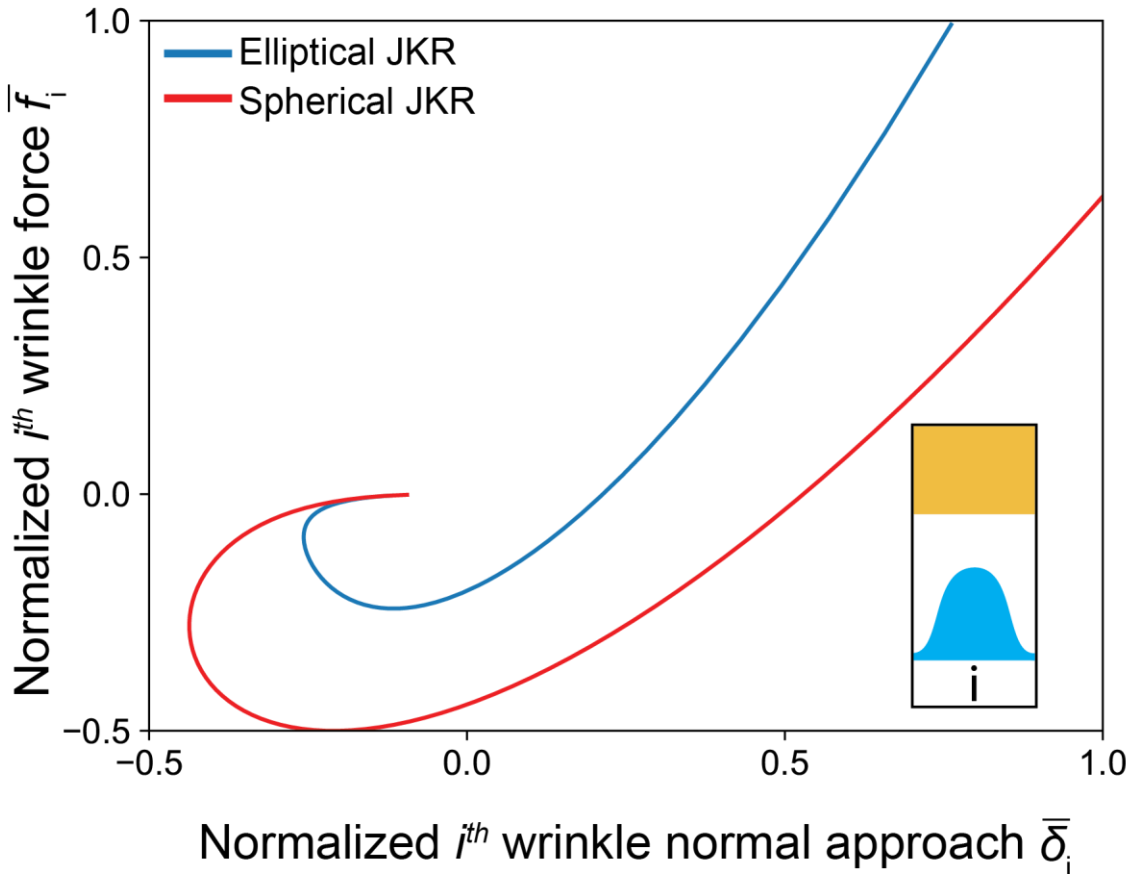

Figure 3.9: Computed exemplary force-[normal approach] curves between the i^{th} wrinkle and the probe with the elliptical and spherical JKR models.

The total force between the probe and the PDA/PDMS substrate F at a normal approach of δ will be a summation of the force that each wrinkle exerts onto the probe in the following form:

$$F(\delta) = \sum_{i=0}^{i=n} 2f_i(\delta_i, \lambda_i) - f_0(\delta_0, \lambda_0) \qquad \text{Eqn. 3.19}$$

The value of i ranges from $i = 0$ (centerline wrinkle) to $i = n$ where the $(n+1)^{th}$ wrinkle is the first wrinkle not in contact with the probe for a given value of δ. The pre-factor of two accounts for symmetry while the subtracted term offsets double counting of the force from the centerline wrinkle.

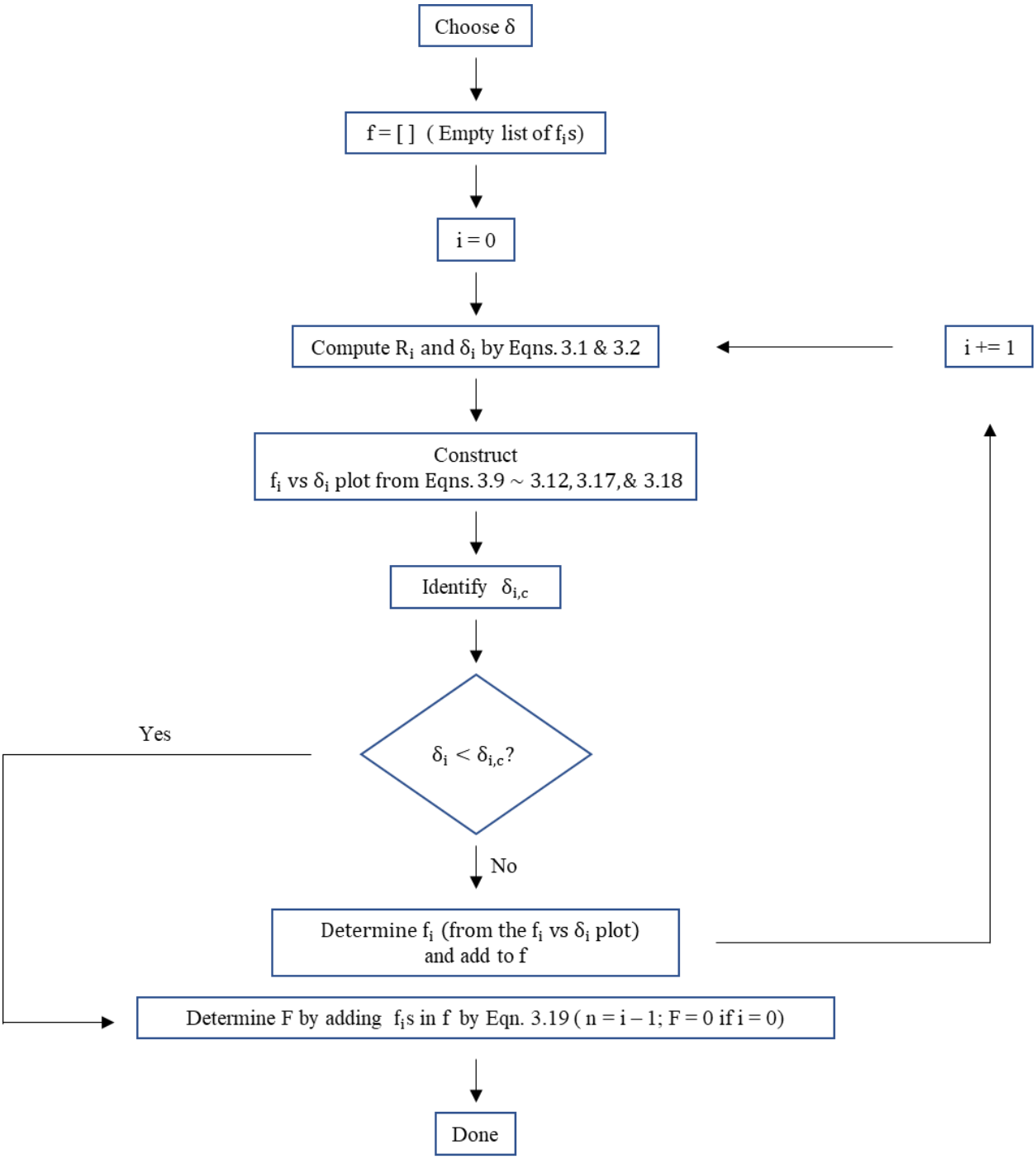

Figure 3.10: Flow chart for the calculation of F for a given δ.

A flow-chart for the actual implementation of Eqn. 3.19 to determine F for a given δ is shown in **Figure 3.10**. Starting from the center wrinkle ($i = 0$), for a given δ, δ_i and R_i was calculated according to Eqns. 3.1 and 3.2, and f_i vs. δ_i plot was constructed using Eqns. 3.9

through 3.12, Eqn. 3.17, and Eqn. 3.18. From the plot of f_i vs δ_i, the point of the maximum tensile force was identified, and the normal approach at the point was termed $\delta_{i,critical}$ (**Figure 3.11**). As the f_i vs δ_i curve is only physically valid for $\delta_i > \delta_{i,critical}$, the i^{th} wrinkle can be considered as non-interacting (not in contact) with the probe if $\delta_i < \delta_{i,critical}$ and all the subsequent wrinkles lies to the right of the i^{th} wrinkle won't be interacting as well. Thus, $f_i = 0 \; if \; \delta_i < \delta_{i,critical}$, and if $\delta_i > \delta_{i,critical}$, f_i can be determined by finding numerically or analytically reading off the f_i value corresponding to the given δ_i value from the f_i vs δ_i plot. If $\delta_i > \delta_{i,critical}$, the same process repeats for the next wrinkle (i+1), but if $\delta_i < \delta_{i,critical}$, the current i value subtracted by 1 (i - 1) becomes the upper limit for the summation (n) in Eqn. 3.19, and identified f_is are summated according to Eqn. 3.19 to yield F.

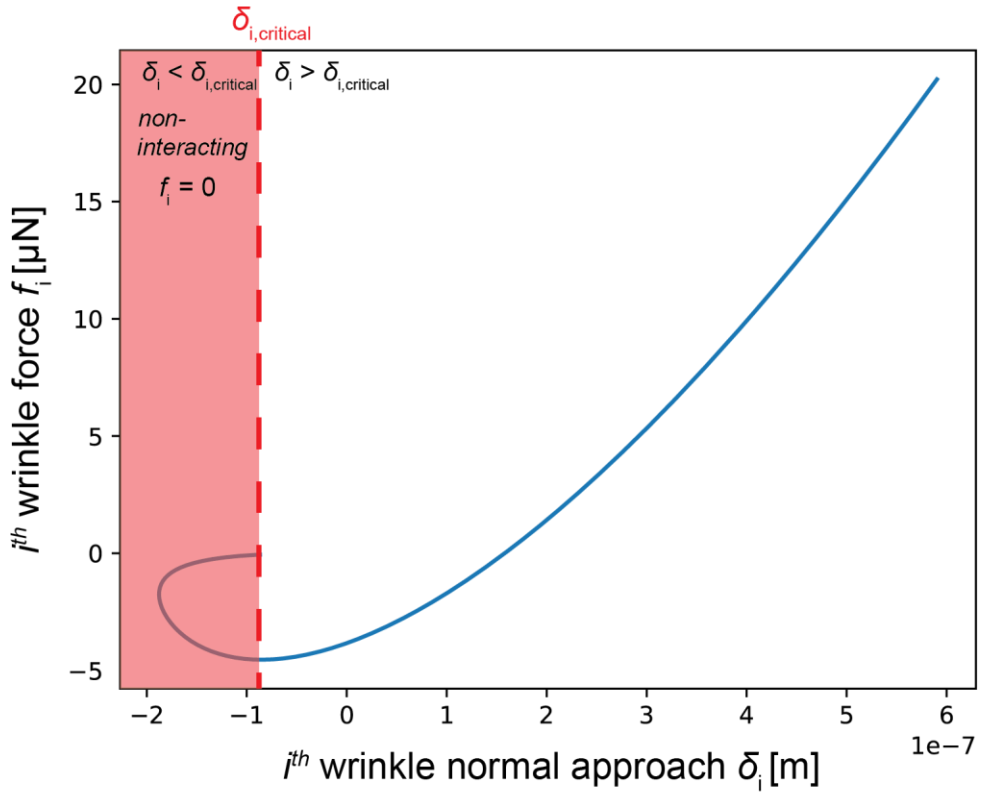

Figure 3.11: A representative plot of the force between the i^{th} wrinkle and the probe vs the normal approach of the i^{th} wrinkle to the probe. The normal approach at the smallest force (maximum tensile force) is the critical normal approach $\delta_{i,critical}$.

The above process can be repeated for a range of δ values (minimum $\delta = \delta_{0,critical}$) to produce a plot of F vs δ curve until the minimum is identified. **Table 3.1** shows the value of the parameters used to construct F vs δ curve. A and λ were measured from the AFM data, and r were calculated according to $r = \frac{\lambda^2}{8A}$. E^* and $G_c(\mathrm{W_{ad}})$ were taken from the JKR fit of the loading portion of the data from the indentation measurements with $\varepsilon_0 = 0\%$ samples. G_c (W_{ad}) from the loading phase was used, as the W_{ad} for unloading part occurs only after the surfaces come into the contact, and thus the surface contact profile is more likely to be governed by W_{ad} from the loading.

Table 3.1: Values used for the computation of the F vs. δ curve.

ε_0 (%)	A (nm)	λ (μm)	r (μm)	R (mm)	E^* (MPa)	G_c (mN/m)
10	19.6	1.13	8.14	3	2.6	25.5
20	32.1	0.89	3.08	3	2.6	25.5
30	95.6	0.88	1.01	3	2.6	25.5
40	100.9	0.84	0.87	3	2.6	25.5
50	116.1	0.82	0.72	3	2.6	25.5

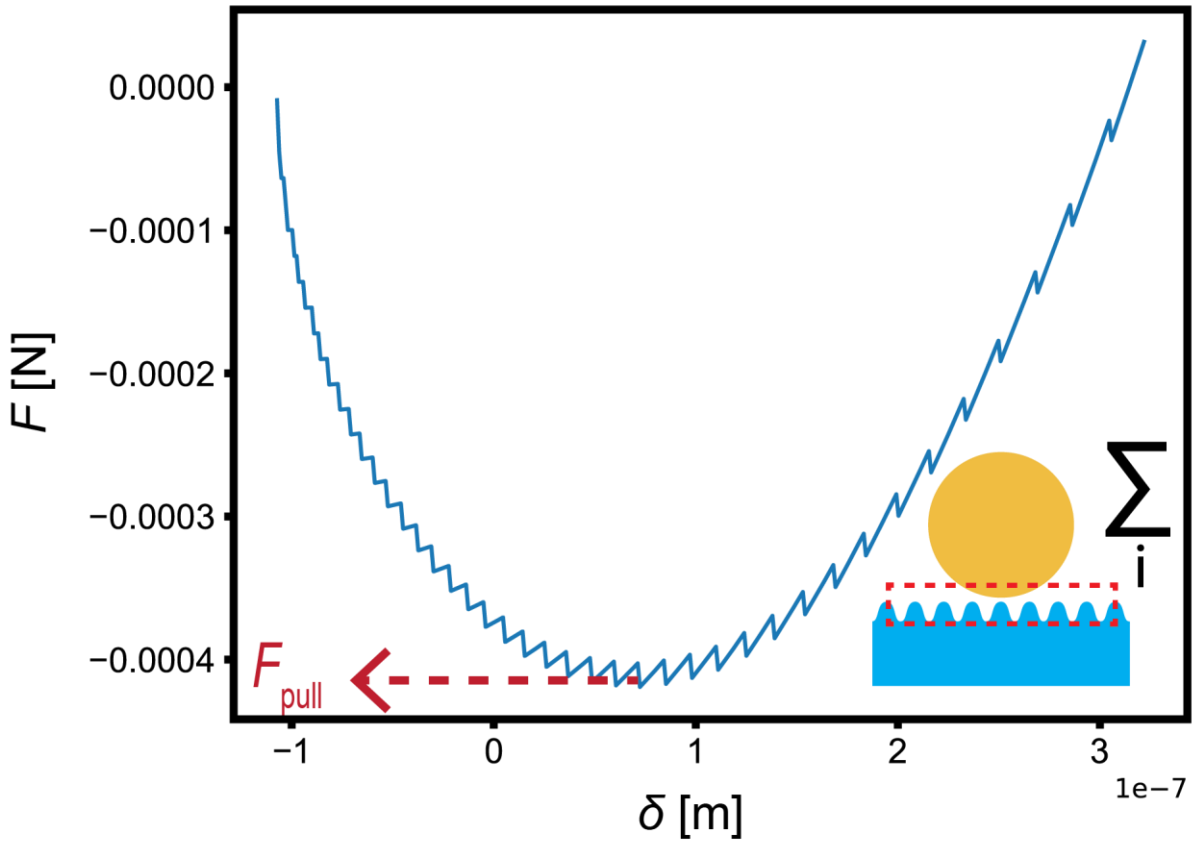

Figure 3.12: A representative plot of force-[normal approach] (F vs δ) between the probe and the PDA/PDMS substrate.

Figure 3.12 shows a representative F vs δ curve for the PDA/PDMS composite. F_{pull} was measured as the minimum value in plots of F vs δ (**Figure 3.12**). The measured F_{pull} was normalized with the theoretical flat surface pull-off force ($F_{\text{pull,flat}} = 1.5\pi G_c R; G_c = 25.5\ \frac{mN}{m}$ & $R = 3\ mm$) to yield the normalized pull-off force ($\overline{F_{\text{pull}}}$). **Figure 3.13a** shows the plot of $\overline{F_{\text{pull}}}$ vs the pre-strain used to fabricate the PDA/PDMS samples. Values of $\overline{F_{\text{pull}}}$ predicted using the JKR theory with elliptical contact area are in a good agreement with the experimental results, which is surprising in that many assumptions were made along the process. Conversely, JKR theory with a circular contact area significantly overestimates the value of $\overline{F_{\text{pull}}}$ (**See Appendix**) as expected given that the spherical model overestimates the tensile force and

underestimates the compressive force. $\overline{F_{\text{pull}}}$ values were also plotted against the wrinkle amplitude, which is directly proportional to the pre-strain applied.

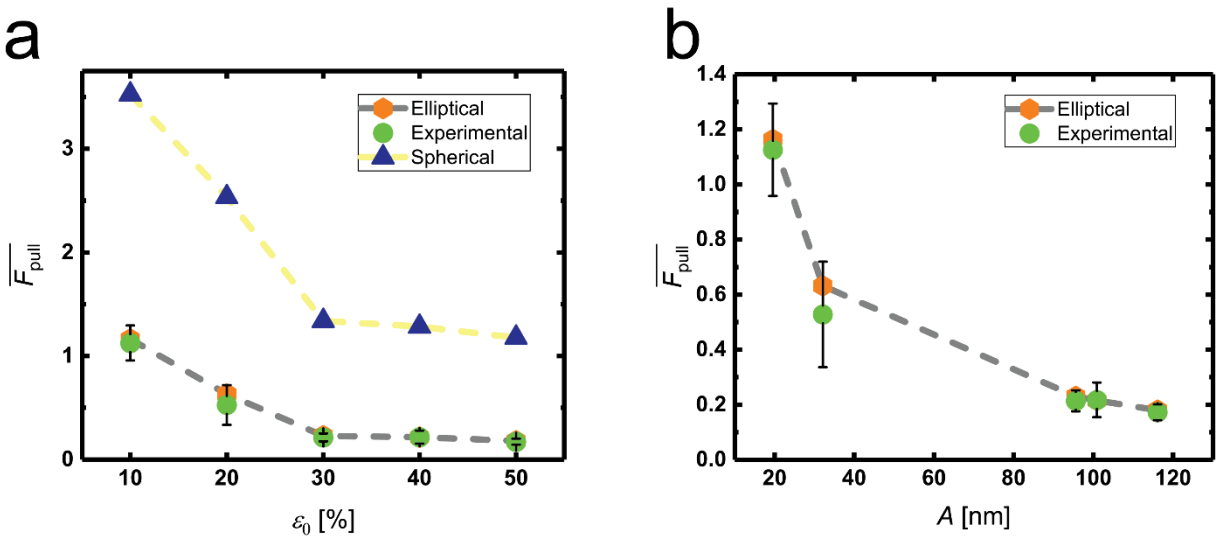

Figure 3.13: a) Plot of the normalized pull-off force vs the pre-strain for the elliptical JKR model, experimental, and the spherical JKR model. b) Plot of the normalized pull-off force vs the amplitude of the PDA/PDMS substrates.

The higher accuracy of the proposed model compared to the scaling model in the literature is attributed to two things. The first reason is that the geometric effect of a spherical probe, which imposes each wrinkle in the surface to go through a different tension-compression state at a given normal approach, were individually taken care of, instead of lump-sum averaging often employed in the literature. The second reason is that the finite size effect of the contact region was systematically taken care of using the elliptical JKR model instead of using the infinite cylinder to infinite plane model, which estimates the line-length from a phenomenological estimation. Utilizing the elliptical JKR theory to approximate the interaction between a wrinkle to the hemispherical probe, the proposed model captures the essence of evolution of pull-off force with the wrinkle geometry and predicts the pull-off force between the wrinkle array to the hemispherical probe in a self-consistent manner by accounting in the contact region geometry under an unified

theory. However, caution should be noted in the model implementation as to apply the model only to the cases where the assumed assumptions are reasonably valid. For instance, if the probe's feature size is not large compared to the wrinkle geometry or the estimation of the wrinkle geometry through the cylinder is not reasonable (e.g.$\frac{\lambda}{A}$ either too small or big), the model is expected to deviate from the experiment.

3.4 Conclusion

In summary, Chapter 3 has discussed the PDA interface adhesion modulation through dynamic control of the interface features through thin-film buckling. Surface wrinkles were introduced onto the PDA/PDMS substrates through modulus mismatch driven thin-film buckling through applications of pre-strains, and the variation of the wrinkle geometry were realized by varying the pre-strain applied. The variation of the wrinkle geometry translated to the variation of adhesion, and it was shown that the adhesion of the PDA/PDMS substrate could be switched on and off real-time through application of the cyclic strain. A model based on the elliptical JKR theory was proposed to model the effect of wrinkle geometry to adhesion by estimating the interaction between the individual wrinkle to the probe as the interaction between two cylinders with different radii. The force that each wrinkle experiences at a given normal approach of the probe were summated to yield the overall force, and the theory prediction well matched with the experimental results.

3.5 References

1 Autumn, K. *et al.* Adhesive force of a single gecko foot-hair. *Nature* **405**, 681-685 (2000).

2 Autumn, K. *et al.* Evidence for van der Waals adhesion in gecko setae. *P Natl Acad Sci USA* **99**, 12252-12256, doi:10.1073/pnas.192252799 (2002).

3 Persson, B. N. J. On the mechanism of adhesion in biological systems. *The Journal of Chemical Physics* **118**, 7614-7621, doi:10.1063/1.1562192 (2003).

4 Glassmaker, N. J., Jagota, A., Hui, C.-Y., Noderer, W. L. & Chaudhury, M. K. Biologically inspired crack trapping for enhanced adhesion. *Proceedings of the National Academy of Sciences* **104**, 10786 (2007).

5 Bhushan, B. Biomimetics: lessons from nature–an overview. *Philosophical Transactions of the Royal Society A: Mathematical, Physical and Engineering Sciences* **367**, 1445-1486, doi:10.1098/rsta.2009.0011 (2009).

6 Geim, A. K. *et al.* Microfabricated adhesive mimicking gecko foot-hair. *Nat Mater* **2**, 461-463, doi:10.1038/nmat917 (2003).

7 Glassmaker, N. J., Jagota, A., Hui, C. Y. & Kim, J. Design of biomimetic fibrillar interfaces: 1. Making contact. *J Roy Soc Interface* **1**, 23-33, doi:10.1098/rsif.2004.0004 (2004).

8 Sitti, M. & Fearing, R. S. Synthetic gecko foot-hair micro/nano-structures as dry adhesives. *Journal of Adhesion Science and Technology* **17**, 1055-1073, doi:10.1163/156856103322113788 (2003).

9 Mahdavi, A. *et al.* A biodegradable and biocompatible gecko-inspired tissue adhesive. *Proceedings of the National Academy of Sciences* **105**, 2307-2312, doi:10.1073/pnas.0712117105 (2008).

10 P., M. M., Burak, A. & Metin, S. Gecko-Inspired Directional and Controllable Adhesion. *Small* **5**, 170-175, doi:doi:10.1002/smll.200801161 (2009).

11 F., B. L., Christian, G., Eduard, A. & Aránzazu, d. C. Gecko-Inspired Surfaces: A Path to Strong and Reversible Dry Adhesives. *Advanced Materials* **22**, 2125-2137, doi:doi:10.1002/adma.200903200 (2010).

12 Greiner, C., del Campo, A. & Arzt, E. Adhesion of Bioinspired Micropatterned Surfaces: Effects of Pillar Radius, Aspect Ratio, and Preload. *Langmuir* **23**, 3495-3502, doi:10.1021/la0633987 (2007).

13 del Campo, A., Greiner, C. & Arzt, E. Contact Shape Controls Adhesion of Bioinspired Fibrillar Surfaces. *Langmuir* **23**, 10235-10243, doi:10.1021/la7010502 (2007).

14 P., C. E., J., S. E., C., H. R. & J., C. A. Surface Wrinkles for Smart Adhesion. *Advanced Materials* **20**, 711-716, doi:doi:10.1002/adma.200701530 (2008).

15 Rahmawan, Y., Chen, C.-M. & Yang, S. Recent advances in wrinkle-based dry adhesion. *Soft Matter* **10**, 5028-5039, doi:10.1039/C4SM00027G (2014).

16 Bowden, N., Brittain, S., Evans, A. G., Hutchinson, J. W. & Whitesides, G. M. Spontaneous formation of ordered structures in thin films of metals supported on an elastomeric polymer. *Nature* **393**, 146, doi:10.1038/30193 (1998).

17 Young, C. J., J., N. A. & M., S. C. Surface Wrinkling: A Versatile Platform for Measuring Thin-Film Properties. *Advanced Materials* **23**, 349-368, doi:doi:10.1002/adma.201001759 (2011).

18 Stafford, C. M. *et al.* A buckling-based metrology for measuring the elastic moduli of polymeric thin films. *Nat Mater* **3**, 545, doi:10.1038/nmat1175 (2004).

19 Luke, K., Zeeshan, A., Venkatasubramanian, V. & J., B. C. Synthesis and Measurement of Cohesive Mechanics in Polydopamine Nanomembranes. *Advanced Materials Interfaces* **4**, 1700041, doi:doi:10.1002/admi.201700041 (2017).

20 Ryu, J. H., Messersmith, P. B. & Lee, H. Polydopamine Surface Chemistry: A Decade of Discovery. *ACS Applied Materials & Interfaces* **10**, 7523-7540, doi:10.1021/acsami.7b19865 (2018).

21 Seonki, H. *et al.* Air/Water Interfacial Formation of Freestanding, Stimuli-Responsive, Self-Healing Catecholamine Janus-Faced Microfilms. *Advanced Materials* **26**, 7581-7587, doi:doi:10.1002/adma.201403259 (2014).

22 Hillborg, H. *et al.* Crosslinked polydimethylsiloxane exposed to oxygen plasma studied by neutron reflectometry and other surface specific techniques. *Polymer* **41**, 6851-6863, doi:https://doi.org/10.1016/S0032-3861(00)00039-2 (2000).

23 Béfahy, S. *et al.* Thickness and Elastic Modulus of Plasma Treated PDMS Silica-like Surface Layer. *Langmuir* **26**, 3372-3375, doi:10.1021/la903154y (2010).

24 Lee, H., Dellatore, S. M., Miller, W. M. & Messersmith, P. B. Mussel-Inspired Surface Chemistry for Multifunctional Coatings. *Science* **318**, 426 (2007).

25 Mangipudi Venkata, S., Huang, E., Tirrell, M. & Pocius Alphonsus, V. Measurement of interfacial adhesion between glassy polymers using the JKR method. *Macromolecular Symposia* **102**, 131-143, doi:10.1002/masy.19961020118 (1996).

26 Johnston, I. D., McCluskey, D. K., Tan, C. K. L. & Tracey, M. C. Mechanical characterization of bulk Sylgard 184 for microfluidics and microengineering. *Journal of Micromechanics and Microengineering* **24**, 035017 (2014).

27 Johnson, K. L., Kendall, K. & Roberts, A. Surface energy and the contact of elastic solids. *Proc. R. Soc. Lond. A* **324**, 301-313 (1971).

28 Weinhold, M. *et al.* Structure and Bonding of the Multifunctional Amino Acid l-DOPA on Au(110). *The Journal of Physical Chemistry B* **110**, 23756-23769, doi:10.1021/jp064956t (2006).

29 Oláh, A., Hillborg, H. & Vancso, G. J. Hydrophobic recovery of UV/ozone treated poly(dimethylsiloxane): adhesion studies by contact mechanics and mechanism of surface modification. *Applied Surface Science* **239**, 410-423, doi:https://doi.org/10.1016/j.apsusc.2004.06.005 (2005).

30 Rundlöf, M. *et al.* Application of the JKR Method to the Measurement of Adhesion to Langmuir–Blodgett Cellulose Surfaces. *Journal of Colloid and Interface Science* **230**, 441-447, doi:https://doi.org/10.1006/jcis.2000.7108 (2000).

31 Sun, Y. & Walker, G. C. Viscoelastic Response of Poly(dimethylsiloxane) in the Adhesive Interaction with AFM Tips. *Langmuir* **21**, 8694-8702, doi:10.1021/la050448j (2005).

32 Waters, J. F., Lee, S. & Guduru, P. R. Mechanics of axisymmetric wavy surface adhesion: JKR–DMT transition solution. *International Journal of Solids and Structures* **46**, 1033-1042, doi:https://doi.org/10.1016/j.ijsolstr.2008.10.013 (2009).

33 Guduru, P. R. Detachment of a rigid solid from an elastic wavy surface: Theory. *Journal of the Mechanics and Physics of Solids* **55**, 445-472, doi:https://doi.org/10.1016/j.jmps.2006.09.004 (2007).

34 Lin, P.-C., Vajpayee, S., Jagota, A., Hui, C.-Y. & Yang, S. Mechanically tunable dry adhesive from wrinkled elastomers. *Soft Matter* **4**, 1830-1835, doi:10.1039/B802848F (2008).

35 Davis, C. S. & Crosby, A. J. Mechanics of wrinkled surface adhesion. *Soft Matter* **7**, 5373-5381, doi:10.1039/C1SM05146F (2011).

36 Santanu, K., S., D. C., Thomas, L., Ravi, S. & J., C. A. Adhesion of nonplanar wrinkled surfaces. *Journal of Polymer Science Part B: Polymer Physics* **49**, 179-185, doi:doi:10.1002/polb.22181 (2011).

37 Rahmawan, Y., Chen, C. M. & Yang, S. Recent advances in wrinkle-based dry adhesion. *Soft Matter* **10**, 5028-5039, doi:10.1039/c4sm00027g (2014).

38 Chen, S. H. Extension of the Two-Dimensional JKR Theory to the Case with a Large Contact Width. *Springer Theses-Reco*, 19-26, doi:10.1007/978-3-662-46955-2_2 (2015).

39 Fischer-Cripps, A. C. *Introduction to contact mechanics*. Vol. 101 (Springer, 2007).

40 Sümer, B., Onal, C. D., Aksak, B. & Sitti, M. An experimental analysis of elliptical adhesive contact. *J Appl Phys* **107**, 113512, doi:10.1063/1.3428494 (2010).

41 Johnson, K. L. & Greenwood, J. A. An approximate JKR theory for elliptical contacts. *Journal of Physics D: Applied Physics* **38**, 1042 (2005).

Chapter 4

Chemical Modulation of Adhesion in PDA

(Disclaimer: The following chapter includes results from a collaboration for the resultant publication of which, myself is a co-first author. My co-author collected data in section 4.3.2. All the figures, analysis, and writing presented in this chapter are my own, unless otherwise noted.)

4.1 Introduction

4.1.1 Background

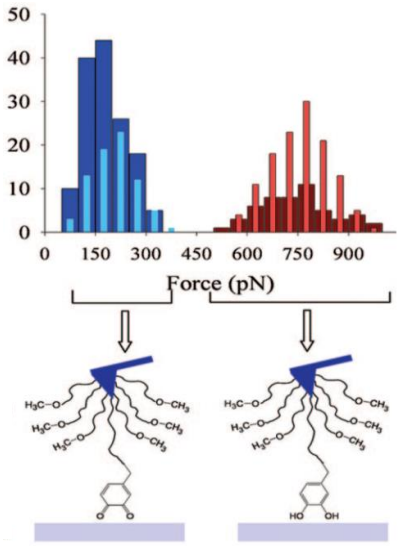

Figure 4.1: Adhesion force measurement between catechol and TiO_2 surface at pH = 9.7 (right) and pH = 8.3 (left). The bimodal distribution of adhesion force was attributed to the differential adhesion of catechol at different oxidation states. Reproduced from [1]

Several studies revealed that the adhesion strength of catechol molecule is the strong function of its oxidation state (**Figure 4.1**).[1-7] Dihydroxyl functionality in the reduced state of catechol makes its interfacial interaction with interfaces, where H-bonding is the primary adhesive interaction scheme with catechol, more favorable than its oxidized form quinone, although the latter can readily participate in cross-linking with many organic molecules due to its highly reactive nature.[1,8-10] Another remarkable feature of catechol is the reversible yet strong nature of its adhesive scheme. For instance, a single molecule study of catechol adhesion to TiO_2 surfaces

underwater revealed that the catechol adhesion to TiO_2 surface is reversible with the adhesion strength reaching up to 40% the bond strength of a covalent bond, the highest value reported thus far for the reversible bond involving a biological molecule.[4] Additionally, a single molecule transition between catechol and quinone shows reversibility with a strong pH dependency.[11-14] Exhibiting oxidation state reversibility with differential adhesion at each state, catechol possesses a potential for reversible control of adhesion through various chemical means such as pH control or external voltage.[15]

As the catechol is one of the primary molecular building blocks in polydopamine (PDA),[16-18] the same adhesion controllability could extend to PDA by means of the oxidation state change of the constituent catechol molecules in PDA through chemical means. Some indirect evidences support the assertion though never has been systematically evaluated.[19] As the single catechol molecule exhibits reversible chemistry, there also is a possibility of tuning PDA's adhesion reversibly; however, caution should be noted. Even though the single molecule chemistry of catechol is reversible, highly reactive quinones can go through various irreversible covalent couplings with other radicals and nucleophilic counterparts, losing their reversible controllability.[20-24]

The exact structure of PDA is still an active area of academic investigation, but it is generally accepted that PDA is characterized by extreme structural and chemical heterogeneity where catechol moieties exist in various forms and oxidation states.[8,16,17] Thus, even though a speculation based on a single molecule catechol chemistry is possible, given the heterogeneous nature of PDA and as the thermodynamics of chemisorption is expected to be different in an polymeric (oligomeric) form than in a free molecule,[25] an experimental study is needed to confirm the PDA adhesion's chemical controllability.

Chapter 4 discusses the chemical controllability of PDA's adhesion via external voltage applied and pH control. Series of electrochemical measurements and indentation measurements were carried out.

4.1.2 Review of Electrochemical Impedance Spectroscopy

As PDA is known to exhibit a certain degree of mixed electronic-ionic conductivity,[26] electrochemical methods are appropriate tools to investigate the chemical mechanisms within PDA. Electrochemical Impedance Spectroscopy (EIS) is a characterization tool that studies the system response to the small ac signal, typically a sinusoidal voltage signal. EIS was initially developed to determine the double-layer capacitance and now is used to study many electrode processes and complex interface dynamics.[27] This tool is especially useful for the study of systems that exhibit time lag to the applied electrical stimuli, typically ionic systems. For EIS, the voltage signal is applied to a system:

$$E(t) = E_0 \exp(jwt) \qquad \text{Eqn. 4.1}$$

One gets the current response of the system:

$$I(t) = I_0 \exp(iwt - i\phi) \qquad \text{Eqn. 4.2}$$

The impedance of the system at frequency *w* can be obtained:

$$Z = \frac{E}{I} = Z_0 \exp(i\phi) = Z_0(cos\phi + isin\phi) \qquad \text{Eqn. 4.3}$$

where Z_0 represents the modulus (magnitude) of the impedance and ϕ represents the phase of the impedance. These measurements are carried out at different frequencies, and one can fit the impedance spectrum to a known model to extract physical parameters of the system. While one

can obtain much information about a system by the qualitative assessment of the impedance spectrum, the equivalent circuit modeling is the most widely used fitting scheme to extract the quantitative physical parameters from the impedance spectrum. For many of electrochemical processes, the functional relation between the current and the applied voltage is known. However, often cases, these functional forms are too complicated that the direct fitting of impedance data to these models is often impractical if not impossible. For that reason, one linearizes the functional forms of these equations to yield the simpler impedance form, a practice that is justified due to the small amplitude used in EIS. For example, redox reaction at the solution/redox active electrode interface follows the following equation:

$$i = nF\left(k_b C_R(0) - k_f C_O(0)\right) \qquad \text{Eqn. 4.4}$$

where i is the current, n is the number of electrons exchanged in the process, $C_O(0)$ and $C_R(0)$ are the surface concentrations of the Ox and Red species, respectively, and k_f and k_b are the potential dependent heterogeneous rate constants of the forward (reduction) and backward (oxidation) processes:[28]

$$k_f = k^0 \exp\left(-\alpha n f(E - E^0)\right) \qquad \text{Eqn. 4.5}$$

$$k_b = k^0 \exp((1-\alpha) n f(E - E^0)) \qquad \text{Eqn. 4.6}$$

$k^0$is the heterogeneous rate constant at the standard potential, α is the transfer coefficient, n is the number of electrons exchanged, f = F/RT, F is the Faraday constant, R is the gas constant, and T is the absolute temperature in Kelvin, and E^0 is the standard redox potential. When linearization is done with the small ac signal assumption, the impedance form of the redox process takes the following form:[28]

$$Z_{faradaic\ process} = R_{ct} + Z_w \qquad \text{Eqn. 4.7}$$

$$R_{ct} = \frac{RT}{n^2F^2}\left(\frac{1}{\alpha k_f C_O(0)+(1-\alpha)k_b C_R(0)}\right) \quad \text{Eqn. 4.8}$$

$$Z_w = warburg\ impedance \quad \text{Eqn. 4.9}$$

R_{ct} accounts for the charge transfer resistance for electrons to cross the interface between the electrode and redox active species, and as one can see doesn't have the frequency dependence. Z_w, often called Warburg impedance, accounts for the impedance rising from diffusion of redox species from the bulk solution to the electrode interface and has a different functional form for different boundary conditions. For the case of semi-infinite diffusion:

$$Z_w = \frac{RT}{n^2F^2}\frac{\frac{k_f}{\sqrt{jwD_O}}+\frac{k_b}{\sqrt{jwD_R}}}{\alpha k_f C_O(0)+(1-\alpha)k_b C_R(0)} \quad \text{Eqn. 4.10}$$

where D_O and D_R are diffusion coefficient of Ox and Red species.

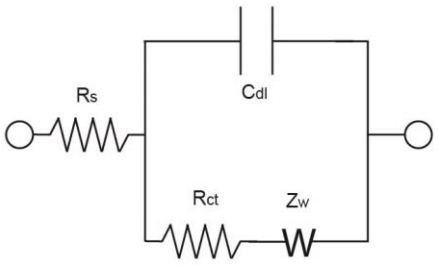

Figure 4.2: Randles circuit for a redox active electrode

After getting the impedance form of physiochemical constituents in the system by simplifying the functional form of physiochemical processes, these impedance forms can be added up by circuit rule to yield the equivalent circuit of the system. **Figure 4.2** is an example of such, which represents the equivalent circuit for a redox-active electrode. R_s is the solution resistance, which accounts for the ohmic drop within the bulk solution, and C_{dl} is the double layer capacitance, the impedance form of which is $1/(jwC_{dl})$ or $1/((jw)^a Y_0)$, if the electrode surface is

rough. R_{ct} and Z_w are as defined by Eqn. 4.8 and 4.10 respectively. Following the circuit addition rule, the impedance of the system takes the following form:

$$Z_{sys} = R_s + \frac{Z_{C_{dl}}(R_{ct}+Z_w)}{Z_{C_{dl}}+R_{ct}+Z_w} \quad \text{Eqn. 4.11}$$

$$Z_{C_{dl}} = \frac{1}{jwC_{dl}} \text{ or } \frac{1}{(jw)^a Y_0} \quad \text{Eqn. 4.12}$$

It is to Z_{sys} that the fitting is occurred with the acquired impedance spectrum. For the redox inactive electrode where no Faradaic reaction takes at the electrode interface, R_{ct}- Z_w branch is absent (**Figure 4.2**), and the equivalent circuit is just the series combination of R_s and C_{dl}. One can get a lot of information about the electrode interface through this fitting, and the same was done in this report to gather information about PDA.

4.2 Methods

4.2.1 Materials

Dopamine hydrochloride (98%), sodium bicarbonate (>99%), sodium carbonate (>99%), phosphate buffered saline (0.01M), sodium chloride (>99%), citric acid (>99.5%), and sodium hydroxide (>97%) were purchased from Sigma-Aldrich (St. Louis, MO USA) and used as received. Tris(hydroxymethyl) aminomethane (Tris) and sodium phosphate dibasic (99.2%) was purchased from Fisher Scientific (Hampton, NH USA) and used as received. Water was purified (18.2 MΩ-cm) using Direct-Q 3 UV-R system (Millipore). Silicon wafers with 1 μm thermal oxide were purchased from Silicon Quest International (San Jose, CA USA; 4" diameter, phosphorus doped). Indium tin oxide (ITO) was purchased from University Wafer (Boston, MA USA; 20 Ω /sq). Sylgard 184 (Polydimethylsiloxane) was purchased from Dow Corning (Midland, MI USA). Borosilicate glass hemispherical probes were purchased from Edmund Optics

(Barrington, NJ, USA; 6mm diameter). Epoxy was purchased from Loctite (Düsseldorf, GER; Aqua Marine Epoxy). 3-aminopropyltriethoxysilane (APTES) was purchased from Gelest (Morrisville, PA USA). UV Glue was purchased from Norland Product (Cranbury, NJ USA; Norland Optical Adhesive 81).

4.2.2 PDA Films for Electrochemical Measurement Preparation

PDA films were deposited through auto-oxidative polymerization from aqueous dopamine solutions.[29] ITO substrates were cleaned by sonication in acetone and isopropyl alcohol (IPA) respectively and then rinsed with deionized water. Substrates were then cleaned by UV and ozone (30 mW/cm^2, 20min; Jelight, Irvine, CA USA). Cleaned ITO substrates were immersed in 2 mg/ml of dopamine hydrochloride in 50mM carbonate/bicarbonate buffer solution (pH = 8.5) for 16 h under rotary shaking (65 rpm). The same deposition procedure was repeated up to three times, changing the dopamine hydrochloride solution with freshly prepared ones every 16 h.

4.2.3 Electrochemical Measurements of PDA Samples

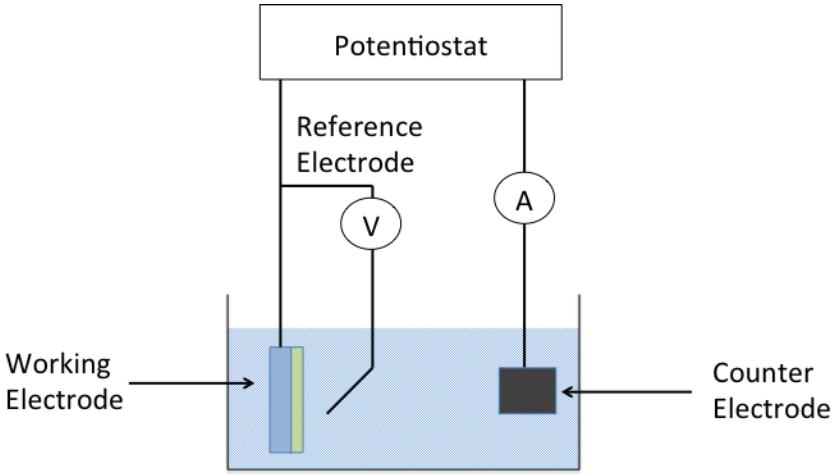

Figure 4.3: Schematic of a three-electrode electrochemical cell

All electrochemical experiments were done in a conventional three-electrode setup, with an Ag/AgCl electrode (Koslow Scientific, Englewood, NJ USA) as a reference electrode and with Pt foil as a counter electrode in 0.01M phosphate buffered saline solution (**Figure 4.3**). Electrochemical Impedance measurements were done with a Gamry Interface 1000 potentiostat (Gamry Instruments, Warminster, PA USA) in the frequency range of 0.1Hz to 100kHz while keeping PDA films at various dc potentials from -0.6V to 0.6V versus Ag/AgCl. PDA samples used for EIS went through a cyclic voltammetry treatment until the reversible redox peaks disappeared, prior to the EIS measurements. EIS fitting was done using Z_fit module in EC-Lab Software (Bio-Logic Science Instruments SAS, Claix, France). Cyclic Voltammetry was done with a Gamry Interface 1000 potentiostat from -1.0 to 1.0 V versus Ag/AgCl at the scan rate of 0.5 mV/s.

4.2.4 Morphological Characterization of PDA Films for Electrochemical Measurements

Atomic force microscopy (NTegra AFM, NT-MDT, Tempe, AZ USA) was performed in tapping mode. Scans were 10 μm × 10 μm at 0.8 Hz using tips with a reported radius of <10 nm (Budget Sensors, Sofia, Bulgaria; k = 40 N/m). Thicknesses were measured by scratching the films with a razor blade and measuring the height difference between scratched and unscratched regions. Data were analyzed via Gwyddion AFM software (http://gwyddion.net).

4.2.5 PDA Samples for Indentation Measurement Preparation

Silicon wafers with 1 μm thick thermal oxide were cleaned by sonication in acetone and isopropyl alcohol followed by rinsing in ddH2O. Substrates were further cleaned by UV-ozone treatment (5 min at 30 mW-cm^{-2}; Jelight, Irvine, CA USA). Substrates were then immersed in 60 ml of hexane mixed with 72 μl of APTES. Substrates were incubated for 16 h, then sonicated in

acetone, isopropyl alcohol, and then rinsed in ddH20 and methanol, and were dried under an N_2 stream. Substrates were incubated in 2 mg/ml dopamine hydrochloride in 10 mM Tris buffer solution in ambient air and under rotation (65 rpm) for 4 h, followed by sonication in 50 mM Tris HCl solution of pH = 8.5 for 2 h. PDA Samples were then rinsed in ddH_20 and stored in ddH_20.

4.2.6 Elastomeric Probes for Indentation Measurement Preparation

Hemispherical molds for elastomeric probes were created by using 6 mm diameter borosilicate glass hemispherical lenses and Norland Optical Adhesive 81 UV Glue. Polydimethylsiloxane (PDMS) blend was prepared by mixing 10 parts base to 1 part curing agent, went through degassing in mild vacuum for ~ 5 min three times. PDMS blend was poured in hemispherical molds (Diameter = 6 mm) and cured at 80 °C for 18 h. Silica-modified PDMS probes were prepared by exposing PDMS probes to UV-ozone treatment (10 min at 30 mW-cm^{-2}). Silica-modified PDMS probes were used immediately after the UV-ozone treatment.

4.2.7 Micro-indentation Measurements

The indentation probe was mounted on a 25g load cell (GSO-25, Transducer Techniques, Temecula, CA USA), attached to a stack of a vertical motorized stage (MFA-CC, Newport Corporation, Irving, CA USA) for vertical motion and a manual tilting stages (Newport GON40-L) for alignment, motion of which was controlled by Newport ESP 301 motion stage. Custom written LabView software was used for control. All measurements were performed at room temperature under aqueous condition. The acidic solution (pH = 4) was prepared by mixing 39 ml of 0.2 M Na_2HPO_4 with 61 ml of 0.1M Citric Acid. The basic solution (pH = 10.5) was prepared by mixing 100 ml 0.05M $NaHCO_3$, 36 ml of 0.1M NaOH, and 15 ml of 1M NaCl. The pH values of the solutions were measured using an Ag/AgCl electrode (Hach, model 5014T; Love-

land, CO USA). ddH2O (pH = 7) was used as a neutral solution. All measurements were done with the PDA sample and the probe fully submerged in one of the solutions (pH 4, 7, and 10.5). Prior to the measurements, probes were briefly dipped into the ethanol and air dried for ~ 5 min. The indentation probe was positioned over a PDA/PDMS substrates at arbitrary heights and approached at a vertical speed of 0.5 μm/s until reaching a preload of 1 mN, allowed to dwell for 120 s, and then retracted at 0.5 μm/s until the detachment occurred. Force-displacement curves were generated during the indentation. A single probe was used only for up to two measurements. For the cyclic experiment, a PDA sample went through the aqueous medium change after each measurement, and the wait-time of 3 min or >30 min was employed between the medium change and the measurement in that condition. A new probe was used for each measurement.

4.3 Results and Discussion

4.3.1 Electrochemical Assessment of Catechol Moieties Retaining Reversible Chemistry in PDA

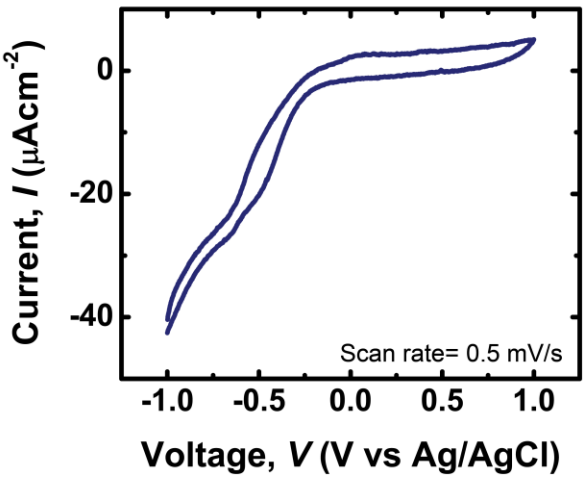

Figure 4.4: Cyclic Voltammogram of PDA on ITO in 0.01M PBS at the scan rate of 0.5 mV/s in the equilibrated state after several cycles.

PDA films (thickness = 40 nm; **see Appendix**) were deposited onto pre-cleaned Indium Tin Oxide (ITO) substrates. As reported in the literature, while the first few cycles of cyclic voltammetry (CV) showed considerable redox peaks, after several cycles, cyclic voltammetry profile of PDA on ITO did not show appreciable redox peaks (**Figure 4.4**).[30,31] As mentioned in the section 4.1.1, the origin of irreversibility is likely traced back to the fact that quinones undergo a nucleophilic attack by hydroxyl ions, losing their reversible oxidation state changeability, although several other mechanisms could come into play.[20-22] An intuitive conclusion to be drawn from the CV results would be that PDA has lost the reversible oxidation state controllability of the catechol groups in PDA; the conclusion would be true if PDA were a homogeneous material with its conductivity independent of the catechol redox state.

Studies show that a comproportionation equilibrium exists between catechols (H_2Q) and quinones (Q) in PDA producing semiquinone radicals (SQ):[32]

$$H_2Q + Q + 2H_2O \leftrightarrow 2H3O^+ + 2SQ^- \qquad \text{Eqn. 4.13}$$

Semiquinone radical population directly governs the electronic and ionic conductivity of PDA through complex mechanisms involving proton migration, comproportionation equilibrium, and redox processes.[21,32] In essence, semiquinones serve as a conduction pathway within PDA, and the percolation theory could be used to shed light on the currently observed phenomenon.

In percolation theory, a continuous conductive path is needed for electrical conduction across the material, which in the case of PDA is semiquinone molecules.[33] As the irreversible oxidation or any other insulating mechanism[21] occurs, the population of catechols that can participate in comproportionation equilibrium decreases, which in turn leads to decrease in the number of conduction pathway decrease and subsequent disappearance or attenuation of the redox peak in CV. However, given the heterogeneous nature of PDA, there is a possibility that the popula-

tion of catechols retaining reversible chemistry, severed from the conductive pathways thus doesn't manifest as a pronounced redox peak in CV, still remains within the PDA matrix (**Figure 4.5**).

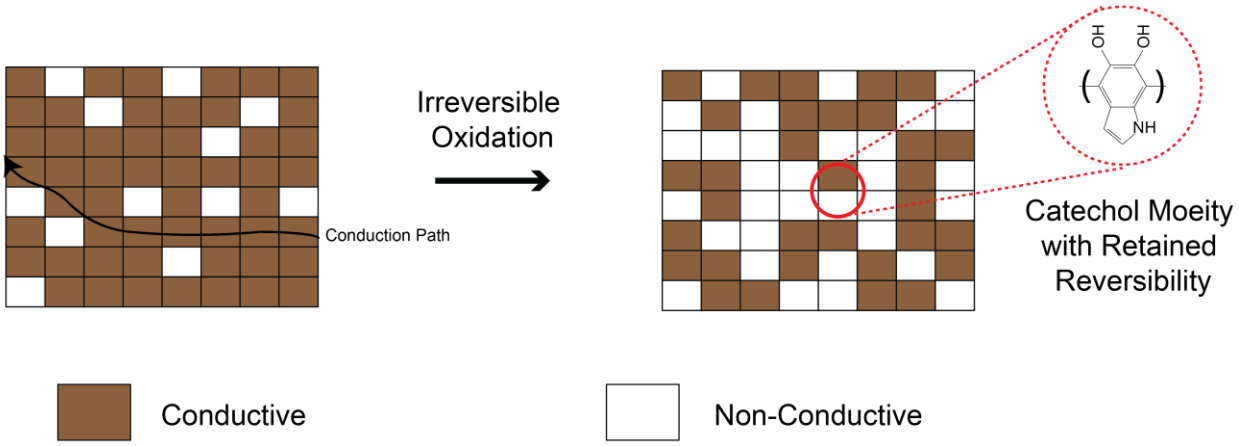

Figure 4.5: Schematic illustrating the proposed mechanism for the possible existence of catechol moieties with retained reversible chemistry within PDA after the irreversible oxidation or any other insulating mechanism. Even after the irreversible oxidation, a population of reversible chemistry catechols could exist severed from the conduction pathways.

To test the proposed assertion, EIS measurements were done on PDA samples after some cyclic voltages have been applied. EIS can provide additional insights as the EIS is a more sensitive technique that could capture the more nuanced-phenomena. Additionally, PDA could undergo a saturation like partly transient insulating behavior due to the depletion of the semiquinone population near the current injecting electrode (i.e. metal or presently ITO) through accumulation of fully oxidized or reduced population of catechols near the conducting electrode interface,[21] and use of small ac signal is likely to alleviate the saturation issue that can't be circumvented in CV measurements.

The EIS responses of a bare ITO and a 40 nm thick PDA on ITO at open circuit potential (no voltage applied) are shown in **Figure 4.6**. The Nyquist plot (**Figure 4.6c**) shows that the bare ITO shows typical almost 90-degree capacitive line, while the PDA film's response deviates

from the capacitive line. Impedance responses of both ITO and PDA interfaces are largely governed by frequency independent ohmic components such as external circuit and solution resistance in the system at the high frequency region ($f > 1$ kHz), evidenced by plateau region in the modulus plot and almost 0 degree region in the phase plot (**Figure 4.6a and b**).[34,35] However, for frequencies lower than 100 Hz, ohmic components that are insensitive to frequency are suppressed, and interfacial impedance dominates the response of the system (**Figure 4.6a**). Almost 90-degree phase at low frequencies ($f < 100$ Hz) for ITO indicates ion & electron blocking interface where no faradaic reaction takes place, and capacitive double layer charging is the dominant mechanism.[35] However, for the case of PDA, the constant rise in phase angle from 10 Hz hints at the presence of the redox reaction (**Figure 4.6b**).[34,35] The rise of the phase angle is not as evident as for the case of systems showing strong redox activity,[36,37] but is still present. The fact that PDA interface shows a lower interfacial impedance compared to ITO, even though the former has significantly lower conductivity hints that there still remain redox-active moieties, though not contributing directly for conduction, that decrease interfacial impedance by pseudocapacitive mechanism.[38]

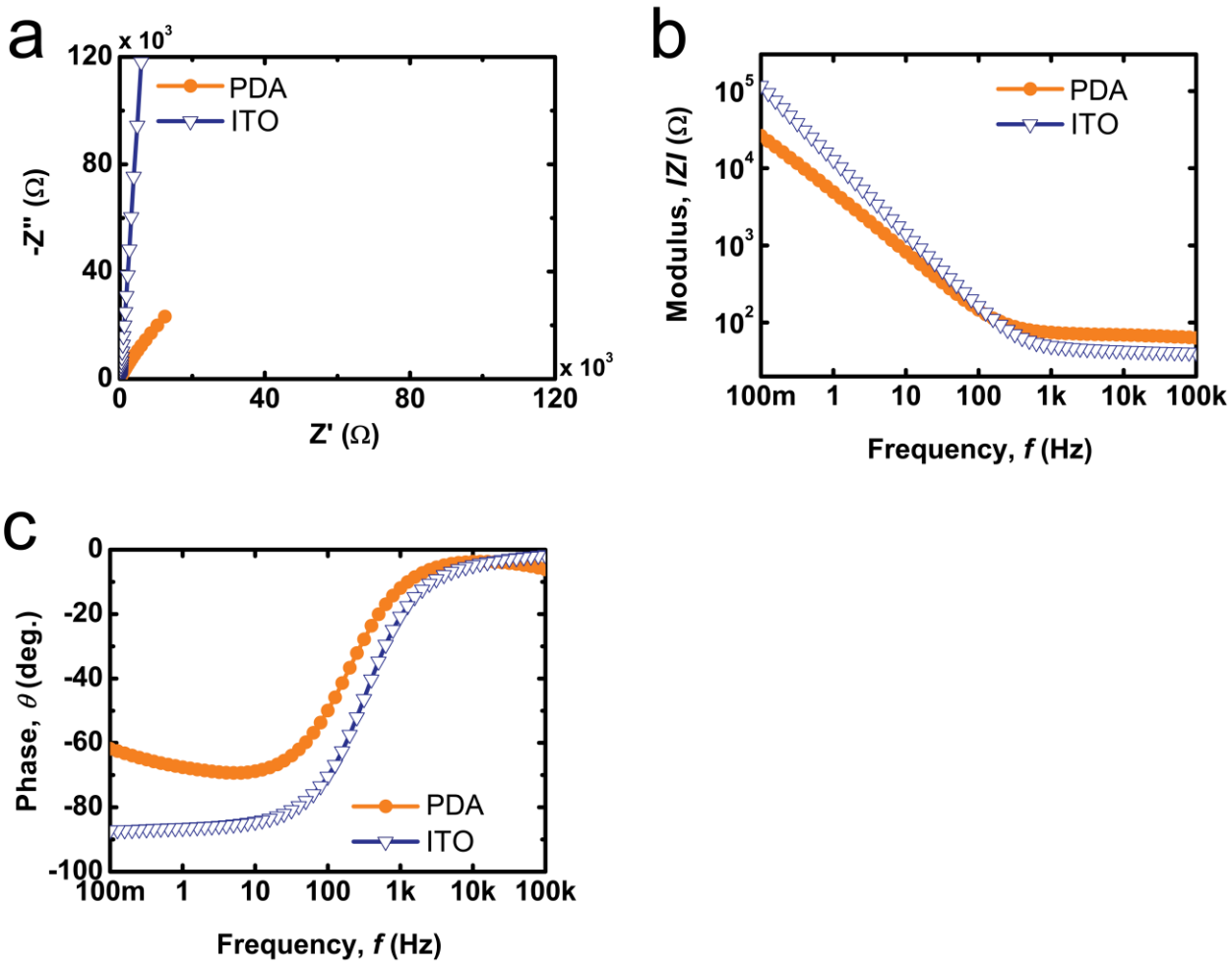

Figure 4.6: Bode plots and Nyquist plots from EIS measurements on a 40nm thick PDA film on ITO and bare ITO in the frequency range of $10^{-1} - 10^{5}$Hz (Sample area 1 cm^2) at open circuit potential. (a) Modulus plot (b) Phase plot (c) Nyquist Plot

For further investigation, EIS was performed while subjecting PDA and ITO Control samples to dc biases (E_{dc})varying from -0.6V to 0.6V versus Ag/AgCl. As expected, the response of bare ITO electrodes was insensitive to the applied bias and did not show sign of redox reaction except at highly negative biases where the response is likely to be attributed to H^+ reduction (**see Appendix**). For the case of the PDA interface, a strong voltage dependency is shown (**Figure 4.7**). At negative biases, as the dc potential became more negative, the onset of semicircle became clearer, signifying stronger redox activity, and thus smaller R_{ct} with increased bias as the radius of semicircle directly translates to R_{ct} (**Figure 4.7a**).[34] For the case of positive biases, at

0.4 V and 0.6 V biases, larger semi circles are observed with linear tails at the end, indicating a possible transition to the mass-transfer region. At 0.2 V, 45-degree straight line is shown, indicating the fastest charge transfer (lowest R_{ct}).[34] The following discussion could be an explanation for the observed phenomena.

For the case of mixed electronic ionic conductors, R_{ct} can be correlated with the mixed electronic and ionic conductivity of the system.[39] As the semiquinone population is directly linked to the conductivity of PDA, high mixed electronic and ionic conductivity means high concentration of semiquinones; the fact that a significant population of semiquinones is present right near the redox potential of catechol and that a PDA's impedance behavior is voltage sensitive, serve as evidence that a fairly significant portion of catechol moieties exist within PDA with reversible chemistry even after the irreversible oxidation. An additional explanation for the absence of redox peak in CV other than the irreversible oxidation could be provided by the transient high conductivity only shown at 0.2 V; despite the fairly significant portion of catechols retaining their reversibility, as the relatively high-conductance is only achieved at 0.2 V and rapidly decays as the applied voltage deviates from the redox potential of 0.2 V, a large portion of reversible catechols cannot go through oxidation state change due to the low-conductivity at potentials outside the narrow range near 0.2 V. The aforementioned saturation like build-up of insulation layer is likely to play a role as well.

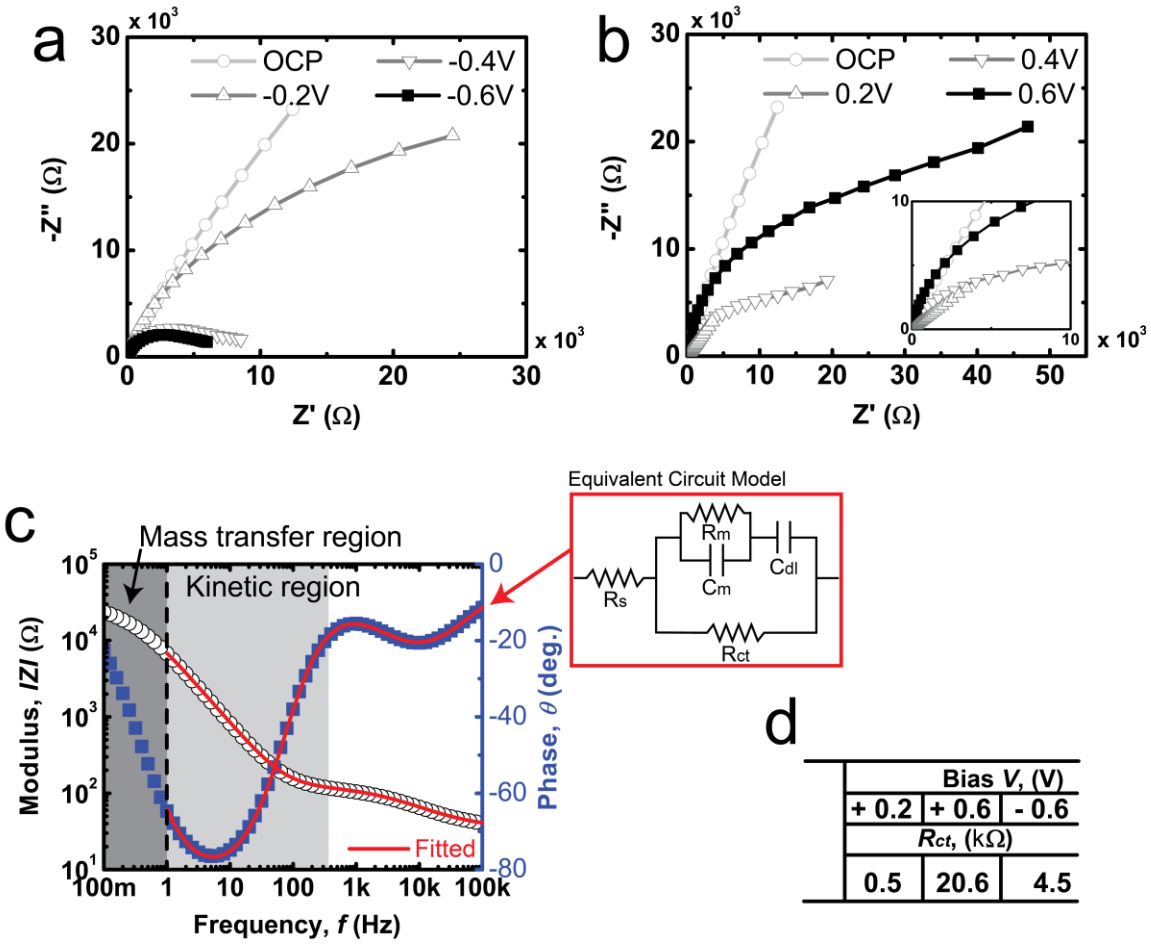

Figure 4.7: Evolution of impedance response of PDA in 0.01M PBS in the frequency range of $10^{-1} - 10^{5}$Hz, applying biases between -0.6 V to 0.6 V versus Ag/AgCl (Sample area $1cm^2$). a) Nyquist plots for negative biases. b) Nyquist plots for positive biases. c) A representative fit between experimental data and the modified Randles circuit model. Parameters are as follows: solution resistance (R_s); film capacitance contribution of the constant phase element (C_m, CPE); out of plane resistance of the film (R_m); double layer capacitance contribution of the constant phase element (C_{dl}, CPE); charge transfer resistance (R_{ct}). d) A tabulation of extracted values of R_{ct} using this model for 0.2 V, 0.6 V, and -0.6 V bias against Ag/AgCl.

To confirm the qualitative observation, EIS data for 0.2 V, 0.6 V and -0.6 V was fit to an equivalent circuit to extract the values of R_{ct} as a function of the applied voltage. Since the focus of fit is dedicated to understanding the evolution of R_{ct}, data were fit by focusing on the $f > 1$ Hz region (kinetic region) where the most data for R_{ct} is present. A parallel RC element was added in series with the double layer capacitance at the conventional Randles circuit to account for non-negligible film resistance and thickness-dependent capacitance at high frequencies.[40] The evolu-

tion of R_{ct} agrees with the qualitative observation such that 0.2 V shows the lowest R_{ct}. Through electrochemical measurements, two-points were confirmed: 1) PDA's electrochemical behavior remains to be voltage sensitive even after irreversible oxidation. 2) PDA's conductivity is transient exhibiting highest value at 0.2 V, near the catechol redox potential. Sensitive voltage dependency of PDA and high conductivity at 0.2 V, though not directly, confirms the presence of the significant number of catechols retaining reversible chemistry.

4.3.2 Reversible control of PDA Adhesion with Oxide Surface through Chemical Modulation

From the previous section, the presence of catechols with retained reversible chemistry was confirmed even after PDA went through irreversible oxidation; yet the transient conductivity, only near the narrow potential range within the redox potential of PDA, suggests that several complications could arise in a voltage-driven adhesion variance scheme. To test the reversibility of PDA's adhesion, a more facile pH control driven tests were carried out. To prevent the possible delamination of PDA under a strong alkaline condition, PDA films were covalently bound to the substrate using 3-aminopropyltriethoxysilane (APTES) layer.[19,41] Briefly, APTES layer was first deposited onto the pre-cleaned SiO_2 substrate through incubation in APTES hexane solution. Afterward, the substrate was immersed in dopamine hydrochloride solution for 4 h. Prepared PDA films were immersed in aqueous solutions of varying pH (pH = 4, 7, 10.5) made by mixing different combinations of solutes (**See Appendix**). The sodium concentration in acidic (pH 4) and basic (pH = 10.5) solution was roughly equal. Catechol molecules are known to oxidize to quinone as the pH approaches its first dissociation constant of the hydroxyl group (pKa = 9.3),[4,42,43] and the redox state equilibrium shows a variance over a broad range of pH values when the reactive oxygen molecule or other molecules are involved.[2,15,44] pH value of 4

where the high quinone reduction potential ($E^0 \sim 0.28\,V$)[45] is likely to assure catechol stability was chosen to bias motifs on PDA toward catechols, pH of 7 as an intermediate, and pH of 10.5 toward quinones. The adhesion of PDA films was measured through micro-indentation measurements in solutions of different pH levels. Poly(dimethylsiloxane) hemispherical probe that went through UV-ozone treatment (PDMS + SiO_2) were used. UV-ozone treatment is known to create a silica-like oxide layer on the PDMS surface.[46] As the catechol is known to interact with silica layer through H-bonding,[47] the adhesion strength between PDMS + SiO_2 probe and PDA will directly related to the number of reduced catechols participate in bonding with the probe. As-is poly(dimethylsiloxane) (PDMS) probe was used as a negative control. PDA is likely to interact with PDMS hydrophobically through the aromatic rings present in catechol moieties regardless of their oxidation states,[48] and relative insensitiveness to the pH level is expected for the PDMS probe.

Micro-indentation measurements generate force-displacement curves, and the maximum tensile force, i.e. pull-off force (F_{pull}) was used as a figure of merit to measure adhesion of PDA under different conditions (**Figure 4.8**). F_{pull} values for different experimental conditions were generated. At pH 4, F_{pull} value for measurements with PDMS + SiO_2 probe reach up to 1.93 mN, reaching an equivalent work of adhesion (W_{ad}) of 137 mN/m ($W_{ad} = F_{pull}/1.5\pi R$;[49] R = radius of the probe (3 mm)) (**See Appendix**). The measured F_{pull} value usually can't be directly compared to the thermodynamic interface energy calculation whenever the viscoelastic dissipative mechanism is present at the interface,[50] which is often true for the mechanically soft systems such as PDMS.[51,52] However, the silica layer created through UV-ozone treatment on PDMS has the modulus range in the Gpa range,[46,53] and the viscoelastic effect in water is minimal for PDMS.[54]

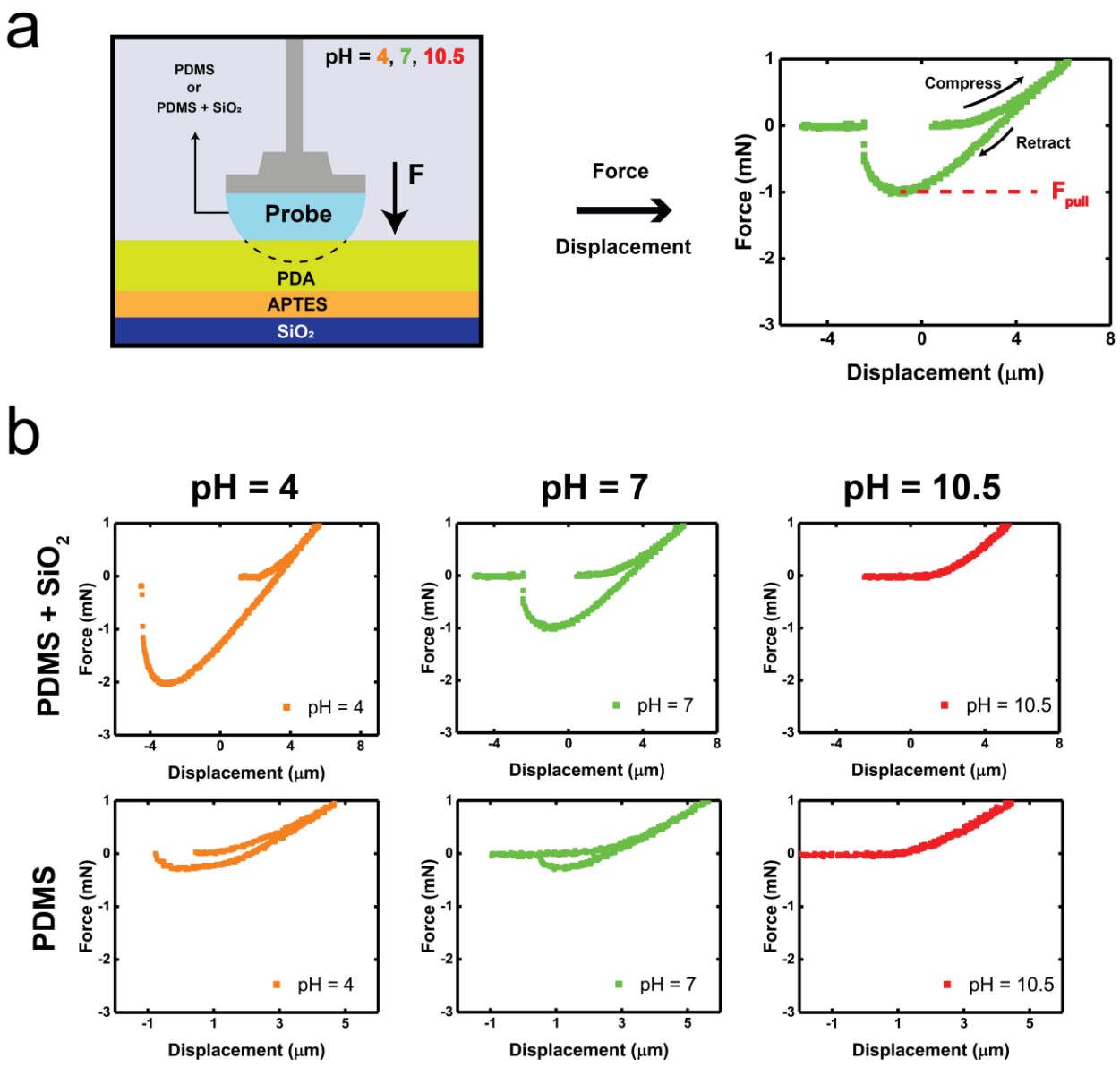

Figure 4.8: a) Schematic of the micro-indentation measurements. Either PDMS or PDMS + SiO2 probe was indented against PDA in solutions of varying pH, and the pull-off force was identified from the force-displacement curve. b) Representative force-displacement curves for different combinations of the probe material and pH levels.

Thus, it could be cautiously posited that the calculated W_{ad} value for PDMS + SiO_2 could be taken as a close approximation to the thermodynamic work of adhesion between PDA and PDMS + SiO_2 interface. The high W_{ad} value (~ 100 mN/m) between two PDMS + SiO_2 interfaces has been reported, the cause of which has been accounted to the high energy functional moieties (hydroxyl groups) and the possible molecular rotational freedom of those high-energy moie-

ties.[55] The measurement presented here is remarkable in that the PDA interaction with PDMS + SiO_2 interface shows high thermodynamically accountable W_{ad} value even in saline aqueous condition, attesting for the remarkable catechol-driven molecular adhesive capability of PDA. For the case of PDMS probe, W_{ad} ($F_{pull}/1.5\pi R$) value reaches up to 28 mN/m, which could have been affected by the effect of roughness (Chapter 2), but since the same is true for PDMS + SiO_2 probe, there is a possibility that W_{ad} is even higher.

Figure 4.9a shows the F_{pull} values at different pH level. For measurements at pH 4 and 7, F_{pull} values with PDMS+SiO_2 probes was consistently higher than those with PDMS probes in consistence with the proposed scheme that the energetically more favorable H-bonding is involved with PDA's interaction with PDMS + SiO_2 interface. F_{pull} measured with the PDMS probes didn't show much variance between pH 4 and pH 7 as expected, given the hydrophobic nature of the interaction. A variance in adhesion (F_{pull}) for PDMS + SiO_2 probe was observed such that F_{pull} at pH 4 is higher than that at pH 7. A higher population of reduced catechols could be responsible for the difference, as well as the change of interaction mechanism in the reduced state of catechols with a silica layer.[43] An interesting point to be noted is that the presence of salts, which is only present in the acidic solution, does not adversely impact the adhesion for PDA (**Figure 4.9b**). Silica and PDA has an isoelectronic point (IEP) of about 3 ~ 4,[56-58] and both could be regarded as effectively anionic surfaces in the acidic and neutral conditions in the study. Cation driven surface hydration layer is one of the main hindrances in underwater adhesion for polar surfaces, a situation often encountered in the nature as the natural surfaces underwater bear negative surface charge regardless of their original polarity due to sea organics.[25] Even though the interactive mode between PDMS and PDA is of hydrophobic nature,

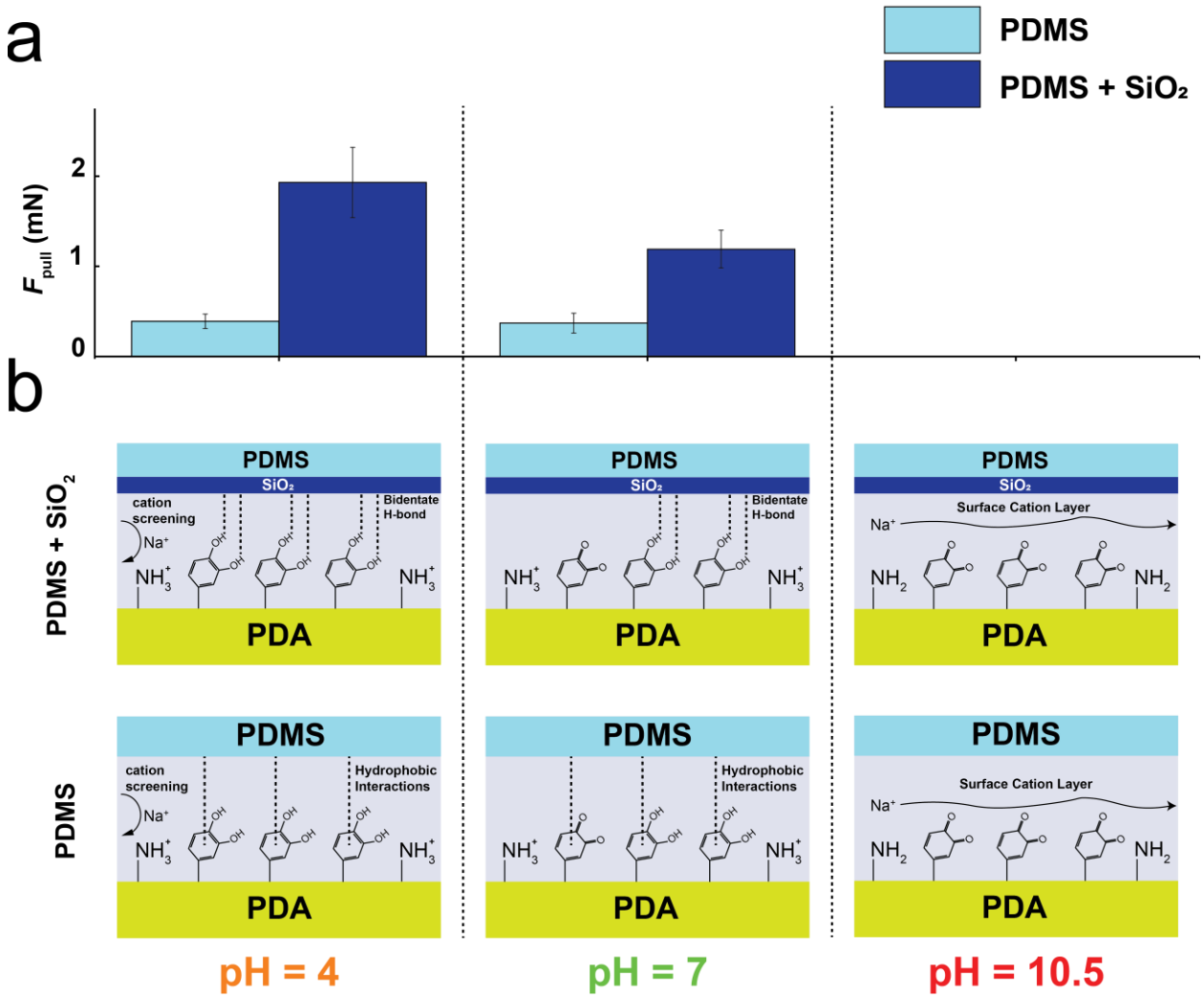

Figure 4.9: a) F_{pull} values for different experimental conditions. Left to right: pH = 4, 7, and 10.5. Data represented as mean ± s.d. for n = 10. b) Schematics illustrating the proposed adhesive mechanisms in each experimental condition. Top: PDA interaction with PDMS + SiO_2 probe. b-top-left) In acidic condition, amines prevent the cations from disrupting surface adhesion and the high population of reduced catechols adhere to silica through H-bonding. b-top-middle) In neutral condition, a lesser amount of reduced catechols participate in adhesion through H-bonding. b-top-right) In basic condition, surface cation hydration layer can't be disrupted due to the oxidation of amines and catechols. Bottom: PDA interaction with the PDMS probe. b-bottom-left) In acidic condition, amines prevent the cations from disrupting surface adhesion and reduced catechols interact with PDMS through hydrophobic interactions. b-bottom-middle) In neutral condition, catechols interact with PDMS through hydrophobic interaction, regardless of their oxidation states. b-top-right) In basic condition, despite the hydrophobic nature of the interaction between PDA and PDMS, as PDA is an anionic surface, disruptive surface cation hydration layers forms on the PDA side, preventing the adhesive interaction.

since PDA is anionic, if cations strongly bind to PDA surfaces, diminished adhesion must manifest. Yet, the invariance in adhesion shown between acidic saline solution and neutral salt-free solution for PDMS interaction demonstrates the effectiveness of PDA chemistry in preventing cations from influencing interfacial binding; higher adhesion at pH 4 compared to pH 7 for PDMS + SiO_2 interface also demonstrates PDA chemistry effectively screens the cation-driven effect to allow catechol chemistry to participate in interfacial binding. This effectiveness in screening cationic effect is likely due to the surface amine groups in PDA (**Figure 4.9b**).[59]

At pH 10.5, adhesion was abolished for both PDMS and PDMS + SiO_2 probe. For the case of PDMS + SiO_2 probe, the loss of H-bonding capability with oxidation of catechol and the loss of capability to displace surface cations with the oxidation of amines likely lead to the observed adhesion loss. For the case of PDMS, it is speculated that the similar mechanism is in play as described above; even though the hydrophobic interaction is the main mechanism with which PDA interacts with PDMS, PDA is close to being a hydrophilic (anionic) surface with hydrophobic interactivity. As the amines in PDA oxidizes at high pH, it could lead to an inability to displace surface salts at PDA, leading to failure to establish the connection with PDMS interface. Overall, the strong pH dependency of PDA with silica surface was observed, supporting the assertion that PDA interacts with silica oxide surface through catechol's H-bonding capability driven interaction.

Reversible control of PDA's adhesion with the PDMS+SiO_2 surface was tested in a cyclic experiment (**Figure 4.10**). F_{pull} between PDMS + SiO2 probe and PDA sample was measured by alternating between acidic (high-adhesion) and basic (low-adhesion) solutions. Wait-time of 3 min was employed between each measurement. While the switching behavior was

observed up to 10 cycles, hysteresis was observed, where the F_{pull} value in the acidic condition showed grad

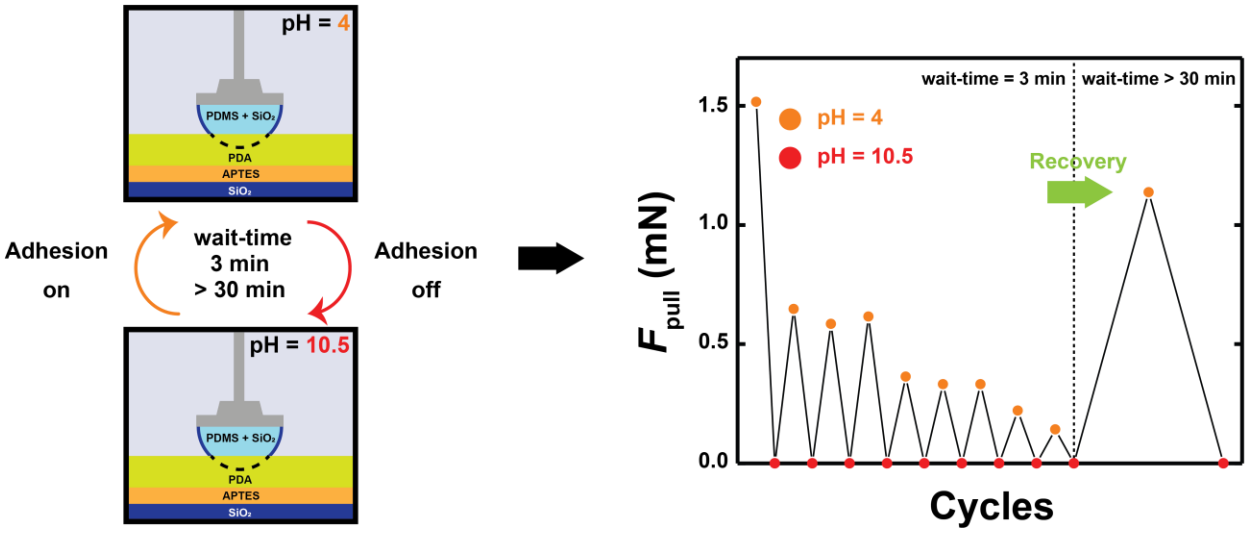

Figure 4.10: Demonstration of reversible modulation of PDA adhesion through pH control. Adhesion measurements were done using PDMS + SiO_2 probes onto a PDA sample by alternating between solutions of pH 4 and pH 10.5 while employing the wait-time of 3 min or > 30 min in-between. Plot of the pull-off forces vs. cycles. Decay in the adhesion (F_{pull}) was observed with successive cycles when the wait-time of 3 min was employed, but the adhesion was recovered after employing the longer-time, demonstrating the kinetic nature of the day.

ual decrease after each cycle. Hysteresis was reduced by a significant amount after the longer wait-time (30 min) was employed, hinting that the observed hysteresis is mostly from the slow kinetics of catechol to quinone transition rather than a permanent interfacial chemistry reconstruction. The observed behavior confirmed the reversible chemical controllability of PDA's adhesion in and serves as evidence that a significant portion of catechols retains reversible chemistry at least within the time-frame employed.

4.4 Conclusion

Chapter 4 has discussed the chemical modulation of PDA's adhesion. Contrary to the fully-reversible single molecule chemistry of catechol, a significant portion of catechols in PDA go

through irreversible oxidation. Yet, electrochemical measurements show that a significant population of catechols retain their reversibility, a fact further confirmed by the pH modulation of PDA's adhesion. At acidic and neutral pH, hydrophobic interaction driven adhesion scheme between PDMS and PDA did not show much fluctuation, yet adhesion between silica and PDA showed considerable variance. Adhesion was abolished for both silica (PDMS + SiO_2) and PDMS at the strong alkaline condition of pH 10.5, a phenomenon cautiously attributed to the failure of amines to dispel cations at PDA's interface at this pH level. PDA's adhesion showed reversible controllability through the cyclic application of different pH levels, but the kinetic-driven hysteresis was observed, which was mediated upon the use of longer wait-time. In conclusion, nuances in reversible chemical control of PDA's adhesion was investigated, which were able to observe through experimental study.

4.5 References

1 Lee, H., Scherer, N. F. & Messersmith, P. B. Single-molecule mechanics of mussel adhesion. *P Natl Acad Sci USA* **103**, 12999-13003, doi:10.1073/pnas.0605552103 (2006).

2 Ahn, B. K., Lee, D. W., Israelachvili, J. N. & Waite, J. H. Surface-initiated self-healing of polymers in aqueous media. *Nature Materials* **13**, 867, doi:10.1038/nmat4037

https://www.nature.com/articles/nmat4037#supplementary-information (2014).

3 Danner, E. W., Kan, Y., Hammer, M. U., Israelachvili, J. N. & Waite, J. H. Adhesion of Mussel Foot Protein Mefp-5 to Mica: An Underwater Superglue. *Biochemistry* **51**, 6511-6518, doi:10.1021/bi3002538 (2012).

4 Pegah, K. F. & P., L. B. Recent approaches in designing bioadhesive materials inspired by mussel adhesive protein. *Journal of Polymer Science Part A: Polymer Chemistry* **55**, 9-33, doi:doi:10.1002/pola.28368 (2017).

5 Soriaga, M. P. & Hubbard, A. T. Determination of the orientation of aromatic molecules adsorbed on platinum electrodes. The effect of solute concentration. *Journal of the American Chemical Society* **104**, 3937-3945, doi:10.1021/ja00378a026 (1982).

6 Lee, B. P. *et al.* Rapid Gel Formation and Adhesion in Photocurable and Biodegradable Block Copolymers with High DOPA Content. *Macromolecules* **39**, 1740-1748, doi:10.1021/ma0518959 (2006).

7 Yu, M., Hwang, J. & Deming, T. J. Role of l-3,4-Dihydroxyphenylalanine in Mussel Adhesive Proteins. *Journal of the American Chemical Society* **121**, 5825-5826, doi:10.1021/ja990469y (1999).

8 Liu, Y., Ai, K. & Lu, L. Polydopamine and Its Derivative Materials: Synthesis and Promising Applications in Energy, Environmental, and Biomedical Fields. *Chemical Reviews* **114**, 5057-5115, doi:10.1021/cr400407a (2014).

9 Maier, G. P., Bernt, C. M. & Butler, A. Catechol oxidation: considerations in the design of wet adhesive materials. *Biomaterials Science* **6**, 332-339, doi:10.1039/C7BM00884H (2018).

10 Josep, S., Javier, S. P., Felix, B. & Daniel, R. M. Catechol-Based Biomimetic Functional Materials. *Advanced Materials* **25**, 653-701, doi:doi:10.1002/adma.201202343 (2013).

11 Koob, T. Effects of oxidation and reduction on the spectral properties of the egg capsules of Raja erinacea Mitchill. *Journal of experimental marine biology and ecology* **113**, 155-166 (1987).

12 Kim, E. *et al.* Context-Dependent Redox Properties of Natural Phenolic Materials. *Biomacromolecules* **15**, 1653-1662, doi:10.1021/bm500026x (2014).

13 Dai, O., Masato, K., Ryosuke, A. & Tsugiko, T. Stability Dependence on Redox–active Site Structure in Free Catechol- or Hydroquinone–substituted Polypyridylruthenium(II) Complexes. *ChemistrySelect* **2**, 2583-2587, doi:doi:10.1002/slct.201700153 (2017).

14 DuVall, S. H. & McCreery, R. L. Control of catechol and hydroquinone electron-transfer kinetics on native and modified glassy carbon electrodes. *Analytical Chemistry* **71**, 4594-4602 (1999).

15 Narkar, A. R., Barker, B., Clisch, M., Jiang, J. & Lee, B. P. pH Responsive and Oxidation Resistant Wet Adhesive based on Reversible Catechol–Boronate Complexation. *Chem Mater* **28**, 5432-5439, doi:10.1021/acs.chemmater.6b01851 (2016).

16 Ryu, J. H., Messersmith, P. B. & Lee, H. Polydopamine Surface Chemistry: A Decade of Discovery. *ACS Applied Materials & Interfaces* **10**, 7523-7540, doi:10.1021/acsami.7b19865 (2018).

17 Liebscher, J. *et al.* Structure of Polydopamine: A Never-Ending Story? *Langmuir* **29**, 10539-10548, doi:10.1021/la4020288 (2013).

18 Lee, H., Dellatore, S. M., Miller, W. M. & Messersmith, P. B. Mussel-Inspired Surface Chemistry for Multifunctional Coatings. *Science* **318**, 426 (2007).

19 Luke, K., Zeeshan, A., Venkatasubramanian, V. & J., B. C. Synthesis and Measurement of Cohesive Mechanics in Polydopamine Nanomembranes. *Adv Mater Interfaces* **4**, 1700041, doi:doi:10.1002/admi.201700041 (2017).

20 Lin, Q., Li, Q., Batchelor-McAuley, C. & Compton, R. G. Two-Electron, Two-Proton Oxidation of Catechol: Kinetics and Apparent Catalysis. *The Journal of Physical Chemistry C* **119**, 1489-1495, doi:10.1021/jp511414b (2015).

21 Wünsche, J. *et al.* Protonic and Electronic Transport in Hydrated Thin Films of the Pigment Eumelanin. *Chem Mater* **27**, 436-442, doi:10.1021/cm502939r (2015).

22 Electrochemical Study of Catechol in the Presence of Dibuthylamine and Diethylamine in Aqueous Media: Part 1. Electrochemical Investigation. *Electroanalysis* **17**, 1755-1760, doi:doi:10.1002/elan.200503279 (2005).

23 Yang, J., Cohen Stuart, M. A. & Kamperman, M. Jack of all trades: versatile catechol crosslinking mechanisms. *Chemical Society Reviews* **43**, 8271-8298, doi:10.1039/C4CS00185K (2014).

24 Arzillo, M. *et al.* Eumelanin Buildup on the Nanoscale: Aggregate Growth/Assembly and Visible Absorption Development in Biomimetic 5,6-Dihydroxyindole Polymerization. *Biomacromolecules* **13**, 2379-2390, doi:10.1021/bm3006159 (2012).

25 Waite, J. H. Nature's underwater adhesive specialist. *International Journal of Adhesion and Adhesives* **7**, 9-14, doi:https://doi.org/10.1016/0143-7496(87)90048-0 (1987).

26 G., B. T., M., H. H., R., C. S. & Milena, G. M. Versatile Surface Modification Using Polydopamine and Related Polycatecholamines: Chemistry, Structure, and Applications. *Adv Mater Interfaces* **4**, 1601192, doi:doi:10.1002/admi.201601192 (2017).

27 Lasia, A. in *Modern aspects of electrochemistry* 143-248 (Springer, 2002).

28 Lasia, A. *Electrochemical impedance spectroscopy and its applications*. (Springer, 2014).

29 Lee, H., Dellatore, S. M., Miller, W. M. & Messersmith, P. B. Mussel-inspired surface chemistry for multifunctional coatings. *Science* **318**, 426-430, doi:10.1126/science.1147241 (2007).

30 Yang, J., Niu, L. H., Zhang, Z. J., Zhao, J. & Chou, L. J. Electrochemical Behavior of a Polydopamine Nanofilm. *Anal Lett* **48**, 2031-2039, doi:10.1080/00032719.2015.1010120 (2015).

31 Zangmeister, R. A., Morris, T. A. & Tarlov, M. J. Characterization of Polydopamine Thin Films Deposited at Short Times by Autoxidation of Dopamine. *Langmuir* **29**, 8619-8628, doi:10.1021/la400587j (2013).

32 Mostert, A. B. *et al.* Role of semiconductivity and ion transport in the electrical conduction of melanin. *Proceedings of the National Academy of Sciences* **109**, 8943 (2012).

33 Clingerman, M. L. *Development and modelling of electrically conductive composite materials*, Michigan Technological University Houghton, (2001).

34 Macdonald, J. R. & Barsoukov, E. Impedance spectroscopy: theory, experiment, and applications. *History* **1**, 8 (2005).

35 Orazem, M. E. & Tribollet, B. *Electrochemical impedance spectroscopy*. Vol. 48 (John Wiley & Sons, 2011).

36 Franceschetti, D. R. & Macdonald, J. R. *Small-signal AC response theory for electrochromic thin films*. (Defense Technical Information Center, 1981).

37 Ho, C., Raistrick, I. D. & Huggins, R. A. Application of Ac Techniques to the Study of Lithium Diffusion in Tungsten Trioxide Thin-Films. *J Electrochem Soc* **127**, 343-350, doi:Doi 10.1149/1.2129668 (1980).

38 Lee, Y. A. *et al.* Mussel-inspired surface functionalization of porous carbon nanosheets using polydopamine and Fe3+/tannic acid layers for high-performance electrochemical capacitors. *Journal of Materials Chemistry A* **5**, 25368-25377, doi:10.1039/C7TA08010G (2017).

39 Bobacka, J., Lewenstam, A. & Ivaska, A. Electrochemical impedance spectroscopy of oxidized poly(3,4-ethylenedioxythiophene) film electrodes in aqueous solutions. *J Electroanal Chem* **489**, 17-27, doi:Doi 10.1016/S0022-0728(00)00206-0 (2000).

40 Freger, V. & Bason, S. Characterization of ion transport in thin films using electrochemical impedance spectroscopy. I. Principles and theory. *J Membrane Sci* **302**, 1-9, doi:10.1016/j.memsci.2007.06.046 (2007).

41 Mi, Y. *et al.* A simple and feasible in-situ reduction route for preparation of graphene lubricant films applied to a variety of substrates. *Journal of Materials Chemistry* **22**, 8036-8042, doi:10.1039/C2JM16656A (2012).

42 Springsteen, G. & Wang, B. A detailed examination of boronic acid–diol complexation. *Tetrahedron* **58**, 5291-5300, doi:https://doi.org/10.1016/S0040-4020(02)00489-1 (2002).

43 Yu, J. *et al.* Adhesion of Mussel Foot Protein-3 to TiO2 Surfaces: the Effect of pH. *Biomacromolecules* **14**, 1072-1077, doi:10.1021/bm301908y (2013).

44 Klegeris, A., Korkina, L. G. & Greenfield, S. A. Autoxidation of dopamine: A comparison of luminescent and spectrophotometric detection in basic solutions. *Free Radical Biology and Medicine* **18**, 215-222, doi:https://doi.org/10.1016/0891-5849(94)00141-6 (1995).

45 Eslami, M., Zare, H. R. & Namazian, M. Thermodynamic Parameters of Electrochemical Oxidation of l-DOPA: Experimental and Theoretical Studies. *The Journal of Physical Chemistry B* **116**, 12552-12557, doi:10.1021/jp3054229 (2012).

46 Béfahy, S. *et al.* Thickness and Elastic Modulus of Plasma Treated PDMS Silica-like Surface Layer. *Langmuir* **26**, 3372-3375, doi:10.1021/la903154y (2010).

47 Mian, S. A. *et al.* Density Functional Theory Study of Catechol Adhesion on Silica Surfaces. *The Journal of Physical Chemistry C* **114**, 20793-20800, doi:10.1021/jp1070538 (2010).

48 Yu, J. *et al.* Adaptive hydrophobic and hydrophilic interactions of mussel foot proteins with organic thin films. *Proceedings of the National Academy of Sciences* **110**, 15680 (2013).

49 Johnson, K. L., Kendall, K. & Roberts, A. Surface energy and the contact of elastic solids. *Proc. R. Soc. Lond. A* **324**, 301-313 (1971).

50 Song, J., Tranchida, D. & Vancso, G. J. Contact Mechanics of UV/Ozone-Treated PDMS by AFM and JKR Testing: Mechanical Performance from Nano- to Micrometer Length Scales. *Macromolecules* **41**, 6757-6762, doi:10.1021/ma800536y (2008).

51 Chen, Y. L., Helm, C. A. & Israelachvili, J. N. Molecular mechanisms associated with adhesion and contact angle hysteresis of monolayer surfaces. *The Journal of Physical Chemistry* **95**, 10736-10747, doi:10.1021/j100179a041 (1991).

52 Zhang, W. *et al.* Surface and Tribological Behaviors of the Bioinspired Polydopamine Thin Films under Dry and Wet Conditions. *Biomacromolecules* **14**, 394-405, doi:10.1021/bm3015768 (2013).

53 Mangipudi Venkata, S., Huang, E., Tirrell, M. & Pocius Alphonsus, V. Measurement of interfacial adhesion between glassy polymers using the JKR method. *Macromolecular Symposia* **102**, 131-143, doi:10.1002/masy.19961020118 (1996).

54 Tiwari, A. *et al.* The effect of surface roughness and viscoelasticity on rubber adhesion. *Soft matter* **13**, 3602-3621 (2017).

55 Rundlöf, M. *et al.* Application of the JKR Method to the Measurement of Adhesion to Langmuir–Blodgett Cellulose Surfaces. *Journal of Colloid and Interface Science* **230**, 441-447, doi:https://doi.org/10.1006/jcis.2000.7108 (2000).

56 Barclay Thomas, G., Hegab Hanaa, M., Clarke Stephen, R. & Ginic-Markovic, M. Versatile Surface Modification Using Polydopamine and Related Polycatecholamines: Chemistry, Structure, and Applications. *Adv Mater Interfaces* **4**, 1601192, doi:10.1002/admi.201601192 (2017).

57 Cuddy, M. F., Poda, A. R. & Brantley, L. N. Determination of Isoelectric Points and the Role of pH for Common Quartz Crystal Microbalance Sensors. *ACS Applied Materials & Interfaces* **5**, 3514-3518, doi:10.1021/am400909g (2013).

58 Kosmulski, M. *Chemical Properties of Material Surfaces*. (CRC Press, 2001).

59 Maier, G. P., Rapp, M. V., Waite, J. H., Israelachvili, J. N. & Butler, A. Adaptive synergy between catechol and lysine promotes wet adhesion by surface salt displacement. *Science* **349**, 628 (2015).

Chapter 5
Conclusions and Perspectives

5.1 Summary of Work

This work explores the fundamentals of macroscopic adhesion in polydopamine (PDA) interfaces and various modulation mechanisms through which the polydopamine interfaces' macro-adhesive behavior changes. Chapter 2 discusses the texture-dependent adhesion in PDA. A common misconception in the literature regarding PDA adhesion is that PDA nanomembranes should exhibit strong adhesive capability as PDA conformally coats various surfaces underwater during *in-situ* polymerization. However, PDA is a rigid material with heterogeneous morphology inevitably caused by its heterogeneous synthesis process. A framework considering both its mechanical behavior and morphology needs to be used to understand PDA's adhesive behavior correctly. Studies presented in Chapter 2 confirms the presence of nanoscale texture-dependent adhesion in PDA and validates that PDA's adhesion is a strong function of its morphology. Additionally, an effect of water in adhesion in relation to texture was analyzed, an often very ill-defined problem.

Chapter 3 discusses the dynamic control of PDA interface adhesion through the application of mechanical strains. Thin-film buckling is a common phenomenon that occurs in a two-material sandwich structure when there is a big modulus mismatch between two layers with one layer having a significantly lower thickness than the back layer. Thin-film buckling phenomenon induces surface wrinkles on the substrates, the geometry of which can be controlled by varying the mechanical strain and other form factors. PDA nanomembranes were incorporated in PDA/PDMS substrates, and PDA/PDMS substrates with varying wrinkle geometries were

fabricated. PDA interface adhesion showed a strong dependency to the wrinkle geometries. Additionally, flattening and wrinkling of the wrinkled PDA/PDMS substrates with the cyclic application of mechanical strain was used to reversibly control PDA adhesion, demonstrating the proposed scheme's effectiveness in fast actuation of reversible control of PDA adhesion, confirming PDA's potential as a component in the micro-structured adhesive structures. A novel theoretical framework based on the elliptical JKR model was presented that could be used to analyze the adhesive interaction between the spherical probe and the planar-wrinkle arrays, which showed a good agreement with the experimental results.

Chapter 4 explores the efficacy of chemical modulation of PDA adhesion. Catechol molecule's adhesion strength is its redox state-dependent, and its single molecule chemistry is reversible; however, within the PDA matrix, it is known to go through irreversible oxidation through covalent cross-linking with adjacent molecules. Cyclic voltammetry study confirmed the assertion and hinted that the practically idealistic approach of modulating PDA adhesion through voltage wouldn't be plausible at the present stage. However, the lack of redox peak doesn't necessarily mean the depletion of catechol groups that exhibit reversible chemistry; as the comproportionation mechanism is a likely conduction mechanism within PDA, some catechol species could remain electrically isolated from the metallic interface, but still, preserve their reversible chemistry. Additional electrochemical measurements with electrochemical impedance spectroscopy revealed that even after going through the irreversible oxidation, a certain amount of catechol groups with reversible chemistry remains intact. Spinning off from the electrochemical control of PDA adhesion, chemical control of PDA adhesion was explored. Series of indentation measurements under various pH levels revealed that PDA adhesion shows strong reversible pH

dependency against oxide surfaces where the redox-state dependent bidentate hydrogen bonding is the likely main adhesive mechanism.

5.2 Future Perspectives

While this work uncovered some fundamentals of PDA adhesion and explored the possibility of PDA incorporation into micro-structured adhesives, there remain a significant amount of both fundamental and practical questions that need to be addressed.

The most imperative would be a fundamental study of the synthesis route and structure of PDA, which still is an active area of investigation. Investigation of PDA using conventional spectroscopic techniques have proven to be challenging; a novel experimental design would be needed to uncover some previously inaccessible correlations. A better understanding of the molecular structure of PDA is likely to lead to solutions or alternatives to the following more practical questions.

More homogeneous film quality will significantly accelerate PDA adaptation on a commercial scale. Even though some indirect routes exist for PDA film quality improvement, currently, it is not possible to achieve the level of topological homogeneity required for the practical adaptation of PDA in many fields. Additionally, indirect evidence in the literature point that the same reason causing the heterogeneity in topography (adsorption of aggregates grown from the solution) could lead to mechanical failures of PDA. Also the film growth limit in a single synthesis step, which currently is at around ~ 50 nm, needs to be addressed as well, along with the PDA's slow growth kinetics.

Resolving the irreversible oxidation of catechol groups in PDA will also be very important. This issue is something that all the catechol chemistry driven materials suffer from.

While this very mechanism is responsible for the cohesive strength of PDA, a strategy to stop the unwanted irreversible oxidation after the synthesis will significantly improve the commercial lifespan of PDA or other catecholic systems, if realized. Also, the conductivity improvement would need to occur.

Another important area to check would be the use of PDA for geometries that permit high adhesion. Surface wrinkle approach presented in the study showed high controllability of adhesion, but the adhesion increment was not big due to the low degree of contact splitting. Translation into fibrillar structures or possibly isotropic wrinkles with much smaller features warrant a further study; incorporation of PDA specific characteristics for tunability of adhesion would be an interesting topic of the subject as well. After the successful demonstration of the concept under dry condition, the realistic high wet-adhesion concept needs to be explored; even though some principles were uncovered in the study, a more complete picture of the interfacial phenomena in water could lead to some novel design principles for underwater adhesion.

Even though PDA in a native form suffers from high modulus, it might function well as a film on soft biological tissues, as tissues will provide the needed tackiness, while PDA provides advantageous interfacial chemistry. Thus, the use of PDA as a medical film that delivers therapeutic agents is worth pursuing.

It now has been a decade since the first introduction of polydopamine in 2007. Many have been uncovered since then, but many still remain elusive. There is no doubt that polydopamine will continue to serve as a source of entertainment for researchers across many fields in the coming years, as it has been.

Appendix

Chapter 2 Supporting Figures

Polydopamine surface tension and the thermodynamic work of adhesion between polydopamine and PDMS determination procedure:

	γ_L (mN/m)	γ^d_L (mN/m)	γ^p_L (mN/m)
Water[1]	72.8	22.6	50.2
Glycerol[2]	63.4	37	26.4
Ethylene Glycol[2]	48.8	32.8	16

Table A1: Total surface tension values, and dispersive and polar components of surface tension values for liquid probes used in the study.

Contact angle data was analyzed in light of Owens-Wendt theory to recover the dispersive and polar components of the surface tension of polydopamine (PDA) nanomembranes. According to Owens-Wendt, the dispersive component of the surface tension of the solid (γ_S^d), the polar component of the surface tension of the solid (γ_S^p), the dispersive component of the surface tension of the liquid (γ_L^d), the polar component of the surface tension of the liquid (γ_L^p), the overall surface tension of the liquid ($\gamma_L = \gamma_L^d + \gamma_L^p$), and the contact angle (CA) between the liquid and the solid (θ) in air follows the following relation:[3]

$$\frac{\gamma_L(\cos\theta+1)}{2(\gamma_L^d)^{\frac{1}{2}}} = (\gamma_S^p)^{\frac{1}{2}}\frac{(\gamma_L^p)^{\frac{1}{2}}}{(\gamma_L^d)^{\frac{1}{2}}} + (\gamma_S^d)^{\frac{1}{2}} \qquad \text{Eqn. A1}$$

This equation is a linear equation ($y = mx + b$), wherein:

$$y = \frac{\gamma_L(\cos\theta+1)}{2(\gamma_L^d)^{\frac{1}{2}}} \qquad \text{Eqn. A2}$$

$$m = (\gamma_S^p)^{\frac{1}{2}} \qquad \text{Eqn. A3}$$

$$x = \frac{(\gamma_L^p)^{\frac{1}{2}}}{(\gamma_L^d)^{\frac{1}{2}}} \quad \text{Eqn. A4}$$

$$b = \left(\gamma_S^d\right)^{\frac{1}{2}} \quad \text{Eqn. A5}$$

With known surface tension values of liquids and the contact angle data for three liquid probes on PDA, an Owens-Wendt plot of $\frac{\gamma_L(\cos\theta+1)}{2(\gamma_L^d)^{\frac{1}{2}}}$ vs. $\frac{(\gamma_L^p)^{\frac{1}{2}}}{(\gamma_L^d)^{\frac{1}{2}}}$ was constructed, and from the slope and intercept of the linear fit, each component of the surface tension of PDA was constructed.

	CA_{Water} (deg)	$CA_{Glycerol}$ (deg)	$CA_{EthylGlycol}$ (deg)	γ^d_{PDA} (mN/m)	γ^p_{PDA} (mN/m)	γ_{PDA} (mN/m)
Apical Side	56.3 ± 1.1	35.0 ± 5.6	15.3 ± 4.9	28.3 ± 3.5	19.6 ± 2.7	47.9 ± 4.4
Basal Side	57.9 ± 0.5	40.5 ± 0.9	18.8 ± 2.0	29.7 ± 3.7	17.9 ± 2.8	47.6 ± 4.6

Table A2: Contact angle (CA) data for three liquid probes on PDA nanomembranes in air. The resulting total surface tension values, and dispersive and polar components of surface tension values for PDA nanomembranes are extracted from the Owens-Wendt Plot (n = 3).

The thermodynamic work of adhesion between PDA and PDMS in air was calculated as:[4]

$$W_{ad} = 2\left(\sqrt{\gamma^d_{PDMS}\gamma^d_{PDA}} + \sqrt{\gamma^p_{PDMS}\gamma^p_{PDA}}\right) \quad \text{Eqn. A6}$$

Given the surface tension values of $\gamma^d_{PDMS} = 18\ mN/m$ and $\gamma^p_{PDMS} = 0\ mN/m$ for PDMS,[5] the thermodynamic work of adhesion between PDA and PDMS in air was ~ 40 mN/m. The thermodynamic work of adhesion between PDA and PDMS in water was calculated as:[4]

$$W_{ad} = 2\left(\gamma^d_{Water} + \gamma^p_{Water} + \sqrt{\gamma^d_{PDMS}\gamma^d_{PDA}} + \sqrt{\gamma^p_{PDMS}\gamma^p_{PDA}} - \sqrt{\gamma^d_{PDMS}\gamma^d_{Water}} - \sqrt{\gamma^p_{PDMS}\gamma^p_{Water}} - \sqrt{\gamma^d_{PDA}\gamma^d_{Water}} - \sqrt{\gamma^p_{PDA}\gamma^p_{Water}}\right) \quad \text{Eqn. A7}$$

The thermodynamic work of adhesion between PDA and PDMS in water was estimated to be ~ 50 mN/m.

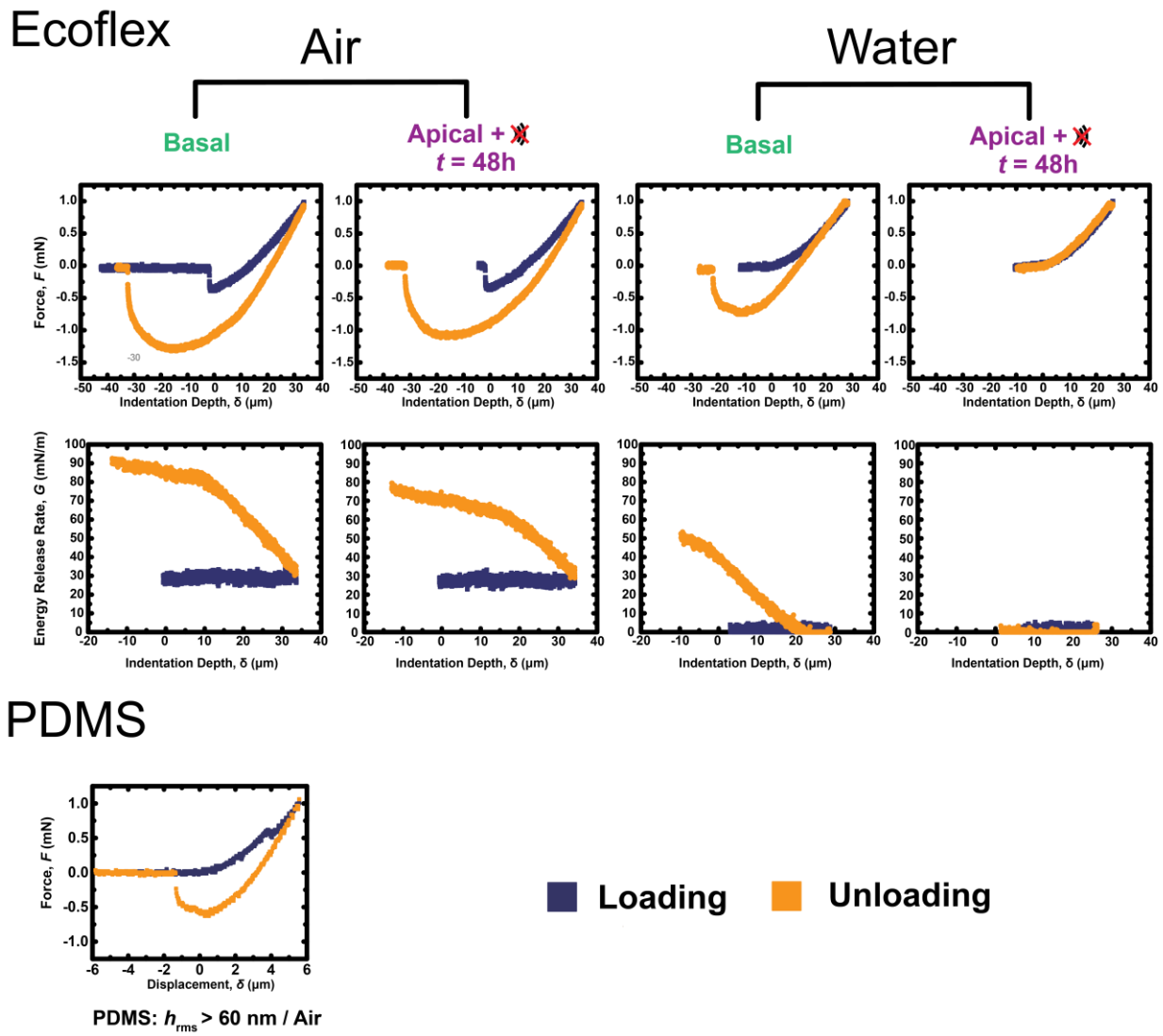

Figure A1: Ecoflex) Representative force-(indentation depth) curves (top) and energy release rate versus indentation depth plots (bottom) for measurements with Ecoflex lenses against basal side samples ($h_{rms,PDA}$ = 18.1 nm & $h'_{rms,PDA}$ = 0.047) and 48h PDA samples ($h_{rms,PDA}$ = 192.6 nm & $h'_{rms,PDA}$ = 1.03) in air and water. For Ecoflex lenses, across all the roughness ranges of PDA nanomembranes studied ($h_{rms,PDA}$ < 200 nm), data from the loading phase of force-displacement measurements in air could be fit to the JKR equation (R2 > 0.995). The average value of the energy release rates was found to be G = 31 ± 4 mN/m (n = 14). For Ecoflex lenses, in water, the non-zero tensile force was shown only against PDA samples with $h_{rms,PDA}$ < 20 nm. PDMS) A representative force-displacement curve for measurements between PDMS lenses and PDA nanomembranes with $h_{rms,PDA}$ > 60 nm in air. In this roughness range, JKR fit to the force-displacement data during the loading phase was not possible.

Computation of the theory curve in the effective work of adhesion versus RMS roughness plot for in air measurements:

To evaluate the effect of surface roughness on the work of adhesion, the model developed by You et al. was implemented.[6] While the model is similar to the multi-asperity model developed by Greenwood and Williamson,[7] it simplifies the load dependence and treats different tension – compression state that each asperity experiences in a lump-sum manner. However, this model permits an intuitive tractable parametric closed form solution and showed good agreements with pull-off forces with other experiments and for the present condition. Given any randomly rough surface, surface roughness features can be estimated by Gaussian distribution;[8-10] then the height distribution of the surface can be estimated as:

$$P_{\mathrm{h}}(h) = \frac{1}{\sqrt{2\pi}\sigma} e^{-\frac{h^2}{2\sigma^2}} \qquad \text{Eqn. A8}$$

where σ is the RMS roughness of the surface.

When a hemispherical lens with Young's modulus of E_1 is brought into contact with the rough surface with Young's modulus of E_2 and the RMS roughness of σ, the ratio of the actual area in contact given the nominal contact area can be estimated as:

$$C = \frac{1}{2}\left[\mathrm{erf}\left(\frac{\overline{\delta_1}+\overline{\delta_2}-h_{\min}}{\sqrt{2}\sigma}\right)+1\right] \qquad \text{Eqn. A9}$$

Where

$$\overline{\delta_1} = 3.530\left(\frac{\sigma^{\frac{1}{2}}\Delta\gamma}{E^*}\right) \qquad \text{Eqn. A10}$$

$$\overline{\delta_2} = 3.207\left(\frac{\sigma^{\frac{1}{2}}\Delta\gamma}{E^*}\right) \qquad \text{Eqn. A11}$$

$$h_{\min} = 2.7\sigma \qquad \text{Eqn. A12}$$

$$E^* = \left[\frac{1-\nu_1^2}{E_1} + \frac{1-\nu_2^2}{E_2}\right]^{-1} \left(E_2 \gg E_1, E^* \approx \frac{E_1}{1-\nu_1^2}\right) \quad \text{Eqn. A13}$$

Then the ratio between the roughness affected pull-off force and pull-off force assuming surfaces are smooth is $C^{\frac{3}{2}}$.

For the computation of the curve, E_1 = 1.2 MPa and E_1 = 60 kPa was used for PDMS and Ecoflex lenses respectively, and $\Delta\gamma = 35$ mN/m was used. $C^{\frac{3}{2}}$ vs. σ was computed, and $C^{\frac{3}{2}}$ was multiplied by 80 mN/m (the average value of the interfacial dissipation effected work of adhesion during pull off for measurements against smooth PDA nanomembranes ($h_{\text{rms,PDA}}$ < 60 nm)) to get W_{UL} vs. σ curve for the theoretical fit.

Chapter 3 Supporting Figures

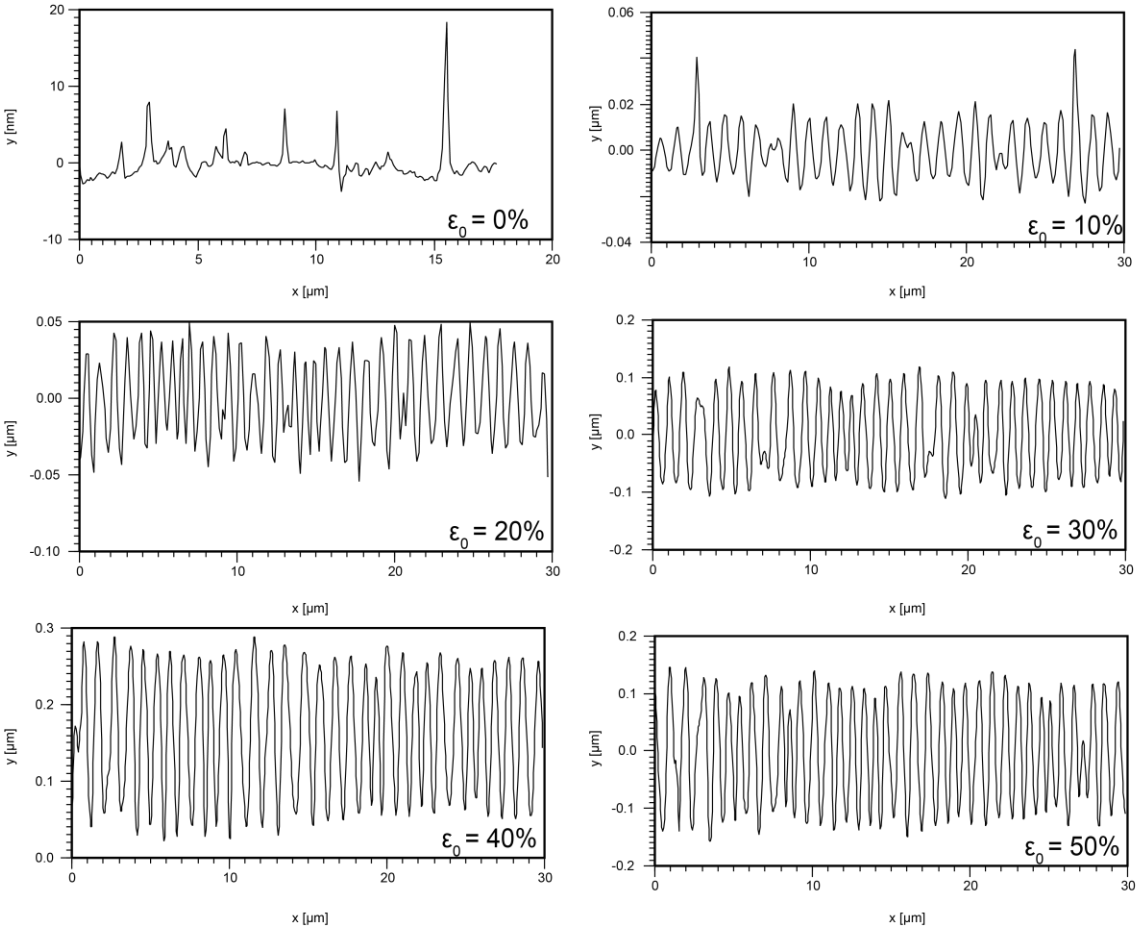

Figure A2: Representative 2D height profiles of the PDA/PDMS substrates created with different pre-strain conditions. Sections of the samples with a minimal amount of adsorbed spherical particles, cracks, or ridges were chosen.

ε_0 (%)	10	20	30	40	50
λ (µm)	1.13 ± 0.33	0.89 ± 0.13	0.88 ± 0.07	0.84 ± 0.13	0.82 ± 0.1
A (nm)	19.6 ± 5.9	32.1 ± 4	95.6 ± 8.5	100.9 ± 13.3	116.1 ± 11.9

Table A3: Wavelength and amplitude of the PDA/PDMS substrates created with different pre-strain conditions. Data presented as mean ± s.d. for n = 10.

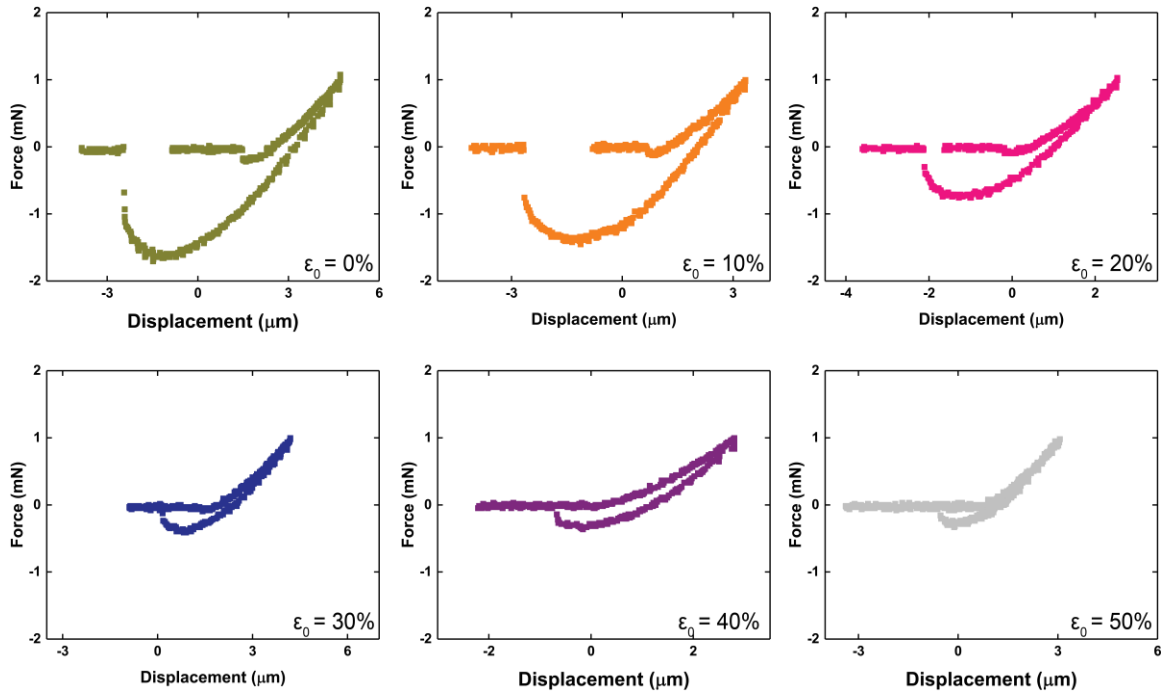

Figure A3: Exemplary Force-displacement curves for the PDA/PDMS substrates created with different pre-strains.

ε_0 (%)	0	10	20	30	40	50
F_{pull} (mN)	1.48 ± 0.14	1.66 ± 0.25	0.78 ± 0.28	0.32 ± 0.06	0.32 ± 0.09	0.26 ± 0.04

Table A4: F_{pull} values for measurements with the PDA/PDMS substrates created with different prestrains. Data presented as mean ± s.d. for $n \geq 4$.

Construction of the non-dimensional spherical JKR curve:

Given the normalized contact radius $\bar{a}$, the normalized load $\bar{f}$ and the normal approach $\bar{\delta}$ of the spherical JKR theory for a circular contact are given in the following expressions:[11]

$$\bar{f} = \bar{a}^3 - \sqrt{2\bar{a}^3} \qquad \text{Eqn. A14}$$

$$\bar{\delta} = \bar{a}^2 - \frac{2}{3}\sqrt{2\bar{a}} \qquad \text{Eqn. A15}$$

Plot of $\bar{f}$ vs $\bar{\delta}$ can be constructed by establishing relationships using the same values for $\bar{a}$. $\bar{f}$ and $\bar{\delta}$ are linked to unionized counter parts with the following expressions:

$$\bar{f} = \frac{f}{3\pi R_e \mathrm{G_c}} \qquad \text{Eqn. A16}$$

$$\bar{\delta} = \delta R_e \left[\frac{9\pi R_e^2 G_c}{4E^*}\right]^{-\frac{2}{3}} \qquad \text{Eqn. A17}$$

where E^* is the equivalent elastic modulus between interacting bodies, G_c is the work of adhesion between two surfaces, and R_e is the radii of interacting bodies. Essentially, the spherical JKR model equivalent to the elliptical JKR model interaction between cylinders with radius r and R_i would be the interaction of the cylinders with the same radii, R_e given as the geometric mean between the elliptical model cylinders ($R_e = \sqrt{rR_i}$).

Construction of the force versus normal approach between the hemispherical probe and the wrinkled surface using the spherical JKR model:

For the JKR model with the spherical contact area, f_i vs δ_i curves can be constructed by employing the following relationships:[12]

$$\delta_i = \frac{a_i^2}{R_{i,e}} - \sqrt{\frac{2\pi a_i G_c}{E^*}} \qquad \text{Eqn. A18}$$

$$f_i = \frac{4E^* a_i^3}{3R_{i,e}} - \sqrt{8\pi E^* G_c a_i^3} \qquad \text{Eqn. A19}$$

where a_i is the contact radius, G_c is the work of adhesion between two surfaces, and $R_{i,e}$ is the geometric mean of the radius between two bodies given by $R_{i,e} = \sqrt{rR_i}$. Essentially the same procedure was repeated as detailed in the flow diagram (**Figure 3.11**) to construct the F vs δ curve for the spherical JKR model.

ε_0 (%)	0	10	20	30	40	50
Elliptical Model F_{pull} (mN)	0.36[a]	0.42	0.23	0.083	0.078	0.065
Spherical Model F_{pull} (mN)	0.36[a]	1.3	0.91	0.48	0.46	0.42

a = $1.5\pi G_c$; G_c = 25.5 mN and R = 3 mm

Table A5: Calculated F_{pull} values at each pre-strain for the elliptical JKR model and the spherical JKR model. For the case of zero pre-strain, the value was calculated using the characteristic JKR relation.[13]

Chapter 4 Supporting Figures

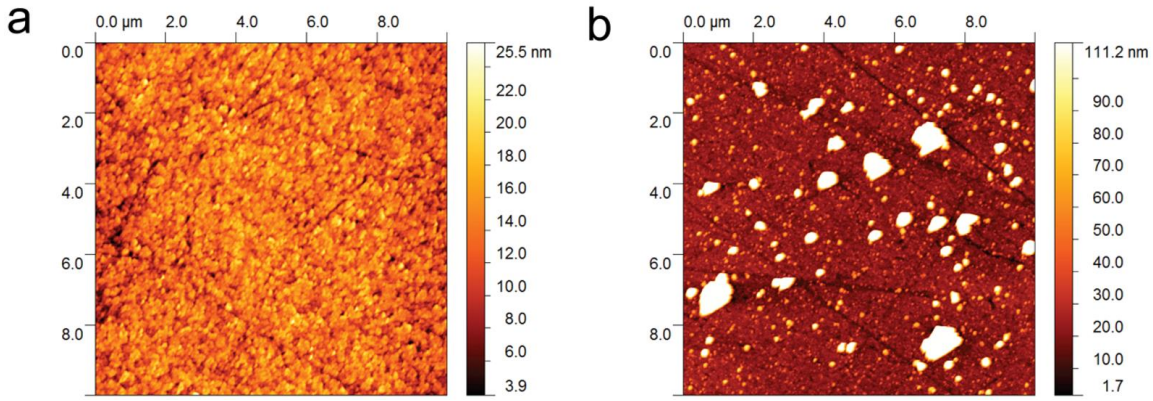

Figure A4: AFM scans of an ITO substrate and PDA film on ITO substrate. AFM scans were taken with 512 x 512 pixels. a) 10 µm x 10 µm scan of an ITO substrate. b) 10 µm x 10 µm scan of PDA film on ITO substrate. Thickness of the PDA sample was 40.5 ± 4.8 nm (mean ± s.d. for n = 3).

Sample	Ra (nm)	RMS(nm)
Bare ITO	1.94 ± 0.11	2.42 ± 0.13
40 nm thick PDA	41.9 ± 6.5	79.9 ± 8.7

Table A6: Roughness Statistics for ITO substrates and PDA films. Data presented as mean ± s.d. for n = 3.

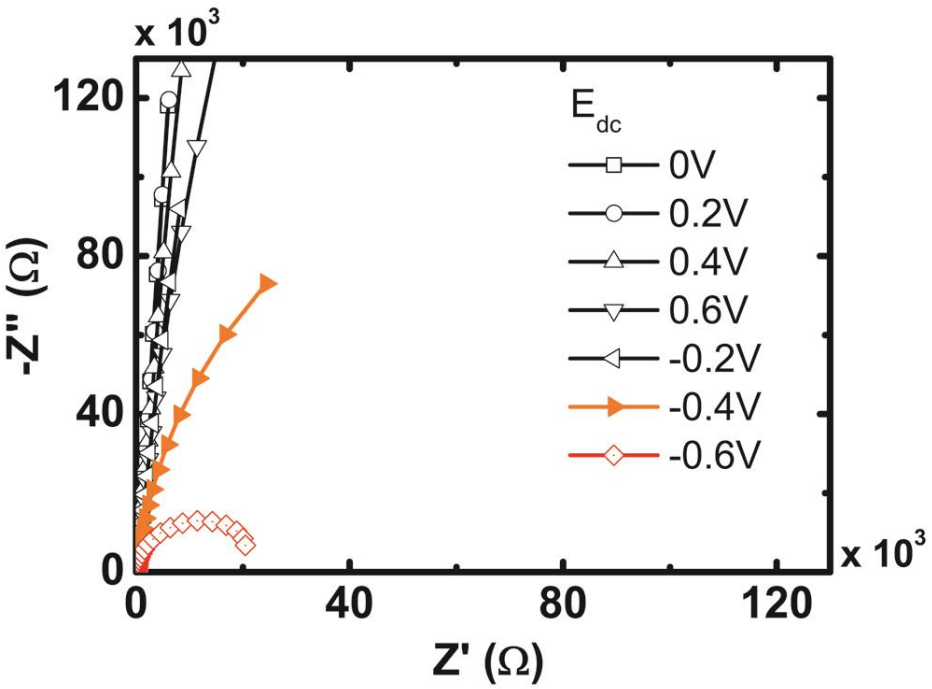

Figure A5: Nyquist plots from EIS measurements on bare ITO at various dc biases from -0.6V to 0.6V versus Ag/AgCl. The onset of the semicircle is clear at -0.4V and -0.6V versus Ag/AgCl thus indicating active H^+ reduction.

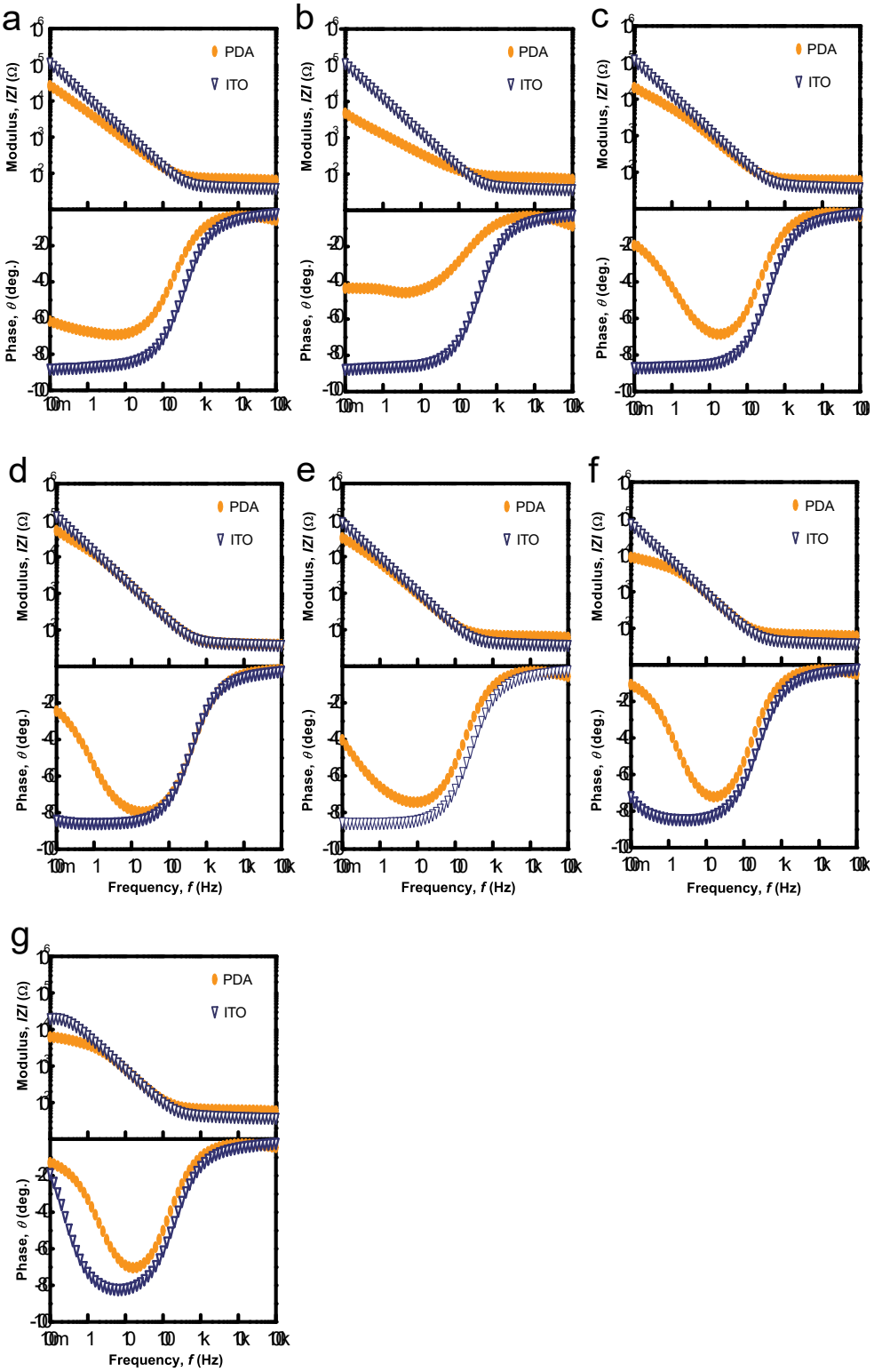

Figure A6: Representative Bode plots extracted from EIS measurements on PDA films and a bare ITO at the following biases versus Ag/AgCl: (a) Open Circuit Potential; (b) E_{dc} = 0.2 V; (c) E_{dc} = 0.4 V; (d) E_{dc} = 0.6 V; (e) E_{dc} = -0.2 V; (f) E_{dc} = -0.4 V; (g) E_{dc} = -0.6 V. PDA films showed comparable or lower interfacial impedance throughout the bias range studied.

Sample	pH[a]	pH[b]	Composition	$[Na^+]$ (M)
Acidic Solution	4	4.5	38.55ml 0.2M Na_2HPO_4 + 61.45ml 0.1M Citric Acid	≈ 0.15
Neutral Solution	7	7	N/A (ddH_2O)	0
Basic Solution	10.5	10.16	100ml 0.05M $NaHCO_3$ + 35.6ml 0.1M NaOH + 14.6ml 1M NaCl	≈ 0.15

a: measured using Ag/AgCl

b: theoretical

Table A7: Composition of the solutions used in the study.

pH Probe	pH = 4 PDMS	pH = 4 PDMS+SiO_2	pH = 7 PDMS	pH = 7 PDMS+SiO_2	pH = PDMS	pH = 10.5 PDMS+SiO_2
F_{pull} (mN)	0.39±0.08	1.93±0.39	0.37±0.11	1.19±0.21	~0.0	~0.0

Table A8: Measured pull-off forces F_{pull} for different experimental conditions. Data presented as mean ± s.d. for n = 10.

References

1 Dalal, E. N. Calculation of Solid-Surface Tensions. *Langmuir* **3**, 1009-1015, doi:DOI 10.1021/la00078a023 (1987).

2 Mittal, K. L. *Contact angle, wettability and adhesion*. Vol. 4 (CRC Press, 2006).

3 Owens, D. K. & Wendt, R. C. Estimation of the surface free energy of polymers. *Journal of Applied Polymer Science* **13**, 1741-1747, doi:10.1002/app.1969.070130815 (1969).

4 Clint, J. H. & Wicks, A. C. Adhesion under water: surface energy considerations. *Int J Adhes Adhes* **21**, 267-273, doi:Doi 10.1016/S0143-7496(00)00029-4 (2001).

5 Yang, F. K. *et al.* "Contact" of Nanoscale Stiff Films. *Langmuir* **28**, 9562-9572, doi:10.1021/la301388e (2012).

6 You, S. M. & Wan, M. P. Mathematical Models for the van der Waals Force and Capillary Force between a Rough Particle and Surface. *Langmuir* **29**, 9104-9117, doi:10.1021/la401516m (2013).

7 Greenwood, J. A. & Williamson, J. B. Contact of Nominally Flat Surfaces. *Proc R Soc Lon Ser-A* **295**, 300-319, doi:DOI 10.1098/rspa.1966.0242 (1966).

8 Greenwood, J. A. & Wu, J. J. Surface roughness and contact: An apology. *Meccanica* **36**, 617-630, doi:Doi 10.1023/A:1016340601964 (2001).

9 Persson, B. N. J., Albohr, O., Tartaglino, U., Volokitin, A. I. & Tosatti, E. On the nature of surface roughness with application to contact mechanics, sealing, rubber friction and adhesion. *J Phys-Condens Mat* **17**, R1-R62, doi:10.1088/0953-8984/17/1/R01 (2005).

10 Robbe-Valloire, F. Statistical analysis of asperities on a rough surface. *Wear* **249**, 401-408, doi:Doi 10.1016/S0043-1648(01)00548-8 (2001).

11 Johnson, K. L. & Greenwood, J. A. An approximate JKR theory for elliptical contacts. *Journal of Physics D: Applied Physics* **38**, 1042 (2005).

12 Hui, C. Y., Lin, Y. Y., Baney, J. M. & Jagota, A. The accuracy of the geometric assumptions in the JKR (Johnson–Kendall–Roberts) theory of adhesion. *Journal of Adhesion Science and Technology* **14**, 1297-1319, doi:10.1163/156856100742203 (2000).

13 Johnson, K. L., Kendall, K. & Roberts, A. Surface energy and the contact of elastic solids. *Proc. R. Soc. Lond. A* **324**, 301-313 (1971).